

UC Santa Cruz

UC Santa Cruz Electronic Theses and Dissertations

Title

Investigations into the mechanisms that regulate C. elegans developmental timekeeping

Permalink

<https://escholarship.org/uc/item/86j914hd>

Author

Ashley, Guinevere

Publication Date

2022

Copyright Information

This work is made available under the terms of a Creative Commons Attribution License, available at <https://creativecommons.org/licenses/by/4.0/>

Peer reviewed|Thesis/dissertation

UNIVERSITY OF CALIFORNIA

SANTA CRUZ

Investigations into the mechanisms that regulate *C. elegans* developmental timekeeping

A dissertation submitted in partial satisfaction

of the requirements for the degree of

DOCTOR OF PHILOSOPHY

In

MOLECULAR, CELLULAR, DEVELOPMENTAL BIOLOGY

by

Guinevere E Ashley

September 2022

The Dissertation of Guinevere E Ashley is approved:

Professor Jordan Ward, Chair

Professor Needhi Bhalla

Professor Carrie Partch

Professor Joshua Arribere

Peter Biehl, Provost and Dean of Graduate Studies

Table of Contents

List of Figures	iv
Abstract	vi
Acknowledgments	viii
Chapter 1 Investigating the links between biological timing mechanisms in nematodes and mammals	1
Chapter 1 Bibliography	39
Chapter 2 An expanded auxin-inducible degron toolkit for targeted protein degradation in <i>Caenorhabditis elegans</i>	47
Chapter 2 Bibliography	100

List of Figures and tables

Figure 1.1 Generic negative transcriptional feedback loop with delay.	3
Figure 1.2 Core Mammalian Circadian clock and Auxiliary loop.	5
Figure 1.3 <i>C. elegans</i> life cycle.	6
Figure 1.4 Conservation of key domains between LIN-42 and PER and high sequence similarity between KIN-20 and human CK1.	10
Figure 1.5 <i>lin-42</i> genomic locus and described mutant alleles.	11
Figure 1.6 CK1 δ /PER2 phospho-switch mechanism regulates 24-hour circadian periodicity.	13
Fig. 1.7 CK1 δ binds and phosphorylates LIN-42 C-terminal constructs.	17
Figure 1.8 Deletions of the conserved CKBD region results in developmental abnormalities.	22
Fig. 1.9 Deletions of the conserved <i>lin-42</i> CKBD region results asynchronous molts and developmental delay.	23
Figure 1.S.1 Protein sequence of LIN-42B used to make constructs and mutants strains	30
Figure 1.S.2 Sequence alignment of <i>C. elegans</i> LIN-42, mouse PER2 and human PER2	32
Table 1.1 List of strains used in chapter 1	37
Figure 2.1. Schematic of the auxin-inducible degron (AID) system.	50
Figure 2.2 A new TIR1 expression system allows assessment of TIR1 expression and activity.	54
Table 2.1 Plasmids to support generation of new TIR1 alleles and other transgenes at standardized genetic loci through CRISPR/Cas-based genome editing.	55
Figure 2.3 The F2A ribosome skip sequence functions efficiently in an <i>eft-3p::TIR1::F2A::BFP::AID*::NLS</i> transgene.	57
Figure 2.4 <i>eft-3p::TIR1::F2A::BFP::AID*::NLS</i> depletes <i>AID*::GFP</i> to the same extent as <i>eft-3p::TIR1::mRuby2</i> but exhibits a slower rate of degradation.	59

Figure 2.5 <i>eft-3p::TIR1::F2A::BFP::AID*::NLS</i> depletes NHR-25::GFP::AID* to the same extent as <i>eft-3p::TIR1::mRuby2</i> but also exhibits a slower degradation rate.	62
Table 2.2 <i>eft-3p::TIR1::F2A::BFP::AID*::NLS</i> produces comparable depletion phenotypes to <i>eft-3p::TIR1::mRuby2</i> for depleting nuclear proteins.	65
Table 2.3 <i>eft-3p::TIR1::F2A::BFP::AID*::NLS</i> produces comparable depletion phenotypes to <i>eft-3p::TIR1::mRuby2</i> for depleting cytoplasmic proteins.	66
Figure 2.6 A new suite of TIR1 expression strains for tissue-specific depletion of AID-tagged proteins in <i>C. elegans</i> .	68
Figure 2.7 NHR-25::GFP::AID*::3xFLAG can be depleted in a cell-specific manner in a strain with undetectable TIR1 expression via a BFP reporter.	71
Figure 2.8. A collection of vectors to generate FP::AID* knock-ins through Gibson cloning and a suite of new vectors for the SapTrap cloning system.	74
Figure 2.9. A collection of vectors to generate FP::AID* knock-ins using linear repair templates.	76
Figure 2.S1 Anti-GFP western blot with wild type (N2) control.	93
Figure 2.S2 Representative images of AID*::GFP and NHR-25::GFP::AID* depletion in animals expressing either <i>eft-3p::TIR1::mRuby2</i> or <i>eft-3p::TIR1::F2A::BFP::AID*::NLS</i> .	94
Figure 2.S3 Nuclear/cytoplasmic ratios of AID*::GFP in VPCs with activated TIR1.	96
Figure 2.S4 Functional test of new TIR1-expressing strains.	97

Abstract

Investigations into the mechanisms that regulate *C. elegans* developmental timekeeping

By Guinevere Ashley

All living organisms have biological clocks that drive and coordinate repetitive developmental processes. These intrinsic timing devices are essential for animal development and survival but, in many cases, the underlying mechanisms are poorly understood. *C. elegans* larval development is an ideal system in which to study this problem. *C. elegans* employ two distinct but interrelated biological timing mechanisms to regulate progression through larval development. The heterochronic pathway ensures that stage-specific cellular events happen at the correct time and in the correct order, while a molt timer ensures the proper timing of each molt in relation to developmental progression. Chapter one of this work describes our investigations into the mechanisms employed by *C. elegans* to regulate and coordinate developmental progression and molting. *lin-42*, the *C. elegans* homolog to the circadian clock protein PERIOD2 (PER2), is unique among heterochronic genes for its dual role in regulating both stage-specific cellular events, and the precise timing and execution of molting, and is thought to coordinate molt cycles with developmental progression. To investigate the mechanisms through which LIN-42 regulates and coordinates developmental timing in *C. elegans*, we looked to the well-characterized mechanisms employed by its mammalian homolog PER2. The circadian period in mammals is determined by the stability of PER2 and the stability is largely determined through its interaction with Casein Kinase I δ (CK1 δ). Our work shows that CK1 δ can bind and phosphorylate a LIN-42 substrate *in vitro* with similar

kinetics compared to a PER2 substrate and that these interactions depend on conserved kinase binding domains. Further, we show that deletion of the SYQ and LT domains, two highly conserved alpha helices within the conserved kinase binding domain, results in dysregulation of LIN-42::GFP expression in vivo. However, severe developmental abnormalities and molting defects are only observed once those deletions are extended to encompass the whole kinase binding domain. Together, these data suggest that PER2/LIN-42 phosphorylation by CK1 δ kinases is evolutionarily conserved and that this mechanism may be employed to coordinate developmental timing in *C. elegans*.

When investigating essential systems and critical gene products, we often cannot employ classical genetic approaches to study gene function. Critical regulators of developmental progression and timing often function with distinct co-regulators in various developmental contexts and may have reiterative functions throughout development. In knockout or null mutants, if disruption of the first developmental event results in embryonic or larval lethality, later functions will be missed. Chapter 2 of this work describes a set of genetic tools that we produced to complement existing reagent and augment the use of the auxin inducible degron (AID) system in *C. elegans*. The AID system is a powerful tool to conditionally deplete proteins. We generated a set of single-copy, tissue-specific and pan-somatic TIR1-expressing *C. elegans* strains carrying a co-expressed blue fluorescent reporter to enable use of both red and green channels in experiments. We also generated a set of plasmids for constructing repair templates to generate fluorescent protein::AID fusions through CRISPR/Cas9-mediated genome editing. Together, these reagents will complement existing TIR1 strains and facilitate rapid and high-throughput fluorescent protein::AID tagging of genes.

Acknowledgments

There are more people than I can name on this page whose influence, mentorship, encouragement, and/or companionship have been invaluable to my success and well-being. I am forever thankful for every single one of you. No one can do this life thing alone.

Jordan, thank you for your patience and guidance. I'm glad I picked you as my PI. Matticus, thank you for patiently answering my twenty million questions over the years, helping me grow as a scientist, and for bringing chocolate into my life when I most need it. Becca, how sad I would be without your cheerful, candy-filled visits. Thank you Londen for being my company for so many years. I want to acknowledge every one of our lab members, past and present for the role you played in contributing to my success, whether that be a helping hand with an experiment, a helpful conversation, or just pleasant company. It's been grand.

I also want to thank my thesis advisory committee for your helpful contributions and discussions and encouragement. I think it's also important to acknowledge the people who kept me alive, sane, and happy while I did this work. Apple and Chris, thank you for hosting our family dinners, for being awesome, and for welcoming my tendency to show up unannounced and bury my face in your sofa. I can't express how much I appreciate you two and how much I love that you like to feed me. Miss Jessie, same. It is so important to have people in my life who remind me that it's okay to be exactly who and what I am in all situations. Thank you for accepting me and reminding me to accept myself. A big giant shoutout to all the folks I've adventured and traveled and played with in these last few years, your presence made it a joy and I hope I see more of you. I especially want to thank my partner Richard who has supported me in nearly every way for over a decade. He won't

talk science with me, but life would be a lot more stressful and a heck of a lot lonelier without him. Finally, I must acknowledge all the pups (Spotty, Berserker, Katelyn, Nordy, and Kona) who provided me endless supplies of cuddles and joy. What a sad life this would be without you.

Chapter 1:

Investigating the links between biological timing mechanisms in nematodes and mammals

Guinevere Ashley¹, Becca Spangler², Kathrin Braun³, Carrie Partch², Jordan Ward¹

¹Dept. of Molecular, Cell, and Developmental Biology, UC Santa Cruz

²Dept. of Chemistry and Biochemistry, UC Santa Cruz

³Friedrich Miescher Institute for Biomedical Research (FMI)

Author contributions: G.A, B.S, C.P, J.W contributed intellectually to this work; conceived and designed the experiments and collaborated to interpret results, analyzed and quantified data, and planned project direction. B.S constructed necessary reagents and performed *in vitro* biochemical assays. G.A constructed necessary reagents/*C. elegans* mutant strains and performed *in vivo* assays and phenotypic analysis, except for the luciferase assays, which were performed and analyzed by Kathrin Braun.

Abstract:

All living organisms have biological clocks that drive and coordinate repetitive developmental processes. These intrinsic timing devices are essential for animal development and survival but, in many cases, the underlying mechanisms are poorly understood. *C. elegans* larval development is an ideal system in which to study this problem. *C. elegans* employ two distinct but interrelated biological timing mechanisms to regulate progression through larval development. The heterochronic pathway ensures that stage-specific cellular events happen at the correct time and in the correct order, while a molt timer ensures the proper timing of each molt in relation to developmental progression. Animal survival depends on precise

coordination of molting with developmental progression but the mechanisms that ensure this coordination are poorly understood. LIN-42, the *C. elegans* homolog to the circadian clock protein PERIOD2 (PER2), stands out for its unusual role as a regulator of both stage-specific coordination are poorly understood. LIN-42, the *C. elegans* homolog to the circadian clock protein PERIOD2 (PER2), stands out for its unusual role as a regulator of both stage-specific cellular events, and the precise timing and execution of molting. The key domains conserved between LIN-42 and PER2 are essential for PER2 function in regulating circadian rhythms. In mammals, circadian clocks are controlled by a transcription-translation feedback loop involving PER2 expression and degradation. The stability of PER2 is largely determined through its interaction with Casein Kinase I δ (CK1 δ). This kinase binds to and phosphorylates PER2 at one of two regions leading to either stabilization or degradation of PER2. Sequence analysis indicates two highly conserved kinase-binding motifs, and our *in vitro* pull-down assays show that these conserved domains in LIN-42 can bind CK1 δ suggesting that a common mechanism may anchor the kinase to LIN-42. The kinase domain of CK1 δ has a 79% sequence identity with the *C. elegans* kinase KIN-20. While we have been unable to purify recombinant KIN-20 thus far, mammalian CK1 δ phosphorylates the LIN-42 C-terminus to a similar degree and within the same timeframe as CK1 δ phosphorylation of a PER2 substrate. Purified LIN-42 lacking the conserved kinase binding motifs has weaker binding to CK1 δ and reduced phosphorylation of the LIN-42 C-terminus compared to wild type LIN-42 protein. When we engineered the equivalent mutations into the *lin-42* endogenous locus, we observed profound developmental delay as well as extended and asynchronous molts. Together, these data suggest that PER2/LIN-42 phosphorylation by CK1 δ kinases is evolutionarily conserved and that this mechanism may be employed to coordinate developmental timing.

Introduction:

Biological clocks

Every living organism possesses innate molecular mechanisms that control physiology and development. These biological clocks direct periodic expression patterns of certain genes, which in turn direct periodic changes in cellular and physiological activities that occur on a daily, seasonal, yearly, or other regular cycle. These cyclical or periodic changes are referred to as rhythms and are characterized by the period with which they occur relative to a day.

Ultradian rhythms include sleep cycles and cellular respiration cycles and have a period of less than 24-hours so that the cycle may repeat multiple times within a day (Schulz and Lavie 1985; Halberg et al. 1965). Infradian rhythms, on the other hand, have a period greater than 28-hours, but less than one year and can include menstrual cycles, seasonal migration patterns, and seasonal breeding patterns (Mahesh 1985; Halberg et al. 1965) The

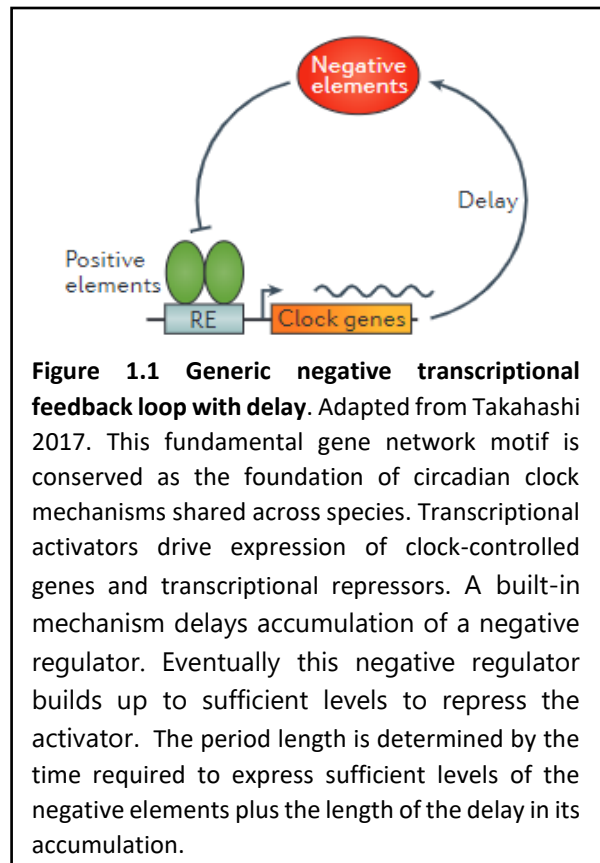


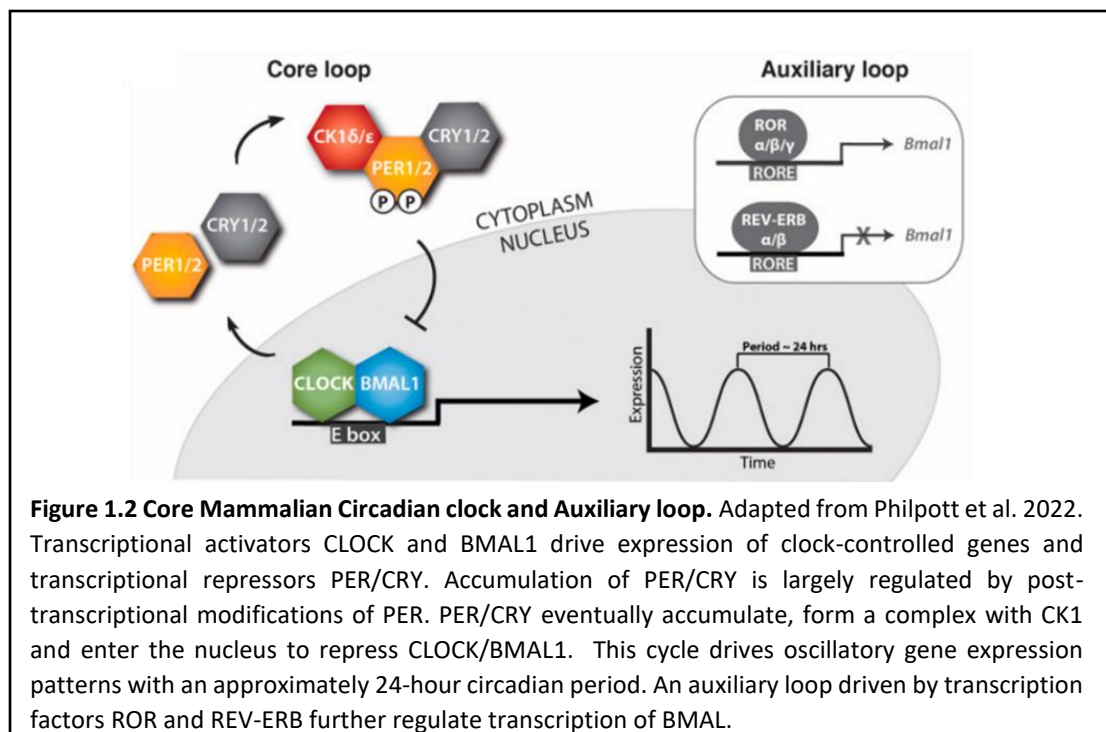
Figure 1.1 Generic negative transcriptional feedback loop with delay. Adapted from Takahashi 2017. This fundamental gene network motif is conserved as the foundation of circadian clock mechanisms shared across species. Transcriptional activators drive expression of clock-controlled genes and transcriptional repressors. A built-in mechanism delays accumulation of a negative regulator. Eventually this negative regulator builds up to sufficient levels to repress the activator. The period length is determined by the time required to express sufficient levels of the negative elements plus the length of the delay in its accumulation.

most well-characterized biological clocks direct circadian rhythms, which exhibit a periodicity of approximately 24 hours, are found in nearly all living organisms, and coordinate a wide range of biological processes with the 24-hour night/day cycles of the

earth. Circadian clocks are thought to be a product of convergent evolution because, while specific components of circadian clocks diverge across species and kingdoms, the fundamental design is generally conserved (Doherty and Kay 2010; Bell-Pedersen et al. 2005; Young and Kay 2001; Dunlap 1999). Namely, circadian rhythms are generated by cell-autonomous negative transcriptional feedback loops with a built-in delay (Alon 2007) (Fig. 1.1). Depending on the organism, this mechanism can be more complicated and can involve additional layers of regulation at every stage of gene expression, but the underlying 'network motif' is conserved (Takahashi 2017).

In mammals, the core circadian clock is driven by a transcription-translation feedback loop that consists of two transcriptional activators: circadian locomotor output cycles protein kaput (CLOCK) and brain and muscle ARNT-like 1 (BMAL1). CLOCK and BMAL1 heterodimerize and drive expression of a large number of clock-controlled genes including transcriptional repressors PERIOD (PER1, PER2 and PER3) and cryptochrome (CRY1 and CRY2) (Takahashi 2017; Aryal et al. 2017). PER and CRY proteins form a complex together with the serine/threonine kinases casein kinases (CK1 δ) and/or (CK1 ϵ) and translocate to the nucleus where they repress the activity of CLOCK/BMAL1, thereby inhibiting their own expression (Gallego and Virshup 2007; Gekakis et al. 1998; Lee et al. 2001; Lowrey and Takahashi 2011). Once PER and CRY levels have decreased, the repression is relieved and CLOCK/BMAL1 drive expression again to start a new cycle (Gallego and Virshup 2007; Preußner and Heyd 2016) (Fig. 1.2). To maintain the 24-hour period of circadian rhythms, a delay between the activation of transcription and the repression of transcription is required. This delay is accomplished, in part, by post-translational modifications of the transcriptional

repressor PER2 that determine its stability and therefore regulate its accumulation (Crosby and Partch 2020). Circadian rhythms and other biological clocks in mammals are exceptionally complicated. There are many additional layers of regulation, from well-studied accessory transcriptional feedback loops that help drive rhythmic expression of core clock proteins, to an ever-growing litany of post-transcriptional modifications that regulate their activity and function (Crosby and Partch 2020; Liu et al. 2008; Ikeda et al. 2019). The current understanding of circadian clocks in mammals indicates a master clock in the hypothalamus responsible for synchronizing peripheral clocks located in every cell of the body (Albrecht 2012; Dibner et al. 2010; Mohawk, Green, and Takahashi 2012). The mechanisms utilized for this coordination and integration remain unclear.



***C. elegans* developmental progression and the molt timer:**

C. elegans is an ideal system in which to tease apart the underlying mechanisms that control and integrate biological timekeeping. Its developmental anatomy has been described in extraordinary detail; cell differentiation patterns and morphological events are almost perfectly predictable throughout its development (Kimble and Hirsh 1979; Sulston et al. 1983; Sulston and Horvitz 1977). Two independent, but interconnected, biological timers drive their progression through larval development. The heterochronic pathway regulates temporal identities such as stage-specific cell differentiation patterns, and the molt timer controls the periodicity of molt cycles and coordinates apical extracellular matrix regeneration, and shedding of the old skin (cuticle) (Tennessee et al. 2006; Rougvie

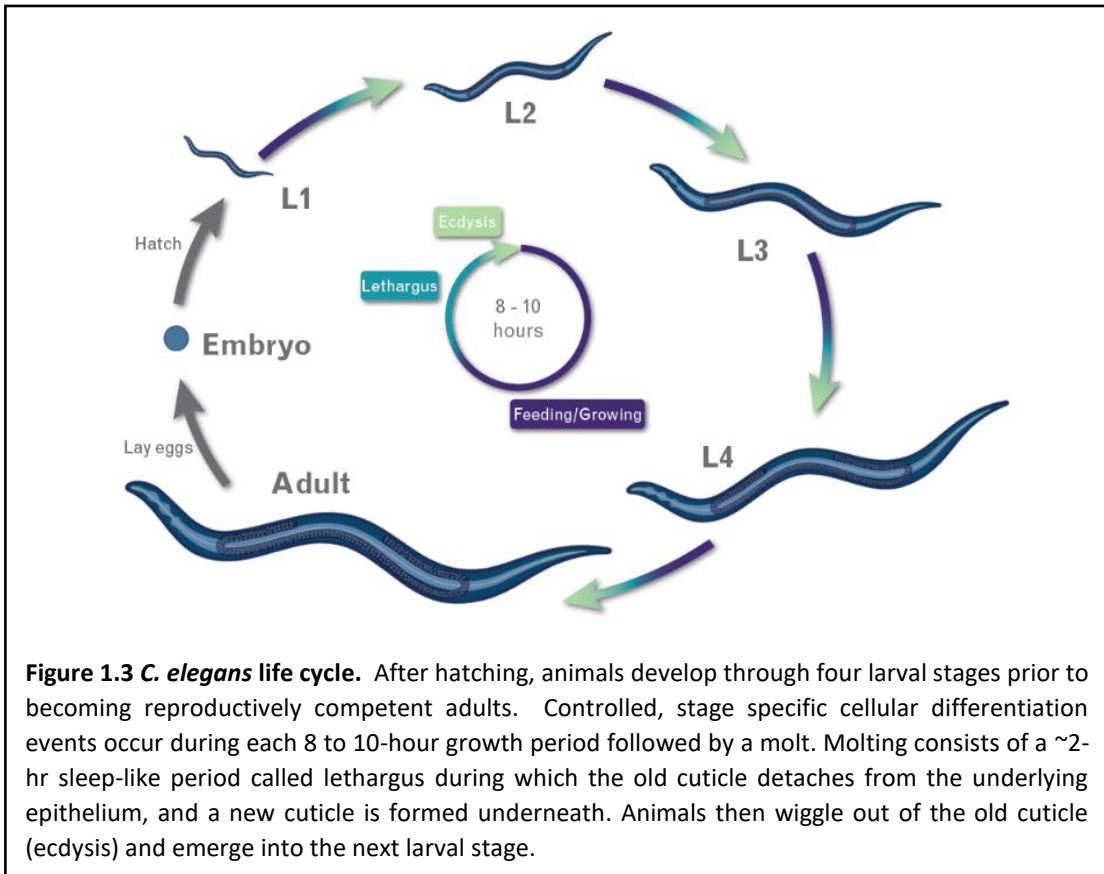


Figure 1.3 *C. elegans* life cycle. After hatching, animals develop through four larval stages prior to becoming reproductively competent adults. Controlled, stage specific cellular differentiation events occur during each 8 to 10-hour growth period followed by a molt. Molting consists of a ~2-hr sleep-like period called lethargus during which the old cuticle detaches from the underlying epithelium, and a new cuticle is formed underneath. Animals then wiggle out of the old cuticle (ecdysis) and emerge into the next larval stage.

and Moss 2013; Monsalve and Frand 2012; Moss 2007; Lažetić and Fay 2017) *C. elegans* hatch from the embryo into the first larval stage with precisely 558 cells (Gilbert and Barresi 2000) They develop through four larval stages, each defined by a tightly regulated series of stage-specific cellular and morphological events that are so invariable that we commonly use cell morphology to determine the age of an animal. *C. elegans* hermaphrodites reach adulthood with exactly 959 somatic cells, and we know precisely when each cell was formed, where it was formed, and where it should be located (Herman 2006). The genes responsible for ensuring that stage-specific events happen at the correct time and in the correct sequence are referred to as heterochronic genes and are members of a well-established biological timing mechanism called the heterochronic pathway (Rougvie and Moss 2013; Ambros and Horvitz 1984; Ambros 1989).

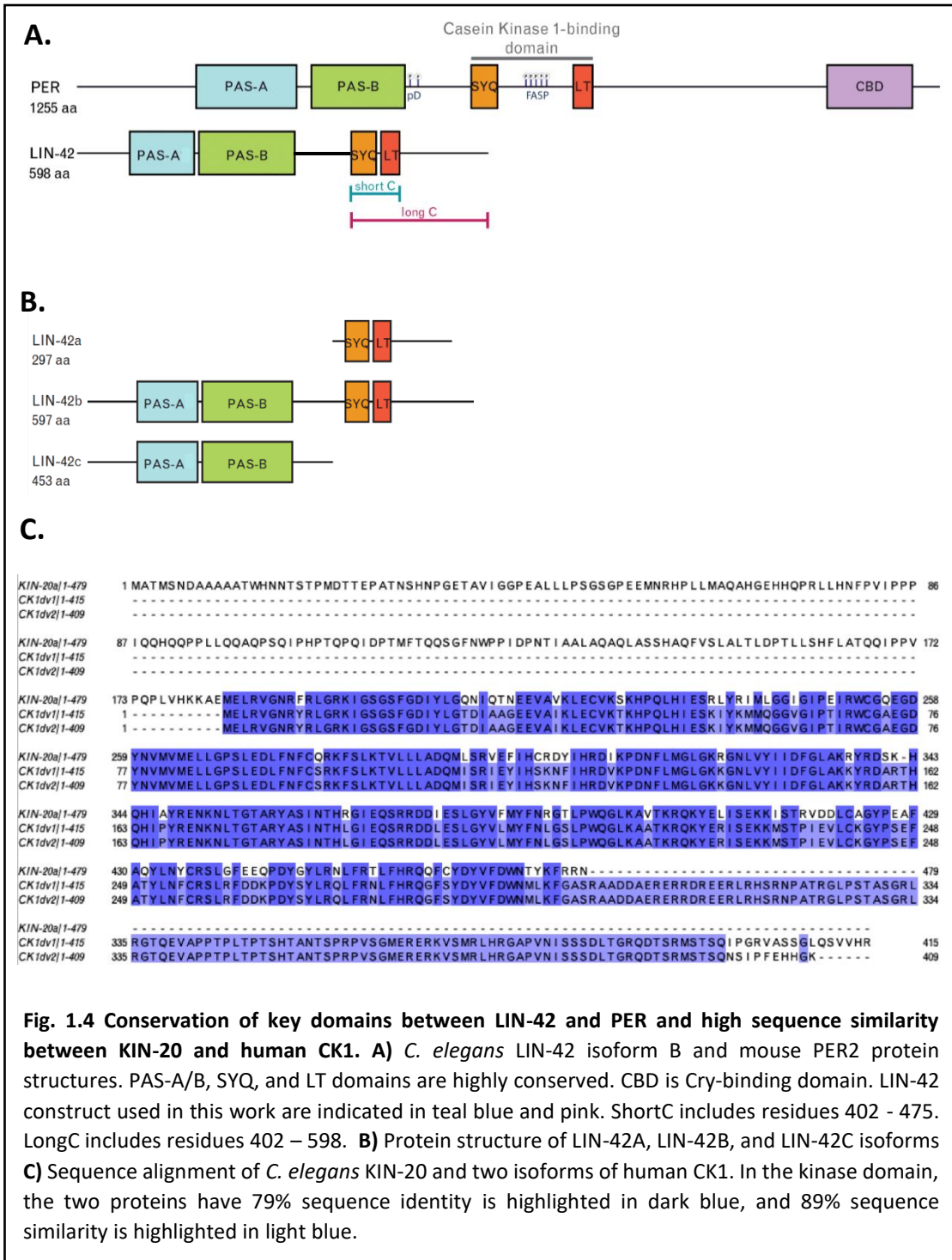
A molt marks the transition between each larval stage. Molting is a large-scale metamorphic event involving the execution of a complex gene expression program that ultimately leads to apical extracellular matrix remodeling and regeneration of a new cuticle (Singh and Sulston 1978; Iwanir et al. 2013; Lažetić and Fay 2017; Hendriks et al. 2014). Molting begins with a period of lethargus, a sleep-like state lasting 2-3 hours (Singh and Sulston 1978). During lethargus, animals partially detach from the old cuticle (apolysis) and a new cuticle is synthesized underneath (Singh and Sulston 1978; Iwanir et al. 2013). Once the new cuticle is fully synthesized, animals wiggle out of the old cuticle (ecdysis) and begin a new larval stage (Singh and Sulston 1978; Lažetić and Fay 2017).

The periodicity of the molt cycles is also tightly regulated; molts occur at regular 8-10 hour intervals at 25°C and must be precisely coordinated with stage-specific developmental

progression (Monsalve and Frand 2012; Edelman et al. 2016; Monsalve et al. 2011).
Uncoupling of the heterochronic pathway and the molt timer through pharmacological activation of a nicotinic receptor during the second larval stage resulted in lethality; developmental progression was slowed, but the molt cycle continued so that animals began to molt before stage-specific cellular events were completed (Ruaud and Bessereau, 2006). The mechanisms that accomplish this regularity and coordination remain unclear, but several key players have been identified. Most notably, *lin-42*, the *C. elegans* homolog to mammalian and *Drosophila* PERIOD (PER) proteins, is an established member of the heterochronic pathway where it temporally regulates seam cell dynamics during larval development by negatively regulating a number of micro-RNAs (Perales et al. 2014; Tennessen et al. 2006; McCulloch and Rougvie 2014; Van Wynsberghe et al. 2014). *lin-42* is unique among heterochronic genes for the molting phenotypes produced when it is mutated. Generally, molting phenotypes caused by mutations to heterochronic genes result from inappropriate cessation or continuation of the molting program leading to too few molts or too many molts (Ambros and Horvitz 1984; Ambros 1989; Ambros and Ruvkun 2018). Mutations in *lin-42*, however, affect not just the number of molts, but also the execution and timing of each molt (Monsalve et al. 2011; Edelman et al. 2016). As a result, *lin-42* is thought to coordinate molting cycles with developmental progression, although the mechanisms involved in this regulation are unclear (Tennessen et al. 2006; Monsalve and Frand 2012).

***Lin-42* is the *C. elegans* homolog to mammalian circadian clock protein PER2**

The structural and functional homology shared between LIN-42, and its mammalian homolog PER2 is striking. PER2 and LIN-42 both function to regulate the timing of biological processes. Mutations in PER2 alter the timing of circadian rhythms so that the circadian period is either shortened or extended, and mutations in LIN-42 alter the period between molts and uncouple molting from developmental progression (Steinlechner et al. 2002; Masuda et al. 2020; Monsalve et al. 2011; Edelman et al. 2016). Expression of PER2 and LIN-42 oscillate in time with their respective cycles. PER2 mRNA and protein levels peak one time in each 24-hour period (Shearman et al. 1997; Lee et al. 2011; Chen et al. 2009; Tei et al. 1997). Similarly, *lin-42* mRNA expression oscillates in time with *C. elegans* 8 to 10- hour molt cycles so that mRNA levels peak once during each intermolt period (Jeon et al. 1999; Tennessen et al. 2006). Additionally, key structural domains are highly conserved between LIN-42 and PER2, namely, the PAS domains and the CKBD, SYQ/ LT domains, which are essential for the circadian function of PER2 (Militi et al. 2016; Zheng et al. 1999; Hennig et al. 2009; Beesley et al. 2020; Lee et al. 2004; Eide et al. 2005) (Fig. 1.4A; Sup. Fig 2). Some Structural differences are also apparent between LIN-42 and PER2, which makes sense given the differences in the functions of the two systems. For example, circadian rhythms are temperature compensated, while *C. elegans* development is expressly not, and there is evidence suggesting that regulation PER2 by CK1 δ phosphorylation is a key component in of the temperature compensation mechanism (Shinohara et al. 2017; Isojima et al. 2009).



In *C. elegans*, the *lin-42* locus

expresses three distinct

protein isoforms that

separate these key domains

(Edelman 2016) (Fig. 1.5).

Edelman et al. (2016)

reported strong evidence for

lin-42a and *lin-42b* based on

RNA-seq data. They also

noted that support for *lin-42c*

comes from 3'RACE (Rapid

amplification of cDNA ends) sequence tags (WormBase release WS252). *lin-42b*, the longest

isoform with the most homology to PER2, contains both the PAS domains and the SYQ/LT

domains. *lin-42a* and *lin-42c* are smaller, non-overlapping isoforms expressed from distinct

promoters. *lin-42a* contains the SYQ/LT domains but not the PAS domains, while *lin-42c*

contains the PAS domains but not the SYQ/LT domains. (Jeon et al. 1999; Tennessen et al.

2006). Studies characterizing and comparing two hypomorphic mutations and a null

mutation suggest that isoforms containing the SYQ/LT domains are key to LIN-42 function in

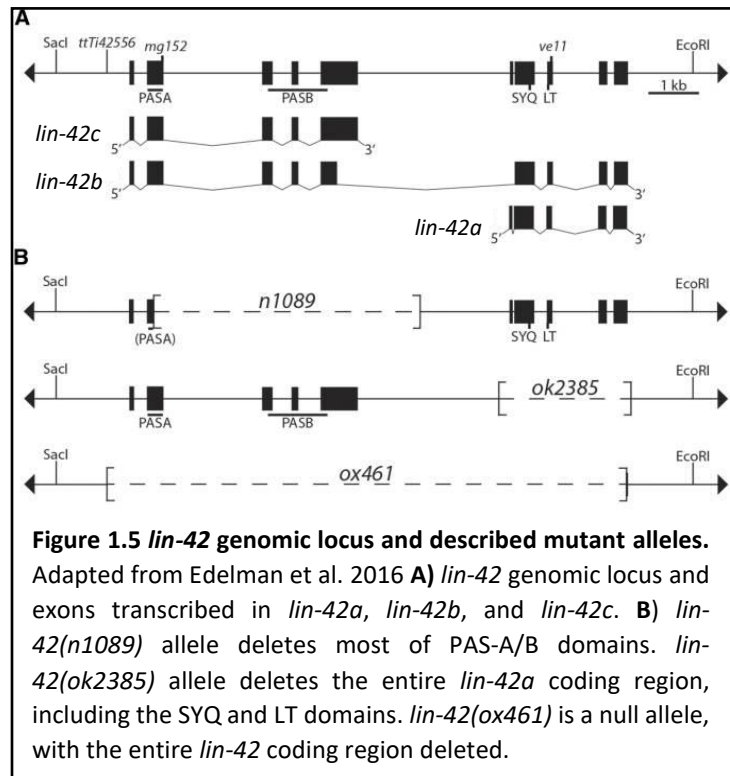
regulating molting and molt timing (Tennessen et al. 2006; Monsalve et al. 2011; Edelman et

al. 2016). *lin-42(ok2385)* an allele that deletes *lin-42a* and the corresponding portion of *lin-*

42b, results in developmental delay, egg laying defects, and severe molting defects,

including asynchronous molts, fewer molts, and larval arrest caused by failure to detach

from and shed the previous cuticle. (Monsalve et al. 2011). *lin-42(n1089)*, an allele deleting

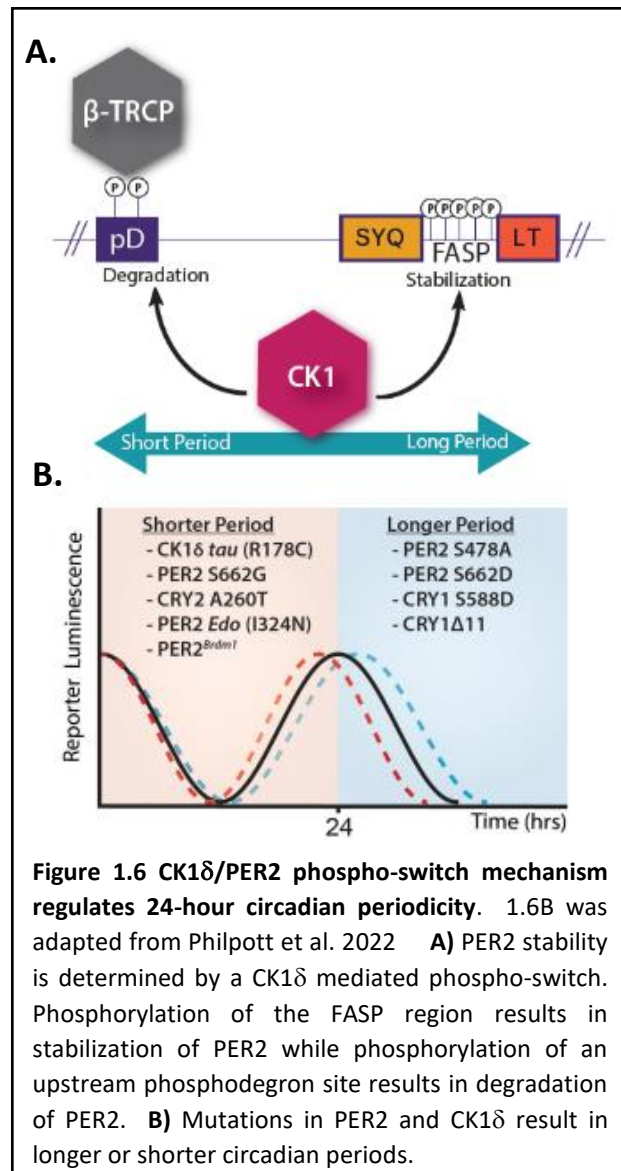


lin-42c, the PAS-containing region, and the corresponding portion of *lin-42b*, causes comparably subtle heterochronic defects but is not required for proper timing or execution of the molts (Tennessen et al. 2006). Additionally, deletion of the entire *lin-42* coding region results in similar but more severe phenotypes compared to the partial deletions, suggesting that the PAS-containing region does have some role in molting and molt timing (Edelman et al. 2016). In mammals, the region encompassing the SYQ and LT domains, referred to as the Casein Kinase-Binding Domain (CKBD), is bound by CK1 δ and CK1 ϵ and is essential for regulating the period of circadian rhythms (Eide et al. 2005; Lee et al. 2004; Toh et al. 2001; Xu et al. 2007). Mutations to either CK1 δ or the CKBD of PER2 that disrupt CK1 binding result in longer or shorter circadian periods and can correspond to human disease (Parico and Partch 2020; Hirano et al. 2016; Patke et al. 2017; Xu et al. 2005; Xu et al. 2007).

Binding and phosphorylation of PER2 by CK1 δ regulates circadian periods: phospho-switch mechanism. The ~24-hour periodicity of circadian rhythms depends, in part, on the accumulation and degradation of PER2 in the cytoplasm. Transcriptional activation by CLOCK and BMAL1 occurs in the daytime, resulting in the accumulation of PER and CRY proteins in the cytoplasm later in the day (Lee et al. 2001). At night, when PER and CRY proteins accumulate to a sufficient level, they form a complex with CK1 δ , migrate to the nucleus and repress the activity of CLOCK/BMAL1 until levels of PER and CRY are reduced and the cycle repeats (Aryal et al. 2017; Philpott et al. 2022) (Fig. 1.2). After transcription, the stability and accumulation of PER2 are largely determined by the balance of phosphorylation by CK1 between two regions. Phosphorylation of a region in between the SYQ and LT domains

referred to as the familial advanced sleep phase (FASP) region results in stabilization of PER2, allowing its accumulation in the cytoplasm (Hirano et al. 2016; Crosby and Partch 2020; Aryal et al. 2017; Lee et al. 2001; Toh et al. 2001).

Phosphorylation of an upstream phosphodegron region results in PER2 ubiquitination and degradation of PER2, delaying its accumulation (Hirano et al. 2016; Crosby and Partch 2020) (Fig. 1.6A). Mutations in CK1 δ and PER2 result in longer or shorter circadian periods (Parico and Partch 2020; Hirano et al. 2016; Toh et al. 2005; Xu et al. 2005). Thus, CK1



plays an integral role in dictating circadian timing through regulating PER2 stability (Fig 1.6B).

Similarly, KIN-20, the *C. elegans* homolog to CK1 δ , appears to have an important function in the temporal regulation of *C. elegans* development and molting cycles, although the exact mechanisms underlying this role are largely unexplored (Banerjee et al. 2005; Rhodehouse

et al. 2018). In this work, we investigate whether elements of the interactions between PER2 and CK1 δ are conserved in *C. elegans* LIN-42 and KIN-20. We show that CK1 δ can bind and phosphorylate a LIN-42 substrate *in vitro* and that the conserved CKBD domains are required for a robust interaction. Further, we show that deletion of the SYQ and LT domains, two highly conserved alpha helices within the CKBD, results in upregulation of LIN-42::GFP, but severe developmental abnormalities and molting defects are only observed once those deletions are extended to encompass the whole CKBD.

Results:

LIN-42 SYQ and LT domains are conserved enough to mediate an interaction with CK1 δ

PER2 and CK1 δ have a very tight and stable binding interaction that allows for phosphorylation of PER2 by CK1 δ which is critical for regulating the mammalian circadian clock (Hirano et al. 2016; Crosby and Partch 2020; Aryal et al. 2017; Lee et al. 2001; Liu et al. 2019). Given that the kinase binding motifs of PER2 are highly conserved in LIN-42 and the extensive sequence identity shared between CK1 δ and KIN-20 in their kinase domains, we first set out to determine if KIN-20 binds to and phosphorylates LIN-42 using a biochemical approach. Unfortunately, we have not been able to purify recombinant protein from bacteria or insect cells as KIN-20 has been exclusively insoluble or poorly behaved. However, there is precedent for using mammalian CK1 δ on *C. elegans* substrates to provide functional insight into KIN-20 (LaBella et al. 2020). We purified two distinct C-terminal LIN-42

fragments. A 196 amino acid fragment (longC) includes the majority of *lin-42a*, while a smaller, 73 amino acid fragment (shortC) contains only the conserved CKBD (Fig.1.4A, Sup. 1). We performed pull-down assays with biotinylated LIN-42 fragments to test for interaction with KIN-20. LIN-42 longC showed a near stoichiometric interaction between CK1 δ and the C-terminus of LIN-42 (Fig. 1.7A). To confirm that this interaction is mediated by the conserved CKBD, which encompasses the SYQ and LT domains of LIN-42, we performed similar pull-down assays using LIN-42 longC fragments lacking either the SYQ domain or the LT domain. Removing either domain resulted in decreased interaction with mammalian CK1 δ , although deletion of the LT domain resulted in a slightly larger decrease (Fig. 1.7A). These data suggest that the kinase binding domain of LIN-42 is conserved enough to mediate an interaction with mammalian CK1 δ and that both the SYQ and LT domains are necessary for the robustness of this interaction.

CK1 δ phosphorylates the C-terminus of LIN-42 *in vitro* and deletion of the SYQ and LT domains (CKBD) results in decreased kinase activity.

To determine if CK1 δ binding leads to phosphorylation of the LIN-42 C-terminus, we performed kinase assays using ³²P-labeled ATP. CK1 δ was able to phosphorylate both LIN-42 constructs; however, significantly higher phosphorylation levels were observed in longC compared to shortC (Fig. 1.7B). These data suggest that the unstructured C terminal tail could help facilitate binding or be a target of CK1 δ phosphorylation. ³²P-ATP kinase assays were repeated over a 120-minute time course along with substrate titrations to compare CK1 δ phosphorylation of longC and mammalian PER2 FASP substrate. CK1 δ phosphorylated LIN-42 longC to a similar degree and within the same timeframe as CK1 δ phosphorylation of

a PER2 substrate (Fig. 1.6C). Deleting the SYQ domain, LT domain, or both resulted in decreased phosphorylation of both the longC and shortC LIN-42 constructs in a stepwise fashion, with the SYQ deletion having the least impact and the double deletion having the most (Fig. 1.7B,D). Taken together, these data indicate that the CKBD in LIN-42 is conserved enough to facilitate both binding and phosphorylation by CK1 δ and that the SYQ and LT domains play an important role in mediating this interaction.

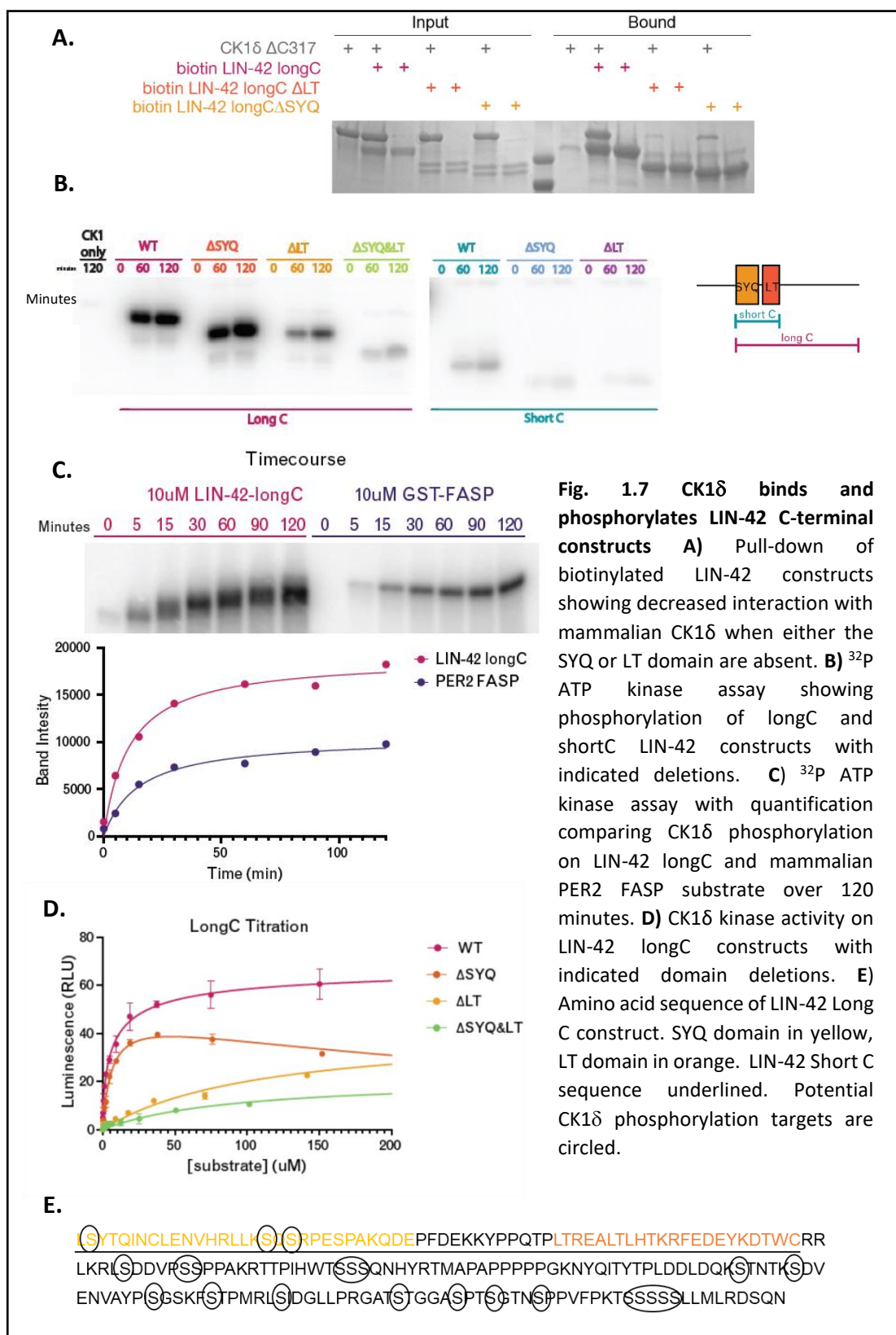


Fig. 1.7 CK1δ binds and phosphorylates LIN-42 C-terminal constructs **A)** Pull-down of biotinylated LIN-42 constructs showing decreased interaction with mammalian CK1δ when either the SYQ or LT domain are absent. **B)** ³²P ATP kinase assay showing phosphorylation of longC and shortC LIN-42 constructs with indicated deletions. **C)** ³²P ATP kinase assay with quantification comparing CK1δ phosphorylation on LIN-42 longC and mammalian PER2 FASP substrate over 120 minutes. **D)** CK1δ kinase activity on LIN-42 longC constructs with indicated domain deletions. **E)** Amino acid sequence of LIN-42 Long C construct. SYQ domain in yellow, LT domain in orange. LIN-42 Short C sequence underlined. Potential CK1δ phosphorylation targets are circled.

CKBD deletion mutations cause drastic upregulation of LIN-42::GFP expression in *C. elegans* but do not cause developmental or molting defects

To gauge the physiological importance of the conserved CKBD in *C. elegans* we used CRISPR/Cas9-mediated genome editing to introduce deletion mutations into a *C. elegans* strain containing a GFP::AID::3XFLAG tag at the 3' end of the endogenous *lin-42* locus. We refer to this parent strain as ***lin-42::GFP*** for the remainder of this document. We deleted a nine amino acid portion of the SYQ domain (*lin-42(SYQΔ403-411)*), and a 21 amino acid portion of the LT domain (*lin-42(LTΔ444-464)*). We also made a strain containing both individual deletions (*lin-42(SYQΔ403-411)*, (*LTΔ444-464*)) (Fig. 1.8A, Sup. Fig. 1). Note that the portion of the SYQ domain removed from our mutant is smaller than the portion removed from the constructs described above. We initially made this smaller deletion as we tried to make the most efficient edit based on PAM orientation and predicted crRNA efficiency (Farboud and Meyer 2015; Farboud et al. 2019; Concordet and Haeussler 2018). Given the lack of impact this deletion had *in vitro*, it has not been a priority to generate a new ΔSYQ mutant that is more closely equivalent. We observed a small but statistically relevant extension in the length of time these mutants spent in larval stages and a small but statistically relevant extension in the length of each molt compared to *lin-42::GFP* (Fig. 1.9 C,D, Sup. Fig. 2). The double mutant exhibited a relatively more severe delay that persisted through all four larval stages and all 4 molts while *lin-42(SYQΔ403-411)* and *lin-42(LTΔ444-464)* mutants exhibited relatively shorter extensions observed only in the first and fourth molts and larval stages. We observed no other significant developmental abnormalities in our *lin-42(SYQΔ403-411)*, *lin-42(LTΔ444-464)*, or *lin-42(SYQΔ403-411)*, (*LTΔ444-464*)

mutants. All reached adulthood within three days of hatching when cultured at 20°C and exhibited no significant molting defects, larval arrest, or egg laying defects (Fig. 1.8, 1.9, Sup. Fig 2).

Interestingly, we did observe an increase in LIN-42::GFP expression throughout larval development (Fig. 1.8E). Deleting the SYQ domain resulted in a slight but noticeable increase in LIN-42::GFP expression compared to wild type. By contrast, the LT deletion and the double deletion caused a significant upregulation of LIN-42::GFP, indicating that these domains play some role in regulating LIN-42 levels *in vivo*. Surprisingly, this upregulation of LIN-42 did not correspond to developmental phenotypes associated with previously described *lin-42* mutants. It is worth noting that we did see a slight developmental delay and a small percentage of dumpy adults in *lin-42::GFP*, presumably because the large GFP tag interferes with *lin-42* activity. As expected, equivalent mild phenotypes were observed in mutants made in this background. For this reason, all mutant strains described in the remainder of this document were made in both wild type and *lin-42::GFP* backgrounds, and phenotypic analyses were performed on mutants in a wild-type background. The *lin-42::GFP* background was used primarily to test the impact of a given mutation on LIN-42::GFP expression.

Deletion of the entire CKBD results in developmental delay and asynchronous molts but does not noticeably affect LIN-42::GFP expression

We used a serial truncation approach to identify regions of the *lin-42* locus necessary for its function in regulating and coordinating molting and developmental timing. We first deleted 194 amino acids from the C-terminal end of LIN-42 relative to the sequence of isoform B

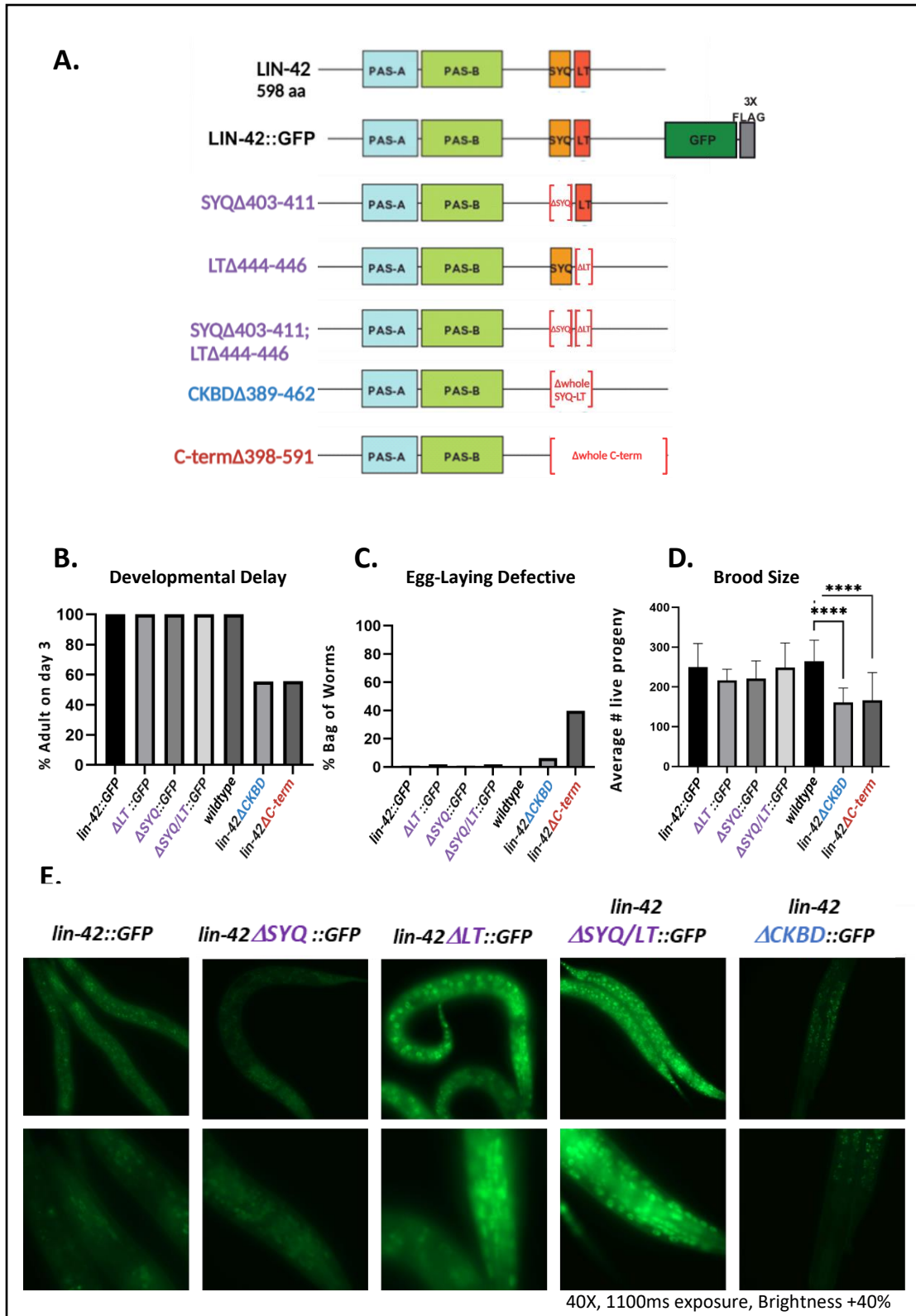
(*lin-42(C-term Δ 398-591)*) in a wild-type background, essentially removing all of *lin-42a* (Fig. 1.8A, Sup. Fig. 1). As expected, severe developmental abnormalities were observed, similar to those previously described in *lin-42a* mutants (Monsalve et al. 2011). Over 40% of *lin-42(C-term Δ 398-591)* mutants failed to complete the fourth molt or reach adulthood by day three after hatching when cultured at 20°C, compared to 100% of wild-type animals (Fig. 1.8B, 1.9A,B). Interestingly, the first three molts, while delayed and extended, occurred synchronously. The fourth larval stage and the fourth molt were severely extended in of *lin-42(C-term Δ 398-591)* mutants, and just over 40% of animals did not complete a fourth molt after 84 hours (Fig. 1.9B-D, Sup Fig. 2). Of those that did reach adulthood, nearly 40% were egg laying defective, exhibiting a bag-of-worms phenotype and the remaining 60% that became reproductively competent adults, had significantly smaller average brood sizes compared to wild-type animals (Fig. 1.8C,D).

We then focused our truncation approach on the conserved CKBD region to determine whether disruption of the sequence necessary for kinase binding and phosphorylation of LIN-42 resulted in the developmental delay and molting phenotypes we observed. Since deletion of individual SYQ and LT domains resulted in only mild developmental delay, we expanded that deletion to encompass the entire conserved CKBD region, including the short unstructured region between the SYQ and LT domains (*lin-42(CKBD Δ 398-462)*) (Fig. 1.8A, Sup. Fig. 1). Expanding the CKBD deletion resulted in developmental defects similar to our *lin-42(C-term Δ 398-591)* mutants but with some key differences. We observed a similar developmental delay, with just under 45% of animals failing to reach adulthood by day three at 20°C after hatching, and a similar, but slightly less severe extensions in the length of each

molt. *lin-42(CKBDΔ398-462)* mutants exhibited asynchronous molt patterns beginning at the L2 molt and persisting until adulthood. We observed significantly less penetrant egg-laying defects, with only 4% of animals presenting with a bag of worms phenotype. *lin-42(CKBDΔ398-462)* animals that reached adulthood had significantly lower average brood sizes compared to wild type, similar to *lin-42(C-termΔ398-591)* mutants.

Figure 1.8: Deletions of the conserved CKBD region results in developmental abnormalities.

A) Schematic of deletions made in *lin-42*. Residue numbers correspond to LIN-42B isoform. Individual SYQ and LT deletions (*lin-42(SYQΔ403-411)*, *lin-42(LTΔ444-464)*, and *lin-42(SYQΔ403-411)*, *(LTΔ444-464)*) were generated only in a *lin-42::GFP* background. *lin-42(CKBDΔ398-462)* and *lin-42(C-termΔ398-591)* alleles were generated in both wild-type and *lin-42::GFP* backgrounds. In subsequent images allele names are color coded and abbreviated. Purple Δ SYQ, Δ LT, and Δ SYQ/LT correspond to *lin-42(SYQΔ403-411)*, *lin-42(LTΔ444-464)*, and *lin-42(SYQΔ403-411)*, *(LTΔ444-464)*. Blue Δ CKBD is *lin-42(CKBDΔ398-462)*, and red Δ C-term is *lin-42(C-termΔ398-591)*. **B)** Percentage of animals that were adults by day 3 after hatching. n>24 for all strains. **C)** Percentage of animals with bag of worms phenotype. n>21 for all strains. C. Average number of live progeny. n>12 for all strains. Statistical significance was determined using a two-tailed unpaired Student's t-test. P < 0.05 was considered statistically significant. **** indicates P < 0.0001 **D)** Representative images of late L3 or early L4 *lin-42::GFP* animals with indicated domain deletions. Animals staged based on germline morphology. Images acquired at 40X magnification, 1000ms exposure, and brightness was increased by 40% post acquisition uniformly for all images.



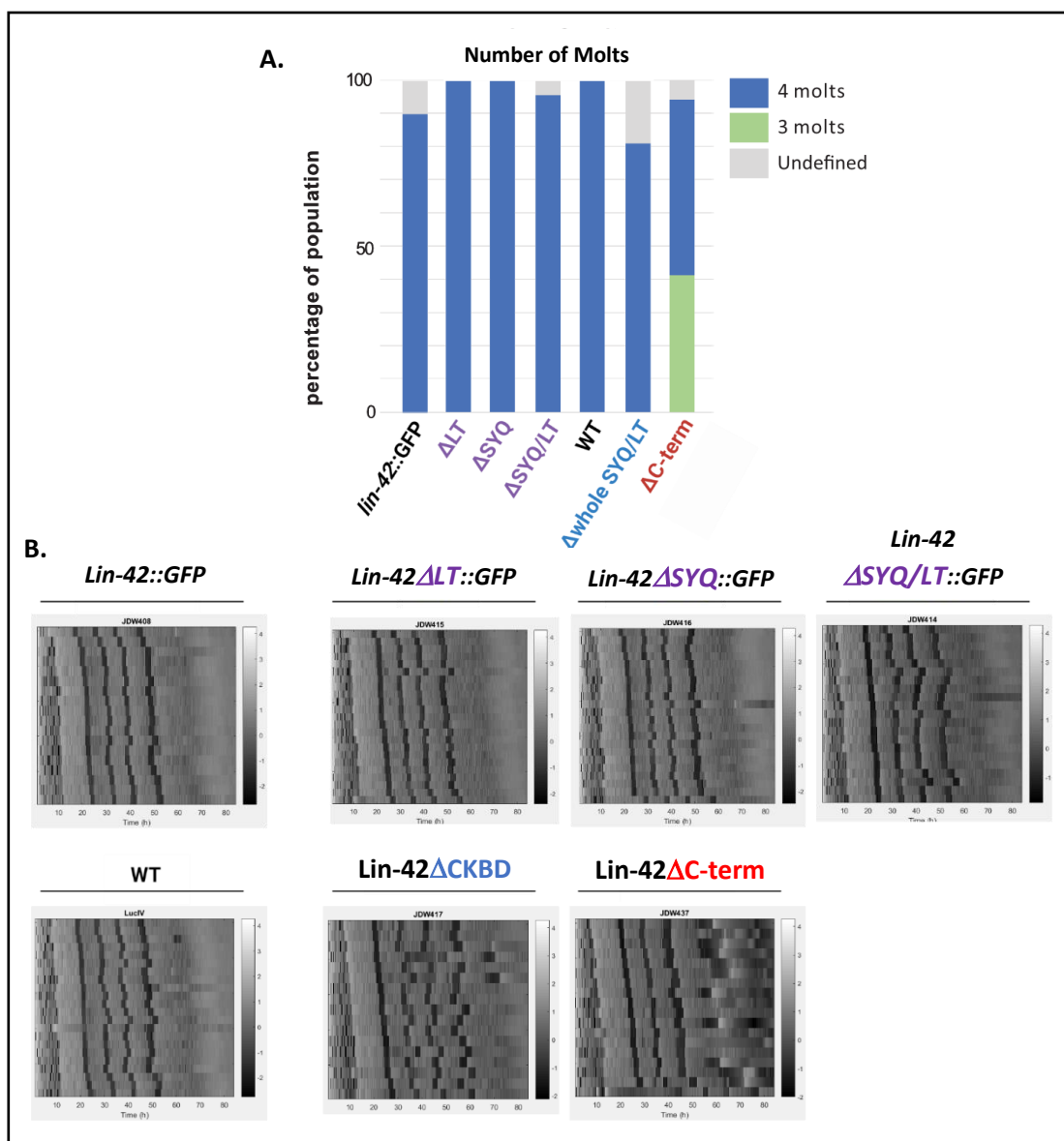
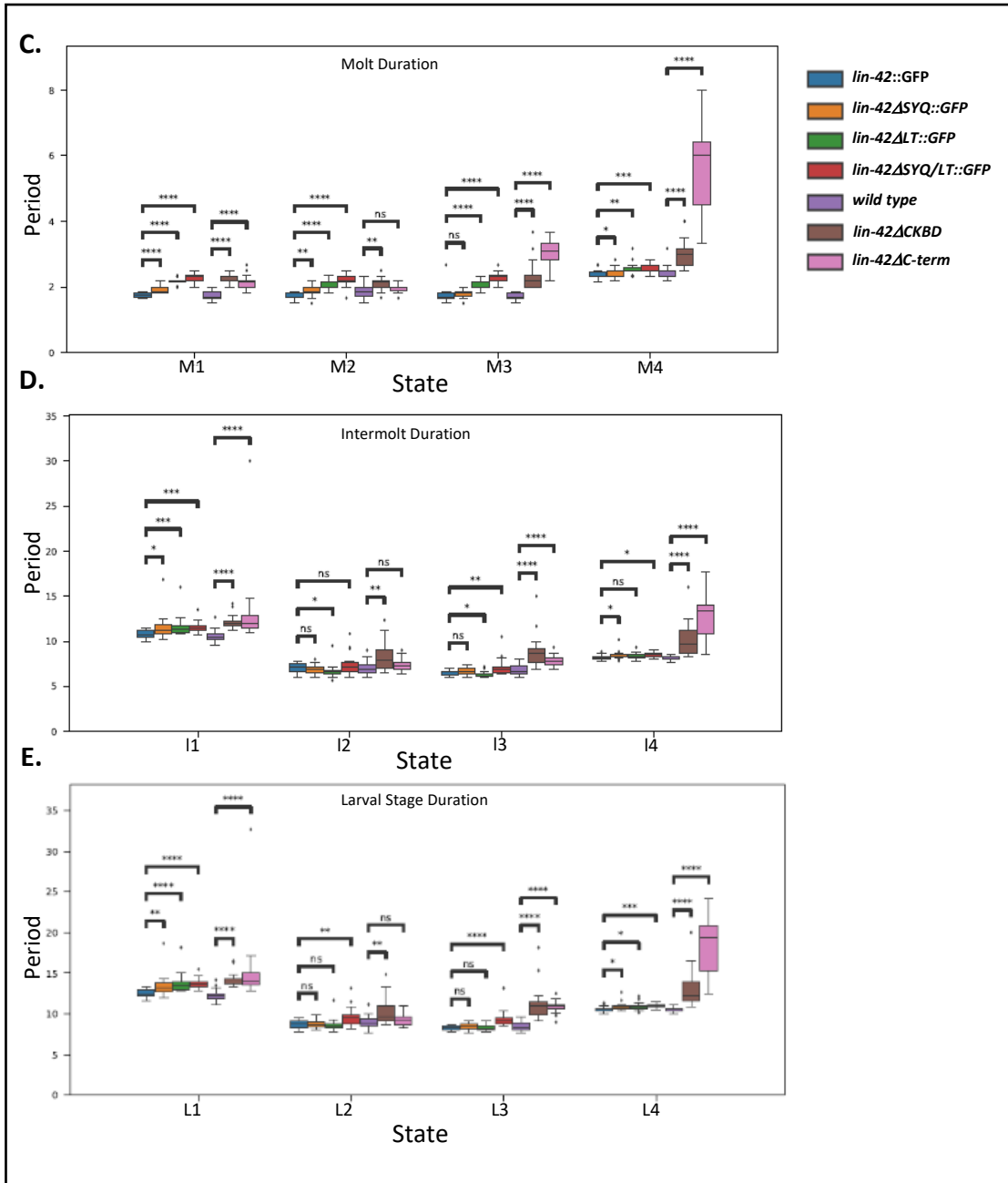


Fig. 1.9 Deletions of the conserved *lin-2* CKBD region results asynchronous molts and developmental delay. Indicated mutant alleles were crossed to a strain that expressed luciferase from a single copy integrated transgene (details in table 1). Luciferase is expressed while animals feed and signal drops during the molt when animals stop feeding. (n = 24) for all strains. In all images allele names are color coded and abbreviated. Purple ΔSYQ , ΔLT , and $\Delta SYQ/LT$ correspond to *lin-2(SYQ Δ 403-411)*, *lin-2(LT Δ 444-464)*, and *lin-2(SYQ Δ 403-411), (LT Δ 444-464)*. Blue $\Delta CKBD$ is *lin-2(CKBD Δ 398-462)*, and red ΔC -term is *lin-2(C-term Δ 398-591)* **A)** Bar plot showing number of molts observed in animals with specified allele over 84hrs. Empty wells and unreadable traces labeled as undefined. **B)** Heat maps representing luciferase activity in specified alleles. Grey represents feeding animals, Black represents lethargus. Each line represents an individual animal **C/D/E)** Boxplots of molt, intermolt, and larval stage durations in specified strains. Period is represented in hours.



Discussion

To determine the mechanisms through which LIN-42 regulates and coordinates developmental timing in *C. elegans*, we looked to the well-studied mechanisms employed by its mammalian homolog PER2. The striking similarities between LIN-42 and PER2 and the extensive sequence identity shared between their cognate kinases lead us to consider the possibility that some aspects of these timekeeping mechanisms may also be conserved. The ~24-hour period of the circadian clock depends on a tight and stable binding interaction between PER2 and CK1 δ that allows for CK1 δ kinase activity on PER2. Here we show that CK1 δ binds and phosphorylates a LIN-42 substrate *in vitro* with similar kinetics compared to a PER2 substrate and that the SYQ and LT domains are required for a robust interaction. Further, we show that deletion of the SYQ and LT domains, two highly conserved sequences that are predicted to take on alpha helical structure within the CKBD, results in dysregulation of LIN-42::GFP expression *in vivo*. However, severe developmental abnormalities and molting defects are only observed once those deletions are extended to encompass the whole CKBD.

Our *in vitro* work indicated that removing the SYQ and LT domains disrupts the interaction between CK1 δ and LIN-42 and decreases CK1 δ kinase activity on LIN-42 (Fig. 1.7A,B). These data are in agreement with recently published work demonstrating that deletion of these domains in PER2, decreases CK1 δ activity in that system and alters circadian activity. (Liu et al. 2019; Marzoll et al. 2022).

When these domains were deleted *in vivo*, presumably disrupting kinase binding, we observed a striking upregulation of LIN-42::GFP expression (Fig 1.8E). These data could suggest that LIN-42 levels depend on CK1 δ /KIN-20 kinase activity, similar to PER2 in mammals. Additional work will be necessary to determine whether the increased levels of LIN-42::GFP we observed resulted from an increase in protein stability or an overexpression at the level of transcription or translation. Upregulation of *lin-42* mRNA was not observed in a *kin-20* null mutant, however, suggesting that the upregulation we observed in LIN-42::GFP protein levels may be posttranscriptional (Rhodehouse et al. 2018).

Still perplexing is the question of why the upregulation we saw in our *lin-42(SYQ1403-411)* and *lin-42(LT1444-464)* mutants did not obviously impact developmental timing or larval progression. This result is surprising considering previous reports that forced expression of *lin-42a* from an integrated array driven by a heat shock promoter resulted in anachronistic molts and lethargy (Monsalve 2011). It is possible that LIN-42 levels in our mutants, while increased in comparison to control animals, may not reach a particular threshold of overexpression required to disrupt developmental timing. Another possibility is that there is some sort of mechanism to maintain LIN-42 activity at certain levels and mutations that reduce LIN-42 activity may trigger upregulation to compensate. We attempted to attenuate LIN-42 levels using RNAi and auxin systems to see if reducing LIN-42 levels in these mutants would result in developmental phenotypes, but our results were unclear (data not shown). Overexpression of LIN-42 in wildtype and mutant backgrounds is another avenue we could pursue to answer these questions. Further work will be necessary to fully understand this discrepancy. Interestingly, when we expanded our *in vivo* deletions to encompass the whole

CKBD, LIN-42::GFP expression appeared to decrease slightly throughout larval development compared to controls (Fig. 1.8E). Further, we observed developmental abnormalities and asynchronous molt patterns similar to those observed when the entire *lin-42a* isoform was deleted (Fig 1.8B-D, Fig. 1.9A-E). These data indicate that an intact CKBD is essential for *lin-42* function in coordinating developmental timing, further indicating a role for kinase binding and the phosphorylation state of LIN-42.

The next steps in this work will require linking the phosphorylation state of LIN-42 to the phenotypes we observe and to KIN-20 specifically. We plan to map potential phosphorylation sites on the C-terminal end of LIN-42 through mass spectrometry and then test the impact of mutations in these sites. PER2 stability is maintained through a phospho-switch mechanism. CK1 phosphorylation of a phospho-degron region results in ubiquitination and degradation of PER2 (Hirano et al. 2016; Crosby and Partch 2020; Zhou et al. 2015), while phosphorylation of the FASP region results in stabilization of PER2 (Toh et al. 2001; Philpott et al. 2020). The FASP region includes a series of five serine residues that are consecutively phosphorylated (Narasimamurthy et al. 2018). CK1 δ phosphorylation of the first 'priming' residue in this series results in the obligately sequential phosphorylation of downstream residues. We observe a cluster of serine residues between the SYQ and LT domains of LIN-42 that may be especially important given that they are located in an area left intact in our individual SYQ and LT domain deletions and that there is evidence suggesting these sites regulate CK1 activity in mammalian systems. (Philpott et al. 2022).

Some unanswered questions remain that could be interesting to explore further. In our serial truncation approach, we began by deleting the entire C-terminus and the entire PAS-

containing region (data not shown). In the circadian clock, the tandem PAS domains allow dimerization of PER proteins and are therefore critical for circadian rhythms (Yagita et al. 2000; Kucera et al. 2012; Hennig et al. 2009). Preliminary data suggested that LIN-42 PAS-B folds similarly to PER2 and that LIN-42 dimerizes *in vitro* (Data not shown). However, deletion of PAS-A and B from LIN-42 did not have any significant impact on developmental progression that we observed. We did not investigate whether they exhibit the subtle but expected heterochronic phenotypes associated with disruptions in *lin-42c*, but the lack of severe developmental phenotypes associated with these mutations suggests that dimerization is not as important for LIN-42 as it is for PER2, or that other LIN-42 domains promote dimerization. We did notice and note a significant upregulation of LIN-42::GFP levels similar to our individual *lin-42(SYQ403-411)/ (LT444-464)* mutants. I am currently working to generate a *lin-42(C-term Δ 398-591)* mutant in a *lin-42::GFP* background to compare levels of LIN-42::GFP and will continue to generate all future strains in both to continue this structure/function approach.

While it is likely we will uncover similarities in these timing mechanisms, there are sure to be differences as well. A key characteristic of the core circadian clock in mammals is that the rhythmic gene expression patterns are achieved by a feedback mechanism that is strongly influenced by PER2 levels (Chen et al. 2009). This doesn't appear to be the case in *C.*

elegans. *lin-42* mRNA continued to oscillate in mutants with non-functional LIN-42 (Jeon et al., 1999), and upregulation of LIN-42::GFP did not, in itself, result in severe perturbations in developmental timing or molting. It is clear, however, that the kinase binding domain, and therefore, the phosphorylation state of LIN-42, is essential for LIN-42 function, but it does

not appear that LIN-42 levels largely impact developmental timing. These differences make sense given that the circadian clock controls cyclical changes in behavior and physiology with an invariant ~24-hour period that is not affected by temperature (Bass and Takahashi, 2010; Buhr et al. 2010; Pittendrigh, 1954; Sweeney and Hastings, 1960). The circadian clock requires such a feedback mechanism to ensure the fidelity of these ~24-hour periods every single day for the life of an organism. *C. elegans* developmental timing, on the other hand, controls a linear progression of cell fate patterns over a set time, coordinated with a finite number of molts. The molt cycles are similar to circadian cycles, in that they are controlled by rhythmic gene expression programs, but they are not temperature compensated and the intermolt periods can be variable. A wild-type population will molt synchronously, but the intermolt periods change in response to environmental cues such as temperature and nutrient availability, to match the speed at which animals are progressing through larval stages. Interestingly, there are reports of circadian rhythms in adult *C. elegans* (Simonetta et al. 2009; Hasegawa et al. 2005; Edgar et al. 2012; De Temmerman et al. 2011), with one report linking *lin-42* (Simonetta et al. 2009). It would be interesting to further investigate the role of *lin-42* and potentially *kin-20* within that mechanism.

Supplemental Figures:



SYQ domain = **DPPLSYTQINCL**ENVHRLLSQSRPESPAKQDE in orange
 LT domain = QTPL**TREALTLHTK**FEDEYKDTWC in blue
 Deletions made highlighted in yellow

>LIN-42 isoform b protein sequence with individual SYQ and LT deletions highlighted



MEPAGHSSATHNIVPNANPTQPQLAPAMREEGATLSPNTWSSSSVEFLDDADDNRLFTCT
 FTLPHGTVLSSATYADGFHEQYL TIGDNFLARLEPKGQSFILSAAAASVKQRIFARVTPDGALR
 ACELLCEFETDRAKITVLALRSFSLQASHVSSNFHVFTFITKHSSTCALHIDYASIPYLGLLPTD
 LIGKSLAFVYSPDVHVVRQAHDHNSRGKIVKSIADLRLVAHNGSILRCQTEWSAYVNPWTRK
 MELVVARHRICSLPIGDSDVSSPPPGIQSNTLPPVMAKTFEDELRTIMNKPVPSTSRHSHHHHH
 SSLKDQNGGFANIDL GAYIDKIVEQLVNVNSTAQQQKQVAVAAAAAAQAAQAAVVATAQIRKVA
 SAPPTTST**DPPLSYTQINCL**ENVHRLLSQSRPESPAKQDEPFDEKKYPP**QTPLTREALTLHTKR**
FEDEYKDTWCRRLKRLSDDVPSSPPAKRTTPIHWTSQQNHYRTMAPAPPPPPGKNYQITYTPL
 DDLTDQKSTNTKSDVENVAYPISGSKFSTPMRLSIDGLLPRGATSTGGASPTSGTNSPPVFPKTS
 SSSLLMLRDSQN

>LIN-42 isoform b protein sequence with whole SYQ-LT region deletion highlighted



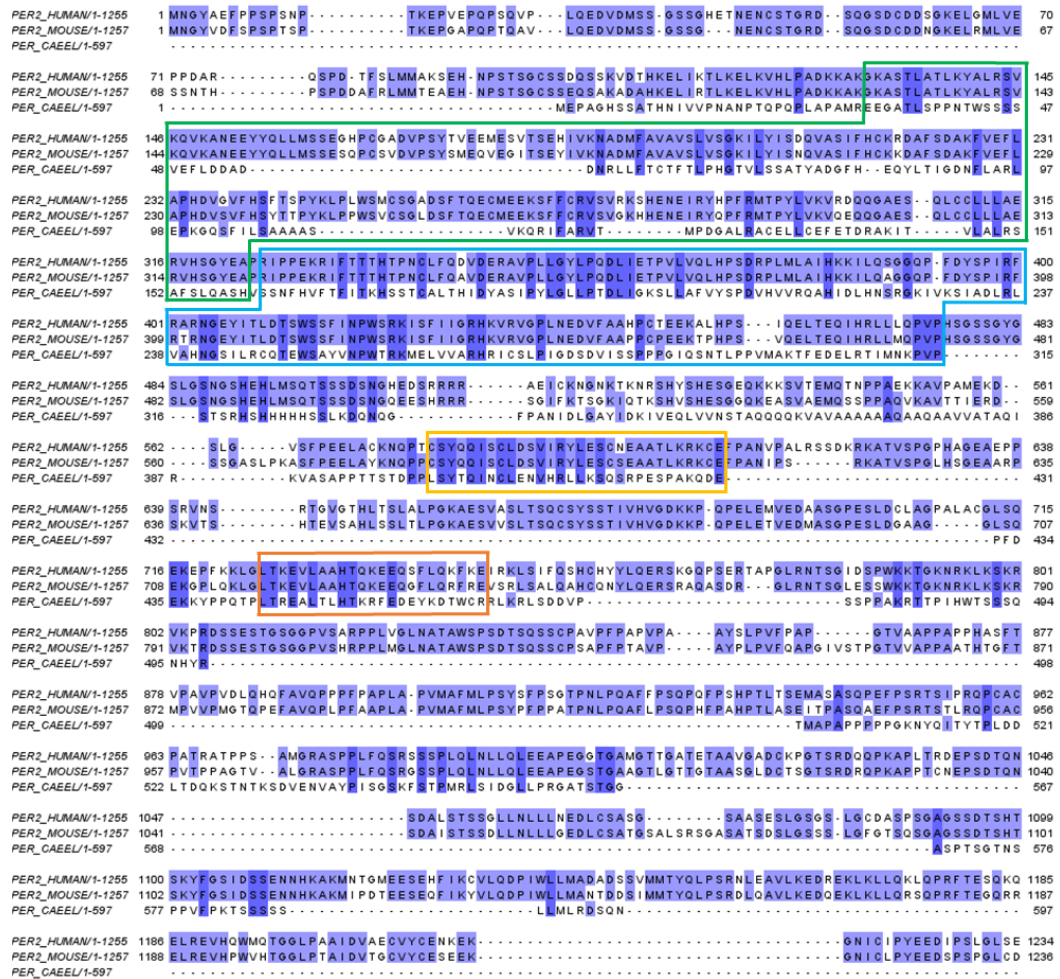
MEPAGHSSATHNIVPNANPTQPQLAPAMREEGATLSPNTWSSSSVEFLDDADDNRLFTCT
 FTLPHGTVLSSATYADGFHEQYL TIGDNFLARLEPKGQSFILSAAAASVKQRIFARVTPDGALR
 ACELLCEFETDRAKITVLALRSFSLQASHVSSNFHVFTFITKHSSTCALHIDYASIPYLGLLPTD
 LIGKSLAFVYSPDVHVVRQAHDHNSRGKIVKSIADLRLVAHNGSILRCQTEWSAYVNPWTRK
 MELVVARHRICSLPIGDSDVSSPPPGIQSNTLPPVMAKTFEDELRTIMNKPVPSTSRHSHHHHH
 SSLKDQNGGFANIDL GAYIDKIVEQLVNVNSTAQQQKQVAVAAAAAAQAAQAAVVATAQIRKVA
 SAPPTTS**DPPLSYTQINCL**ENVHRLLSQSRPESPAKQDEPFDEKKYPP**QTPLTREALTLHTKR**
FEDEYKDTWCRRLKRLSDDVPSSPPAKRTTPIHWTSQQNHYRTMAPAPPPPPGKNYQITYTPL
 DDLTDQKSTNTKSDVENVAYPISGSKFSTPMRLSIDGLLPRGATSTGGASPTSGTNSPPVFPKTS
 SSSLLMLRDSQN

>LIN-42 isoform b protein sequence Whole C-term deletion highlighted (398-591)



MEPAGHSSATHNIVPNANPTQPQLAPAMREEGATLSPNTWSSSSVEFLDDADDNRLFTCT
 FTLPHGTVLSSATYADGFHEQYL TIGDNFLARLEPKGQSFILSAAAASVKQRIFARVTPDGALR
 ACELLCEFETDRAKITVLALRSFSLQASHVSSNFHVFTFITKHSSTCALHIDYASIPYLGLLPTD
 LIGKSLAFVYSPDVHVVRQAHDHNSRGKIVKSIADLRLVAHNGSILRCQTEWSAYVNPWTRK
 MELVVARHRICSLPIGDSDVSSPPPGIQSNTLPPVMAKTFEDELRTIMNKPVPSTSRHSHHHHH
 SSLKDQNGGFANIDL GAYIDKIVEQLVNVNSTAQQQKQVAVAAAAAAQAAQAAVVATAQIRKVA
 SAPPTTS**DPPLSYTQINCL**ENVHRLLSQSRPESPAKQDEPFDEKKYPP**QTPLTREALTLHTKR**
FEDEYKDTWCRRLKRLSDDVPSSPPAKRTTPIHWTSQQNHYRTMAPAPPPPPGKNYQITYTPL
DDLTDQKSTNTKSDVENVAYPISGSKFSTPMRLSIDGLLPRGATSTGGASPTSGTNSPPVFPKTS
SSSLLMLRDSQN

Supplemental Figure 2



Supplemental Figure 2. Sequence alignment of *C. elegans* LIN-42, mouse PER2 and human PER2. PASA domain is boxed in green. PASB domain is boxed in Blue. SYQ domain is boxed in yellow, and LT domain is boxed in orange. Homologous sequence is highlighted in blue.

Materials and methods:

Strains and Nematode Maintenance

C. elegans were grown and maintained at 20°C and cultures as described (BRENNER 1974), except worms were grown on MYOB agar instead of NGM as described (Church, 1995). Full genotypes of strains used in this work are listed in Table 1. All mutant strains were backcrossed to N2 at least 2X. The Bristol N2 strain was used as wild type.

lin-42::GFP::AID::3XFLAG { *lin-42(wrd35[lin-42::GFP^{degron}:3XFLAG])* } parent strain used to observe *lin-42::GFP* expression was generated through self-excising cassette (SEC) selection-based editing as previously described (Dickinson et al. 2015). A single copy transgene was inserted into the 3' end of the endogenous *lin-42* locus. Repair template was injected into EG9615 at 40ng/μl along with 40 ng/μl sgRNA plasmid (pJW1858) + co-injection marker (pCFJ90).

lin-42 mutant strains used in this work were generated by injection of Cas9 or Cas12 ribonucleoprotein complexes as described (Ragle et al. 2022). Specified deletions were made in the endogenous *lin-42* locus, in N2, *lin-42::GFP::AID::3XFLAG*, or both. Repair templates were used at 100ng/μl along with Cas9 or Cas12 at 250ng/μl, crRNA oligos at 60ng/μl, and 10ng/μl co-injection marker (pCFJ90).

In Table 1, we detail the genetic background in which injections were performed and the reagents used to generate each strain.

Strains used in luciferase assays were crosses of mutant strains listed above and a luciferase reporter strain previously described (Milou et al. 2020) HW1993: EG8081; *xeSi312[eft-3p::luc::gfp::unc-54 3'UTR, unc-119(+)]* IV. Crosses and genotypes are detailed in Table 1.

Phenotypic analysis

For all phenotypic analyses, gravid adults were bleached, and embryos were immediately released or singled onto plates seeded with OP50, or gravid adults were picked onto seeded plates and removed after 1-2 hours. Animals were maintained at 20°C and observed daily. Bag-of-worms phenotype was determined when live progeny were observed moving inside adult animals. For brood counts, animals were individually transferred to fresh wells daily for five days after L4 and progeny were counted and averaged. Developmental delay was determined if animals failed to reach adulthood by day 3 after hatching or as determined by length of development in luciferase assays. Statistical significance was determined using a two-tailed unpaired Student's t-test. $P < 0.05$ was considered statistically significant. **** indicates $P < 0.0001$.

Imaging

Synchronized animals were collected from MYOB plates by washing off plates. 1000 μ l of M9 + 2% gelatin was added to the plate or well, agitated to suspend animals in M9+gelatin, and then transferred to a 1.5 ml tube. Animals were spun at 700xg for 1 min. The media was then aspirated off and animals were resuspended in 500 μ l M9 + 2% gelatin with 5 mM levamisole. 12 μ l of animals in M9 +gel with levamisole solution were placed on slides with a 2% agarose pad and secured with a coverslip. Images were acquired using a Plan-Apochromat 40x/1.3 Oil DIC lens or a Plan-Apochromat 63x/1.4 Oil DIC lens on an

Axiomager M2 microscope (Carl Zeiss Microscopy, LLC) equipped with a Colibri 7 LED light source and an Axiocam 506 mono camera. Acquired images were processed through Affinity photo software (version: 1.9.2.1035). For direct comparisons of LIN-42::GFP, we set exposure to we set the exposure conditions to avoid pixel saturation of the brightest sample and kept equivalent exposure for imaging of the other samples.

Luciferase assays

Assays were performed and analyzed as described (Milou et al. 2020). Briefly, Gravid adults were bleached, and eggs were immediately singled into wells containing 90 μ l OP50/S-Basal/D-Luciferin solution per well and left in Luminometer machine and measured every 10 minutes for 0.05 seconds. In this work, the following differences are notes. The assays were performed for 84 hrs and for statistical analysis, we performed a Wilcoxon-Mann-Whitney test (implemented in the python package SciPy version 1.4.1 as the function `mannwhitneyu`).

Expression and purification of recombinant proteins

All proteins were expressed from a pET22-based vector in *Escherichia coli* Rosetta (DE3) cells based on the Parallel vector series (Sheffield et al., 1999). All LIN-42 constructs (Long C, residues 402-598; short C, residues 402-475, all Δ SYQ, Δ LT, and Δ Both mutants) and human FASP peptide were expressed downstream of an N-terminal TEV-cleavable His-NusA tag. Human CK1 δ catalytic domains (CK1 δ Δ C, residues 1–317) were all expressed with a TEV-cleavable His-GST tag. All proteins expressed from Parallel vectors have an additional N-

terminal vector artifact of 'GAMDPEF' remaining after TEV cleavage. Cells were grown in LB media at 37°C until the O.D.600 reached ~0.8; expression was induced with 0.5 mM IPTG, and cultures were grown for approximately 16–20 hr more at 18°C. Cells were centrifuged at 3,200 x g, resuspended in 50 mM Tris, pH 7.5, 300 mM NaCl, 20 mM imidazole, 5% (vol/vol) glycerol, 1 mM tris(2-carboxyethyl)phosphine (TCEP), and 0.05% Tween-20. For purification of recombinant protein, cells were lysed with a microfluidizer followed by sonication and then the lysate was clarified via centrifugation at 140,500 x g for 1 hour at 4°C. Ni-NTA affinity chromatography was used to extract his-tagged proteins from the lysate and then the affinity/solubility tags were cleaved using His6-TEV protease overnight at 4°C. The cleaved protein was then separated from tag and TEV by a second Ni-NTA affinity column and further purified using size exclusion chromatography (SEC) in 50 mM Tris, pH 7.5, 200 mM NaCl, 1 mM EDTA, 5% (vol/vol) glycerol, 1 mM TCEP, and 0.05% Tween-20. Small aliquots of protein were frozen in liquid nitrogen and stored at -70°C for long-term storage.

***In vitro* biotinylation and pull-down assays**

LIN-42 Long C constructs were biotinylated via Sortase A-mediated reactions between a Sortase A recognition motif peptide (biotin-LPETGG) and our LIN-42 long C (N-terminal G from 'GAMDPEF' artifact). Reactions were carried out in 50 mM Tris pH 7.5 and 150 mM NaCl using 5 μM His6-Sortase A, 300 μM biotin-LPETGG, and 50 μM LIN-42 protein. Ni-NTA affinity chromatography followed by SEC was used to purify labeled protein from His6-Sortase A and excess biotin, respectively. Magnetic Streptavidin beads were used to bind biotinylated LIN-42 long C WT and mutants (final concentration 5μM) in the presence and absence of CK1δ ΔC (final concentration 5μM).

32P-ATP kinase assay

1 μ M CK1 δ Δ C was incubated with 10 μ M LIN-42 (Long C or short C WT/mutants) or 10 μ M human FASP peptide in 25 mM Tris pH 7.5, 100 mM NaCl, 10 mM MgCl₂, 2 mM TCEP.

Reactions were started by the addition of ³²P-ATP (final concentration 2 mM) and samples were collected at indicated timepoints and quenched in an equivalent volume of 2x SDS-PAGE loading buffer. Protein labeled with ³²P were separated on an a KDTM pre-cast gel (BioRad) and gels were dried for overnight exposure to phosphoscreen. A Typhoon phosphoimager was used to visualize exposed gels and ³²P-labeled proteins were quantified via densitometry using ImageJ.

ADP-Glo kinase assay

Substrate titrations kinase reactions were performed as done previously (Philpott et al., 2020) using the Promega ADP-Glo kinase assay kit. Reactions were incubated in 25 mM Tris pH 7.5, 100 mM NaCl, 10 mM MgCl₂, 20 mM TCEP, and 100 μ M ATP for 1 hour at room temperature.

Table 1. List of strains used in this work

Table 1 Strains used in this work

Strain name	lin-42 mutations	Genotype	Background	crRNA oligo(s)	repair template	Injected into	outcross	Origin
JDW136	None	<i>lin-42(wrd35[lin-42::GFP^Δdegron:3xFLAG])</i>	wt			EG6915	X3	This work
JDW251	SYQ Δ403-411	<i>lin-42(wrd49[SYQ Δ403-411]::GFP::AID::3xFLAG) II</i>	JDW136	#69_GTCAGTGCTTCTCGGGTCAG TGG	5042	JDW136	X3	This work
JDW248	LT Δ444-446	<i>lin-42(wrd47[LT Δ444-446]::GFP::AID::3xFLAG) II</i>	JDW136	#16_TTTG AAGACGAGTACAAGGACACTTGG	5190	JDW136	X3	This work
JDW270	SYQ Δ403-411; LT Δ444-446	<i>lin-42(wrd50[SYQ Δ403-411]::[LT Δ444-446]::GFP::AID*::3xFLAG) II</i>	JDW136	#69_GTCAGTGCTTCTCGGGTCAG TGG	5042	JDW248	X3	This work
JDW335	CKBD Δ398-462	<i>lin-42 (wrd63[Δ398-462]) II</i>	wt	#143_GAGTGGTGGGTCCTGAGG TGG #145_AAGACGAGTACAAGGACACT TGG	6158	N2	X3	This work
JDW336	CKBD Δ398-462	<i>lin-42 (wrd64[Δ398-462]::GFP::AID*::3xFLAG) II</i>	JDW136	#143_GAGTGGTGGGTCCTGAGG TGG #145_AAGACGAGTACAAGGACACT TGG	6158	JDW136	X2	This work
DW130	C-term Δ398-592	<i>lin-42(wrd89[Δ398-592]) II</i>	wt	#143_GAGTGGTGGGTCCTGAGG TGG #144_CCTCCTCTCTCAATGCTA CGG	6157	N2	X2	This work

Strains used in luciferase assays

Strain name	Deletion	Genotype	HW1993 crossed to	Origin
HW1993	'wild type' control	<i>EG8081, xeSi312 [Peft-3::luc::gfp::unc-54 3' UTR, unc-119(+)] IV</i>		Milou et al. 2020
JDW408	<i>lin-42::GFP control</i>	<i>lin-42(wrd35[lin-42::GFP^Δdegron:3xFLAG])</i>	JDW136	This work
JDW416	SYQ Δ403-411	<i>lin-42(wrd49[SYQ Δ403-411]::GFP::AID::3xFLAG); EG8081, xeSi312 [Peft-3::luc::gfp::unc-54 3' UTR, unc-119(+)] IV</i>	JDW251	This work
JDW415	LT Δ444-446	<i>lin-42(wrd47[LT Δ444-446]::GFP::AID::3xFLAG); EG8081, xeSi312 [Peft-3::luc::gfp::unc-54 3' UTR, unc-119(+)] IV</i>	JDW248	This work
JDW414	SYQ Δ403-411; LT Δ444-446	<i>lin-42(wrd50[SYQ Δ403-411]::[LT Δ444-446]::GFP::AID*::3xFLAG); EG8081, xeSi312 [Peft-3::luc::gfp::unc-54 3' UTR, unc-119(+)] IV</i>	JDW270	This work
JDW417	CKBD Δ398-462	<i>lin-42 (wrd63[Δ398-462]); EG8081, xeSi312 [Peft-3::luc::gfp::unc-54 3' UTR, unc-119(+)] IV</i>	JDW335	This work
JDW437	C-term Δ398-592	<i>lin-42(wrd89[Δ398-592]); EG8081, xeSi312 [Peft-3::luc::gfp::unc-54 3' UTR, unc-119(+)] IV</i>	JDW130	This work

Acknowledgments:

I would like to thank Kathrin Braun from the Großhans Lab at Friedrich Miescher Institute for Biomedical Research for being so kind to run the luciferase assays and perform the necessary analyses. Credit to the Partch lab for Fig 1.6A. Figure was reproduced with their permission. I would also like to thank Matt Ragle for his injections skills, which greatly increased the speed at which I can generate mutant strains.

Bibliography:

- Albrecht, Urs. 2012. "Timing to Perfection: The Biology of Central and Peripheral Circadian Clocks." *Neuron* 74 (2): 246–60.
- Ambros, V. 1989. "A Hierarchy of Regulatory Genes Controls a Larva-to-Adult Developmental Switch in *C. elegans*." *Cell* 57 (1): 49–57.
- Ambros, V., and H. R. Horvitz. 1984. "Heterochronic Mutants of the Nematode *Caenorhabditis elegans*." *Science* 226 (4673): 409–16.
- Ambros, Victor. 2011. "MicroRNAs and Developmental Timing." *Current Opinion in Genetics & Development*. <https://doi.org/10.1016/j.gde.2011.04.003>.
- Ambros, V. 2021. "Development: Keeping Time with Transcription." *Current Biology: CB*.
- Aryal, Rajindra P., Pieter Bas Kwak, Alfred G. Tamayo, Michael Gebert, Po-Lin Chiu, Thomas Walz, and Charles J. Weitz. 2017. "Macromolecular Assemblies of the Mammalian Circadian Clock." *Molecular Cell* 67 (5): 770–82.e6.
- Banerjee, Diya, Alvin Kwok, Shin-Yi Lin, and Frank J. Slack. 2005. "Developmental Timing in *C. elegans* Is Regulated by Kin-20 and TIM-1, Homologs of Core Circadian Clock Genes." *Developmental Cell* 8 (2): 287–95.
- Beesley, Stephen, Dae Wook Kim, Matthew D'Alessandro, Yuanhu Jin, Kwangjun Lee, Hyunjeong Joo, Yang Young, et al. 2020. "Wake-Sleep Cycles Are Severely Disrupted by Diseases Affecting Cytoplasmic Homeostasis." *Proceedings of the National Academy of Sciences of the United States of America* 117 (45): 28402–11.

- Bell-Pedersen, Deborah, Vincent M. Cassone, David J. Earnest, Susan S. Golden, Paul E. Hardin, Terry L. Thomas, and Mark J. Zoran. 2005. "Circadian Rhythms from Multiple Oscillators: Lessons from Diverse Organisms." *Nature Reviews. Genetics* 6 (7): 544–56.
- Brenner, S. 1974. "The Genetics of *Caenorhabditis elegans*." *Genetics* 77 (1): 71–94.
- Chen, Rongmin, Aaron Schirmer, Yongjin Lee, Hyeongmin Lee, Vivek Kumar, Seung-Hee Yoo, Joseph S. Takahashi, and Choogon Lee. 2009. "Rhythmic PER Abundance Defines a Critical Nodal Point for Negative Feedback within the Circadian Clock Mechanism." *Molecular Cell* 36 (3): 417–30.
- Church, D. L., K. L. Guan, and E. J. Lambie. 1995. "Three Genes of the MAP Kinase Cascade, *mek-2*, *mpk-1/sur-1* and *let-60* Ras, Are Required for Meiotic Cell Cycle Progression in *Caenorhabditis elegans*." *Development* 121 (8): 2525–35.
- Concordet, Jean-Paul, and Maximilian Haeussler. 2018. "CRISPOR: Intuitive Guide Selection for CRISPR/Cas9 Genome Editing Experiments and Screens." *Nucleic Acids Research* 46 (W1): W242–45.
- Crosby, Priya, and Carrie L. Partch. 2020. "New Insights into Non-Transcriptional Regulation of Mammalian Core Clock Proteins." *Journal of Cell Science* 133 (18).
<https://doi.org/10.1242/jcs.241174>.
- De Temmerman, Marie-Luce, Jo Demeester, Filip De Vos, and Stefaan C. De Smedt. 2011. "Encapsulation Performance of Layer-by-Layer Microcapsules for Proteins." *Biomacromolecules* 12 (4): 1283–89.
- Dibner, Charna, Ueli Schibler, and Urs Albrecht. 2010. "The Mammalian Circadian Timing System: Organization and Coordination of Central and Peripheral Clocks." *Annual Review of Physiology* 72: 517–49.
- Doherty, Colleen J., and Steve A. Kay. 2010. "Circadian Control of Global Gene Expression Patterns." *Annual Review of Genetics* 44: 419–44.
- Dunlap, J. C. 1999. "Molecular Bases for Circadian Clocks." *Cell* 96 (2): 271–90.
- Edelman, Theresa L. B., Katherine A. McCulloch, Angela Barr, Christian Frøkjær-Jensen, Erik M. Jorgensen, and Ann E. Rougvie. 2016. "Analysis of a *lin-42/period* Null Allele Implicates All Three Isoforms in Regulation of *Caenorhabditis elegans* Molting and Developmental Timing." *G3* 6 (612): 4077–86.
- Edgar, Rachel S., Edward W. Green, Yuwei Zhao, Gerben van Ooijen, Maria Olmedo, Ximing Qin, Yao Xu, et al. 2012. "Peroxioredoxins Are Conserved Markers of Circadian Rhythms." *Nature* 485 (7399): 459–64.

- Eide, Erik J., Margaret F. Woolf, Heeseog Kang, Peter Woolf, William Hurst, Fernando Camacho, Erica L. Vielhaber, Andrew Giovanni, and David M. Virshup. 2005. "Control of Mammalian Circadian Rhythm by CKIepsilon-Regulated Proteasome-Mediated PER2 Degradation." *Molecular and Cellular Biology* 25 (7): 2795–2807.
- Farboud, Behnom, and Barbara J. Meyer. 2015. "Dramatic Enhancement of Genome Editing by CRISPR/Cas9 through Improved Guide RNA Design." *Genetics* 199 (4): 959–71.
- Farboud, Behnom, Aaron F. Severson, and Barbara J. Meyer. 2019. "Strategies for Efficient Genome Editing Using CRISPR-Cas9." *Genetics* 211 (2): 431–57.
- Gallego, Monica, and David M. Virshup. 2007. "Post-Translational Modifications Regulate the Ticking of the Circadian Clock." *Nature Reviews. Molecular Cell Biology* 8 (2): 139–48.
- Gekakis, N., D. Staknis, H. B. Nguyen, F. C. Davis, L. D. Wilsbacher, D. P. King, J. S. Takahashi, and C. J. Weitz. 1998. "Role of the CLOCK Protein in the Mammalian Circadian Mechanism." *Science* 280 (5369): 1564–69.
- Halberg, F., M. Engeli, C. Hamburger, and D. Hillman. 1965. "Spectral Resolution of Low-Frequency, Small-Amplitude Rhythms in Excreted 17-Ketosteroids; Probable Androgen-Induced Circaseptan Desynchronization." *Acta Endocrinologica* 50: Suppl 103:1–54.
- Hasegawa, Kenji, Tetsu Saigusa, and Yoichi Tamai. 2005. "*Caenorhabditis elegans* Opens up New Insights into Circadian Clock Mechanisms." *Chronobiology International* 22 (1): 1–19.
- Hennig, Sven, Holger M. Strauss, Katja Vanselow, Özkan Yildiz, Sabrina Schulze, Julia Arens, Achim Kramer, and Eva Wolf. 2009. "Structural and Functional Analyses of PAS Domain Interactions of the Clock Proteins *Drosophila* PERIOD and Mouse PERIOD2." *PLoS Biology*. <https://doi.org/10.1371/journal.pbio.1000094>.
- Hirano, Arisa, Ying-Hui Fu, and Louis J. Ptáček. 2016. "The Intricate Dance of Post-Translational Modifications in the Rhythm of Life." *Nature Structural & Molecular Biology* 23 (12): 1053–60.
- Hirano, Arisa, Guangsen Shi, Christopher R. Jones, Anna Lipzen, Len A. Pennacchio, Ying Xu, William C. Hallows, et al. 2016. "A Cryptochrome 2 Mutation Yields Advanced Sleep Phase in Humans." *eLife* 5 (August). <https://doi.org/10.7554/eLife.16695>.
- Huang, George, Bailey de Jesus, Alex Koh, Sara Blanco, Aubrie Rettmann, Ella DeMott, Melynda Sylvester, et al. 2021. "Improved CRISPR/Cas9 Knock-in Efficiency via the Self-Excising Cassette (SEC) Selection Method in *C. elegans*." *microPublication Biology* 2021 (September). <https://doi.org/10.17912/micropub.biology.000460>.

Isojima, Yasushi, Masato Nakajima, Hideki Ukai, Hiroshi Fujishima, Rikuhiko G. Yamada, Koh-Hei Masumoto, Reiko Kiuchi, et al. 2009. "CKI ϵ / δ -Dependent Phosphorylation Is a Temperature-Insensitive, Period-Determining Process in the Mammalian Circadian Clock." *Proceedings of the National Academy of Sciences* 106 (37): 15744–49. Ikeda, Ryosuke, Yoshiki Tsuchiya, Nobuya Koike, Yasuhiro Umemura, Hitoshi Inokawa,

Ryutaro Ono, Maho Inoue, et al. 2019. "REV-ERB α and REV-ERB β Function as Key Factors Regulating Mammalian Circadian Output." *Scientific Reports* 9 (1): 10171.

Iwanir, Shachar, Nora Tramm, Stanislav Nagy, Charles Wright, Daniel Ish, and David Biron. 2013. "The Microarchitecture of *C. elegans* Behavior during Lethargus: Homeostatic Bout Dynamics, a Typical Body Posture, and Regulation by a Central Neuron." *Sleep* 36 (3): 385–95.

Jeon, M., H. F. Gardner, E. A. Miller, J. Deshler, and A. E. Rougvie. 1999. "Similarity of the *C. elegans* Developmental Timing Protein LIN-42 to Circadian Rhythm Proteins." *Science* 286 (5442): 1141–46.

Kimble, J., and D. Hirsh. 1979. "The Postembryonic Cell Lineages of the Hermaphrodite and Male Gonads in *Caenorhabditis elegans*." *Developmental Biology* 70 (2): 396–417.

Kume, K., M. J. Zylka, S. Sriram, L. P. Shearman, D. R. Weaver, X. Jin, E. S. Maywood, M. H. Hastings, and S. M. Reppert. 1999. "mCRY1 and mCRY2 Are Essential Components of the Negative Limb of the Circadian Clock Feedback Loop." *Cell* 98 (2): 193–205.

LaBella, Matthew L., Edward J. Hujber, Kristin A. Moore, Randi L. Rawson, Sean A. Merrill, Patrick D. Allaire, Michael Ailion, Julie Hollien, Michael J. Bastiani, and Erik M. Jorgensen. 2020. "Casein Kinase 1 δ Stabilizes Mature Axons by Inhibiting Transcription Termination of Ankyrin." *Developmental Cell* 53 (1): 130.

Lažetić, Vladimir, and David S. Fay. 2017. "Molting in *C. elegans*." *Worm* 6 (1): e1330246.

Lee, C., J. P. Etchegaray, F. R. Cagampang, A. S. Loudon, and S. M. Reppert. 2001. "Posttranslational Mechanisms Regulate the Mammalian Circadian Clock." *Cell* 107 (7): 855–67.

Lee, Choogon, David R. Weaver, and Steven M. Reppert. 2004. "Direct Association between Mouse PERIOD and CKI ϵ Is Critical for a Functioning Circadian Clock." *Molecular and Cellular Biology* 24 (2): 584–94.

Lee, R. C., R. L. Feinbaum, and V. Ambros. 1993. "The *C. elegans* Heterochronic Gene *lin-4* Encodes Small RNAs with Antisense Complementarity to *Lin-14*." *Cell* 75 (5): 843–54.

Lee, Yongjin, Rongmin Chen, Hyeong-Min Lee, and Choogon Lee. 2011. "Stoichiometric Relationship among Clock Proteins Determines Robustness of Circadian Rhythms." *The*

Journal of Biological Chemistry 286 (9): 7033–42.

Liu, Andrew C., Hien G. Tran, Eric E. Zhang, Aaron A. Priest, David K. Welsh, and Steve A. Kay. 2008. "Redundant Function of REV-ERB α and β and Non-Essential Role for *bmal1* Cycling in Transcriptional Regulation of Intracellular Circadian Rhythms." *PLoS Genetics* 4 (2): e1000023.

Lowrey, Phillip L., and Joseph S. Takahashi. 2011. "Genetics of Circadian Rhythms in Mammalian Model Organisms." *Advances in Genetics* 74: 175–230.

Mahesh, V. B. 1985. "The Dynamic Interaction between Steroids and Gonadotropins in the Mammalian Ovarian Cycle." *Neuroscience and Biobehavioral Reviews* 9 (2): 245–60.

Masuda, Shusaku, Rajesh Narasimamurthy, Hikari Yoshitane, Jae Kyoung Kim, Yoshitaka Fukada, and David M. Virshup. 2020. "Mutation of a PER2 Phosphodegron Perturbs the Circadian Phosphoswitch." *Proceedings of the National Academy of Sciences of the United States of America* 117 (20): 10888–96.

McCulloch, Katherine A., and Ann E. Rougvié. 2014. "*Caenorhabditis elegans* Period Homolog Lin-42 Regulates the Timing of Heterochronic miRNA Expression." *Proceedings of the National Academy of Sciences of the United States of America* 111 (43): 15450–55.

Meeuse, Milou Wm, Yannick P. Hauser, Lucas J. Morales Moya, Gert-Jan Hendriks, Jan Eglinger, Guy Bogaarts, Charisios Tsiarlis, and Helge Großhans. 2020. "Developmental Function and State Transitions of a Gene Expression Oscillator in *Caenorhabditis elegans*." *Molecular Systems Biology* 16 (10): e9975.

Migliori, María Laura, Sergio H. Simonetta, Andrés Romanowski, and Diego A. Golombek. 2011. "Circadian Rhythms in Metabolic Variables in *Caenorhabditis elegans*." *Physiology & Behavior*. <https://doi.org/10.1016/j.physbeh.2011.01.026>.

Mohawk, Jennifer A., Carla B. Green, and Joseph S. Takahashi. 2012. "Central and Peripheral Circadian Clocks in Mammals." *Annual Review of Neuroscience*. <https://doi.org/10.1146/annurev-neuro-060909-153128>.

Marzoll, Daniela, Fidel E. Serrano, Anton Shostak, Carolin Schunke, Axel C. R. Diernfellner, and Michael Brunner. 2022. "Casein Kinase 1 and Disordered Clock Proteins Form Functionally Equivalent, Phospho-Based Circadian Modules in Fungi and Mammals." *Proceedings of the National Academy of Sciences of the United States of America* 119 (9). <https://doi.org/10.1073/pnas.2118286119>.

Monsalve, Gabriela C., and Alison R. Frand. 2012. "Toward a Unified Model of Developmental Timing." *Worm*. <https://doi.org/10.4161/worm.20874>.

- Monsalve, Gabriela C., Cheryl Van Buskirk, and Alison R. Frand. 2011. "LIN-42/PERIOD Controls Cyclical and Developmental Progression of *C. elegans* Molts." *Current Biology: CB* 21 (24): 2033–45.
- Moss, Eric G. 2007. "Heterochronic Genes and the Nature of Developmental Time." *Current Biology: CB* 17 (11): R425–34.
- Parico, Gian Carlo G., and Carrie L. Partch. 2020. "The Tail of Cryptochromes: An Intrinsically Disordered Cog within the Mammalian Circadian Clock." *Cell Communication and Signaling: CCS* 18 (1): 182.
- Parico, Gian Carlo G., Ivette Perez, Jennifer L. Fribourgh, Britney N. Hernandez, Hsiau-Wei Lee, and Carrie L. Partch. 2020. "The Human CRY1 Tail Controls Circadian Timing by Regulating Its Association with CLOCK:BMAL1." *Proceedings of the National Academy of Sciences*. <https://doi.org/10.1073/pnas.1920653117>.
- Patke, Alina, Patricia J. Murphy, Onur Emre Onat, Ana C. Krieger, Tayfun Özçelik, Scott S. Campbell, and Michael W. Young. 2017. "Mutation of the Human Circadian Clock Gene CRY1 in Familial Delayed Sleep Phase Disorder." *Cell* 169 (2): 203–15.e13.
- Perales, Roberto, Dana M. King, Cristina Aguirre-Chen, and Christopher M. Hammell. 2014. "LIN-42, the *Caenorhabditis elegans* PERIOD Homolog, Negatively Regulates microRNA Transcription." *PLoS Genetics* 10 (7): e1004486.
- Philpott, Jonathan M., Megan R. Torgrimson, Rachel L. Harold, and Carrie L. Partch. 2022. "Biochemical Mechanisms of Period Control within the Mammalian Circadian Clock." *Seminars in Cell & Developmental Biology*. <https://doi.org/10.1016/j.semcd.2021.04.012>.
- Preußner, Marco, and Florian Heyd. 2016. "Post-Transcriptional Control of the Mammalian Circadian Clock: Implications for Health and Disease." *Pflugers Archiv: European Journal of Physiology* 468 (6): 983–91.
- Ragle, James Matthew, Kayleigh N. Morrison, An A. Vo, Zoe E. Johnson, Javier Hernandez Lopez, Andreas Rechtsteiner, Diane C. Shakes, and Jordan D. Ward. 2022. "NHR-23 and SPE-44 Regulate Distinct Sets of Genes during *C. elegans* Spermatogenesis." *bioRxiv*. <https://doi.org/10.1101/2022.06.24.497528>.
- Rhodehouse, Kyle, Katherine Cascino, Laura Aseltine, Allegra Padula, Rachel Weinstein, Joseph S. Spina, Christiane E. Olivero, and Priscilla M. Van Wynsberghe. 2018. "The Doubletime Homolog KIN-20 Mainly Regulates *let-7* Independently of Its Effects on the Period Homolog LIN-42 in *Caenorhabditis elegans*." *G3* 8 (8): 2617–29.
- Rougvie, Ann E., and Eric G. Moss. 2013. "Developmental Transitions in *C. elegans* Larval Stages." *Current Topics in Developmental Biology* 105: 153–80.

Ruaud, A-F. 2006. "Activation of Nicotinic Receptors Uncouples a Developmental Timer from the Molting Timer in *C. elegans*." *Development* 133 (11): 2211–22.

Schulz, Hartmut, and Peretz Lavie. 1985. *Ultradian Rhythms in Physiology and Behavior*. Springer Verlag Berlin, Germany.

Shearman, Lauren P., Mark J. Zylka, David R. Weaver, Lee F. Kolakowski, and Steven M. Reppert. 1997. "Two Period Homologs: Circadian Expression and Photic Regulation in the Suprachiasmatic Nuclei." *Neuron*. [https://doi.org/10.1016/s0896-6273\(00\)80417-1](https://doi.org/10.1016/s0896-6273(00)80417-1).

Shinohara, Yuta, Yohei M. Koyama, Maki Ukai-Tadenuma, Takatsugu Hirokawa, Masaki Kikuchi, Rikuhiko G. Yamada, Hideki Ukai, et al. 2017. "Temperature-Sensitive Substrate and Product Binding Underlie Temperature-Compensated Phosphorylation in the Clock." *Molecular Cell* 67 (5): 783–98.e20.

Simonetta, Sergio H., María Laura Migliori, Andrés Romanowski, and Diego A. Golombek. 2009. "Timing of Locomotor Activity Circadian Rhythms in *Caenorhabditis elegans*." *PloS One* 4 (10): e7571.

Singh, R. N., and J. E. Sulston. 1978. "Some Observations On Moulting in *Caenorhabditis elegans*." *Nematologica* 24 (1): 63–71.

Steinlechner, Stephan, Birgit Jacobmeier, Frank Scherbarth, Haiko Dernbach, Friederike Kruse, and Urs Albrecht. 2002. "Robust Circadian Rhythmicity of *per1* and *per2* Mutant Mice in Constant Light, and Dynamics of *per1* and *per2* Gene Expression under Long and Short Photoperiods." *Journal of Biological Rhythms* 17 (3): 202–9.

Sulston, J. E., and H. R. Horvitz. 1977. "Post-Embryonic Cell Lineages of the Nematode, *Caenorhabditis elegans*." *Developmental Biology* 56 (1): 110–56.

Sulston, J. E., E. Schierenberg, J. G. White, and J. N. Thomson. 1983. "The Embryonic Cell Lineage of the Nematode *Caenorhabditis elegans*." *Developmental Biology* 100 (1): 64–119.

Takahashi, Joseph S. 2017. "Transcriptional Architecture of the Mammalian Circadian Clock." *Nature Reviews. Genetics* 18 (3): 164–79.

Tei, H., H. Okamura, Y. Shigeyoshi, C. Fukuhara, R. Ozawa, M. Hirose, and Y. Sakaki. 1997. "Circadian Oscillation of a Mammalian Homologue of the *Drosophila* Period Gene." *Nature* 389 (6650): 512–16.

Tennessee, Jason M., Heather F. Gardner, Mandy L. Volk, and Ann E. Rougvie. 2006. "Novel Heterochronic Functions of the *Caenorhabditis elegans* Period-Related Protein LIN-42." *Developmental Biology* 289 (1): 30–43.

Toh, K. L., C. R. Jones, Y. He, E. J. Eide, W. A. Hinz, D. M. Virshup, L. J. Ptáček, and Y. H. Fu.

2001. "An hPer2 Phosphorylation Site Mutation in Familial Advanced Sleep Phase Syndrome." *Science* 291 (5506): 1040–43.

Van Wynsberghe, Priscilla M., Emily F. Finnegan, Thomas Stark, Evan P. Angelus, Kathryn E. Homan, Gene W. Yeo, and Amy E. Pasquinelli. 2014. "The Period Protein Homolog LIN-42 Negatively Regulates microRNA Biogenesis in *C. elegans*." *Developmental Biology*. <https://doi.org/10.1016/j.ydbio.2014.03.017>.

Xu, Y., K. L. Toh, C. R. Jones, J-Y Shin, Y-H Fu, and L. J. Ptáček. 2007. "Modeling of a Human Circadian Mutation Yields Insights into Clock Regulation by PER2." *Cell* 128 (1): 59–70.

Young, M. W., and S. A. Kay. 2001. "Time Zones: A Comparative Genetics of Circadian Clocks." *Nature Reviews. Genetics* 2 (9): 702–15.

Zheng, B., D. W. Larkin, U. Albrecht, Z. S. Sun, M. Sage, G. Eichele, C. C. Lee, and A. Bradley. 1999. "The mPer2 Gene Encodes a Functional Component of the Mammalian Circadian Clock." *Nature* 400 (6740): 169–73.

Chapter 2

An expanded auxin-inducible degron toolkit for *Caenorhabditis elegans*

[This chapter has been adapted from publication, **An expanded auxin-inducible degron toolkit for *Caenorhabditis elegans***, (Ashley et al. 2020) Genetics]

Authors: Guinevere Ashley¹, Tam Duong^{*2}, Max T. Levenson^{*1}, Michael A. Q. Martinez^{*3}, Londen C. Johnsen¹, Jonathan D. Hibshman⁴, Hannah N. Saeger¹, Nicholas J. Palmisano³, Ryan Doonan⁵, Raquel Martinez-Mendez¹, Brittany Davidson¹, Wan Zhang³, James Matthew Ragle¹, Taylor N. Medwig-Kinney³, Sydney S. Sirota³, Bob Goldstein^{4,6}, David Q. Matus³, Daniel J. Dickinson⁵, David J. Reiner², and Jordan D. Ward^{1,‡}

¹Department of Molecular, Cell, and Developmental Biology, University of California-Santa Cruz, Santa Cruz, CA 95064, USA.

²Institute of Biosciences and Technology, Texas A&M Health Science Center, Houston, TX 77030, USA.

³Department of Biochemistry and Cell Biology, Stony Brook University, Stony Brook, NY 11794, USA.

⁴Department of Biology, University of North Carolina at Chapel Hill, Chapel Hill, North Carolina, USA

⁵Department of Molecular Biosciences, University of Texas at Austin, Austin, TX 78712, USA.

⁶Lineberger Comprehensive Cancer Center, University of North Carolina at Chapel Hill, Chapel Hill, North Carolina, USA

[‡]Correspondence should be addressed to jward2@ucsc.edu

Permission from the co-authors giving their approval for the material used in this dissertation has been submitted separately to ProQuest.

Abstract

The auxin-inducible degron (AID) system has emerged as a powerful tool to conditionally deplete proteins in a range of organisms and cell types. Here, we describe a toolkit to augment the use of the AID system in *Caenorhabditis elegans*. We have generated a set of single-copy, tissue-specific (germline, intestine, neuron, muscle, pharynx, hypodermis, seam cell, anchor cell) and pan-somatic TIR1-expressing strains carrying a co-expressed blue fluorescent reporter to enable use of both red and green channels in experiments. These transgenes are inserted into commonly used, well-characterized genetic loci. We confirmed that our TIR1-expressing strains produce the expected depletion phenotype for several nuclear and cytoplasmic AID-tagged endogenous substrates. We have also constructed a set of plasmids for constructing repair templates to generate fluorescent protein::AID fusions through CRISPR/Cas9-mediated genome editing. These plasmids are compatible with commonly used genome editing approaches in the *C. elegans* community (Gibson or SapTrap assembly of plasmid repair templates or PCR-derived linear repair templates). Together these reagents will complement existing TIR1 strains and facilitate rapid and high-throughput fluorescent protein::AID tagging of genes. This battery of new TIR1-expressing strains and modular, efficient cloning vectors serves as a platform for straightforward assembly of CRISPR/Cas9 repair templates for conditional protein depletion.

Introduction

The AID system has allowed rapid, conditional, and tissue-specific depletion of tagged proteins in a wide range of organisms and cell types (Nishimura *et al.* 2009; Holland *et al.*

2012; Zhang *et al.* 2015; Natsume *et al.* 2016; Trost *et al.* 2016; Brown *et al.* 2017; Daniel *et al.* 2018; Chen *et al.* 2018; Camlin and Evans 2019). Since its introduction to *C. elegans* (Zhang *et al.* 2015), it has been promptly adopted by the community. This system has allowed for rapid depletion of proteins in tissues that are refractory to RNA interference approaches, such as the germline (Pelisch *et al.* 2017; Shen *et al.* 2018; Zhang *et al.* 2018b), vulval precursor cells (Matus *et al.* 2014), and neurons (Liu *et al.* 2017; Patel and Hobert 2017; Serrano-Saiz *et al.* 2018). The system is also powerful for studying rapid developmental events such as molting (Zhang *et al.* 2015; Joseph *et al.* 2020), organogenesis (Martinez *et al.* 2020), developmental timing (Azzi *et al.* 2020), meiosis (Zhang *et al.* 2015), and spermatogenesis (Ragle *et al.* 2020). Improvements to the auxin ligand have enhanced protein degradation in the embryo (Negishi *et al.* 2019) and removed the need for ethanol solubilization, allowing the auxin derivative to be dissolved in any aqueous buffer (Martinez *et al.* 2020). This water-soluble auxin was shown to be compatible with microfluidic devices, allowing the coupling of long-term imaging and targeted protein depletion (Martinez *et al.* 2020). Auxin-mediated depletion of a spermatogenesis regulator has been developed to conditionally sterilize animals, a valuable approach for the *C. elegans* aging field (Kasimatis *et al.* 2018).

The system is comprised of two components. First, the plant F-box protein Transport Inhibitor Response 1 (TIR1) is expressed under the control of a promoter with a defined expression pattern (Figure 1). TIR1 can then interact with endogenous Skp1 and Cul1 proteins to form a functional SCF E3 ubiquitin ligase complex (Figure 1). Second, an auxin-

inducible degron (AID) sequence from the IAA17 protein is fused to a protein of interest (Figure 1) (Nishimura *et al.* 2009; Natsume and Kanemaki 2017). Addition of the plant hormone, auxin, promotes TIR1 binding to the degron, leading to the ubiquitination and subsequent proteasome-mediated degradation of the degron-tagged protein (Figure 1). While the full length IAA17 sequence is 229 amino acids, minimal AID tags of 44 amino acids (AID*) and 68 amino acids (mAID) have been developed (Morawska and Ulrich 2013; Li *et al.* 2019). In *C. elegans*, the *Arabidopsis thaliana* TIR1, AID*, and mAID sequences are used (Zhang *et al.* 2015; Negishi *et al.* 2019), as this plant grows at a temperature range more similar to *C. elegans*, whereas rice (*Oryza sativa*)-derived sequences are used in other systems (Nishimura *et al.* 2009; Natsume *et al.* 2016; Natsume and Kanemaki 2017). The SCF ligase in *C. elegans* with which TIR1 interacts is thought to be comprised of SKR-1/2, CUL-1, and RBX-1 (Martinez *et al.* 2020).

Here, we describe a new set of strains and reagents for *C. elegans* that complement the tools originally described by Zhang *et al.* (2015). To enable both targeted protein degradation and imaging-based measurement of depletion, we have generated a set of strains that express single-copy, tissue-specific TIR1 marked with a reporter of activity (*TIR1::F2A::mTagBFP2::AID*::NLS*). Nuclear-localized mTagBFP2::AID* (hereafter referred to simply as “BFP”) serves as a reporter for TIR1 expression. TIR1 should degrade BFP in the presence of auxin, providing a built-in read-out of TIR1 activity. For many of the tissue-specific promoters driving this construct, we have created strains with insertions into well-characterized, neutral target sites on both chromosomes I and II (Frøkjær-Jensen *et al.* 2008; Frøkjær-Jensen *et al.* 2012), to facilitate crossing schemes. These strains expand

experimental possibilities with green and red fluorescent proteins (FPs) of interest. We have also generated constructs to introduce FP::AID* tags into genes of interest using conventional genome editing approaches in *C. elegans*.

Ashley et al. (2020) Figure 1

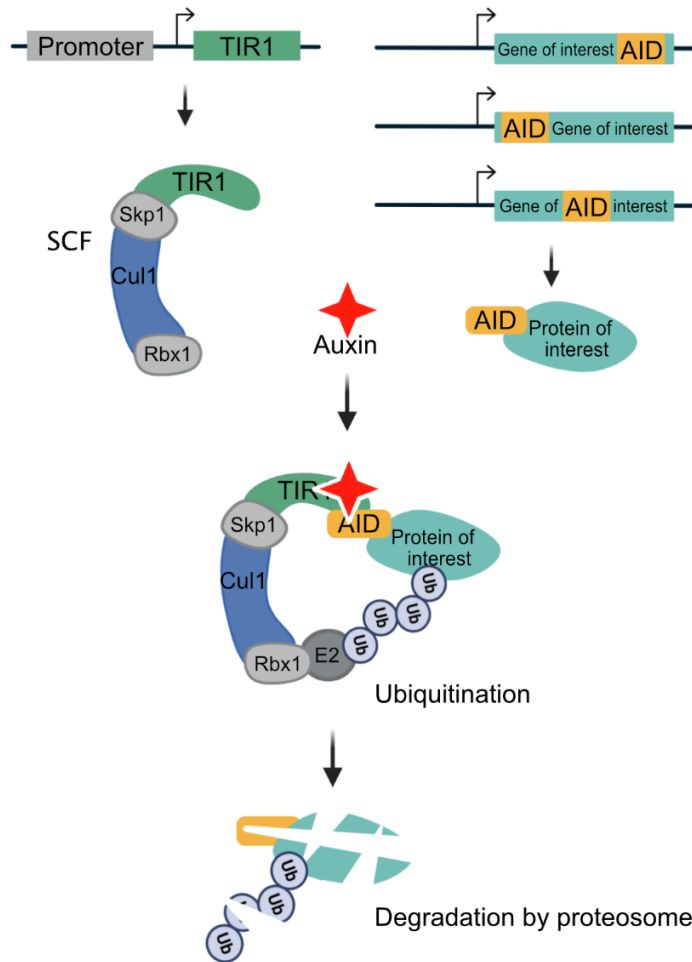


Figure 1. Schematic of the auxin-inducible degron (AID) system. The plant F-box protein TIR1 is expressed using a promoter of interest with a desired spatiotemporal expression pattern. TIR1 interacts with endogenous Skp1 and Cul1 proteins to form an SCF E3 ubiquitin ligase complex. An auxin-inducible degron sequence (AID) is fused to a protein of interest. In the presence of the plant hormone auxin, TIR1 recognizes and binds the AID sequence, leading to ubiquitination and subsequent degradation of the AID-tagged protein. We use a minimal, 44 amino acid degron sequence (AID*), but a full-length 229 amino acid AID tag or a 68 amino acid mini-AID (mAID) are used in other systems. In *C. elegans*, the system is frequently used with single-copy TIR1 transgenes inserted into neutral loci, and AID* knock-ins into genes of interest, though extrachromosomal arrays can also be used.

Results:

A new TIR1 transgene with a built-in BFP::AID*::NLS reporter

The initial description of the AID system in *C. elegans* used an mRuby2 fusion to monitor the expression of TIR1 (Zhang *et al.* 2015). This feature was useful to monitor TIR1 localization and expression level in comparison to depletion of GFP::AID* tagged proteins. One limitation is that the mRuby2 fusion interferes with the imaging of factors tagged with red FPs. Blue fluorescent proteins offer an appealing alternative as reporters for TIR1 expression, since their emission spectra do not significantly overlap with commonly used green and red FPs (Lambert 2019). To report TIR1 expression and activity, we placed an *F2A::BFP::AID*::NLS* reporter downstream of the TIR1 transgene and put the transgene under the control of a *sun-1* promoter, which drives germline and embryo expression (Figure 2A). We used an F2A ribosome skip sequence to allow separate TIR1 and BFP::AID*::NLS proteins to be produced from the mRNA transcript (Ryan and Drew 1994; Ryan *et al.* 1999; Donnelly *et al.* 2001; de Felipe *et al.* 2003; Ahier and Jarriault 2014).

Our *sun-1p::TIR1::F2A::BFP::AID*::NLS* transgene was introduced in single copy through CRISPR/Cas9 editing and self-excising cassette (SEC) selection into the same neutral locus where Mos1 transposon was inserted in ttTi4348 (Dickinson *et al.* 2015). The SEC strategy (Dickinson *et al.* 2015) first produces hygromycin resistant, rolling animals, which is useful for tracking the allele phenotypically in crosses. The loxP-flanked SEC is then excised by heat shock, producing the final strain with wild type locomotion. As expected, this *sun-1p* construct drives nuclear-localized BFP in the germline and embryos, confirming the

expression of the transgene. We confirmed TIR1 activity by placing adult animals on 1 mM auxin and observing loss of BFP::AID*::NLS (Figure 2B). To test the performance of our new TIR1 transgene, we compared depletion of mNeonGreen (mNG)::AID*::PAR-3 using the *sun-1p::TIR1::F2A::BFP::AID*::NLS* transgene and the original *sun-1p::TIR1::mRuby2* transgene (Zhang *et al.* 2015). In the absence of auxin, comparable PAR-3 fluorescence was observed (Figure 2C,D). Similarly, exposure to 1 mM auxin resulted in a comparable loss of fluorescence (Figure 2D). Moreover, 100% of auxin-treated embryos exhibited symmetric cell division which is the expected *par-3* loss-of-function phenotype (Figure 2C). Together, these results indicate that our *TIR1::F2A::BFP::AID*::NLS* transgene can effectively deplete AID*-tagged PAR-3, a cytoplasmic cell polarity determinant.

We planned to insert our constructs into the sites in chromosomes I and II, respectively, where the ttTi4348 and ttTi5605 transposons are inserted for MosSCI-based genome editing (Frøkjær-Jensen *et al.* 2008; Frøkjær-Jensen *et al.* 2012). To facilitate genome editing, we created sgRNA and Cas9+sgRNA vectors targeting these loci containing the “Flipped and extended (F+E)” sgRNA modifications that improved editing efficiency in mammalian cells and *C. elegans* (Chen *et al.* 2013; Ward 2015) (Table 1). We generated sgRNA expression vectors using the two commonly used U6 promoters in *C. elegans* as it is currently unclear whether one promoter is broadly more active (Friedland *et al.* 2013; Dickinson *et al.* 2013; Schwartz and Jorgensen 2016) (Table 1). We also generated sgRNA vectors targeting the cxTi10882 insertion site on chromosome IV to support future knock-ins into this locus (Frøkjær-Jensen *et al.* 2008; Frøkjær-Jensen *et al.* 2012).

Figure 2. A new TIR1 expression system allows assessment of TIR1 expression and activity. A) The new TIR1 expression construct contains a *TIR1::F2A::BFP::AID*::NLS* transgene cassette. An F2A skip sequence results in expression of two separate protein products: 1) TIR1, which will interact with endogenous SCF proteins to produce an E3 ubiquitin ligase complex and can only bind the AID sequence in the presence of auxin; and 2) an AID*-tagged BFP protein with a c-Myc nuclear localization signal (NLS) that functions as a readout for TIR1 expression and internal control for TIR1 activity. The use of BFP as a reporter makes this construct compatible with simultaneous green and red FP imaging. B) Adult animals expressing *sun1p::TIR1::F2A::BFP::AID*::NLS*. A control animal expresses AID*-tagged BFP in the nuclei of germline and embryonic cells (white arrows). When animals are exposed to 1 mM auxin, BFP expression is undetectable. BFP channel and DIC images are provided for each condition. Note that the fluorescence signal at the lower right-hand side of each BFP image is due to intestinal autofluorescence. Scale bars represent 50 μ m. C) Images of embryos harboring endogenously-tagged *mNG::AID*::PAR-3* and expressing either *sun-1p::TIR1::mRuby2* (Zhang et al. 2015) or *sun-1p::TIR1::F2A::BFP::AID*::NLS* (this study). Both TIR1 transgenes were able to deplete *mNG::AID*::PAR-3* to background levels in the presence of auxin and produced a symmetric first division as expected for loss of PAR-3 function. D) Quantification of whole-embryo *mNG::AID*::PAR-3* fluorescence intensity for the indicated conditions. Wild-type (N2) embryos were measured to account for autofluorescent background. Data points represent the fluorescence intensity from individual embryos; at least six embryos were imaged for each condition. The horizontal red bar depicts the mean for each condition.

Ashley et al. (2020) Figure 2

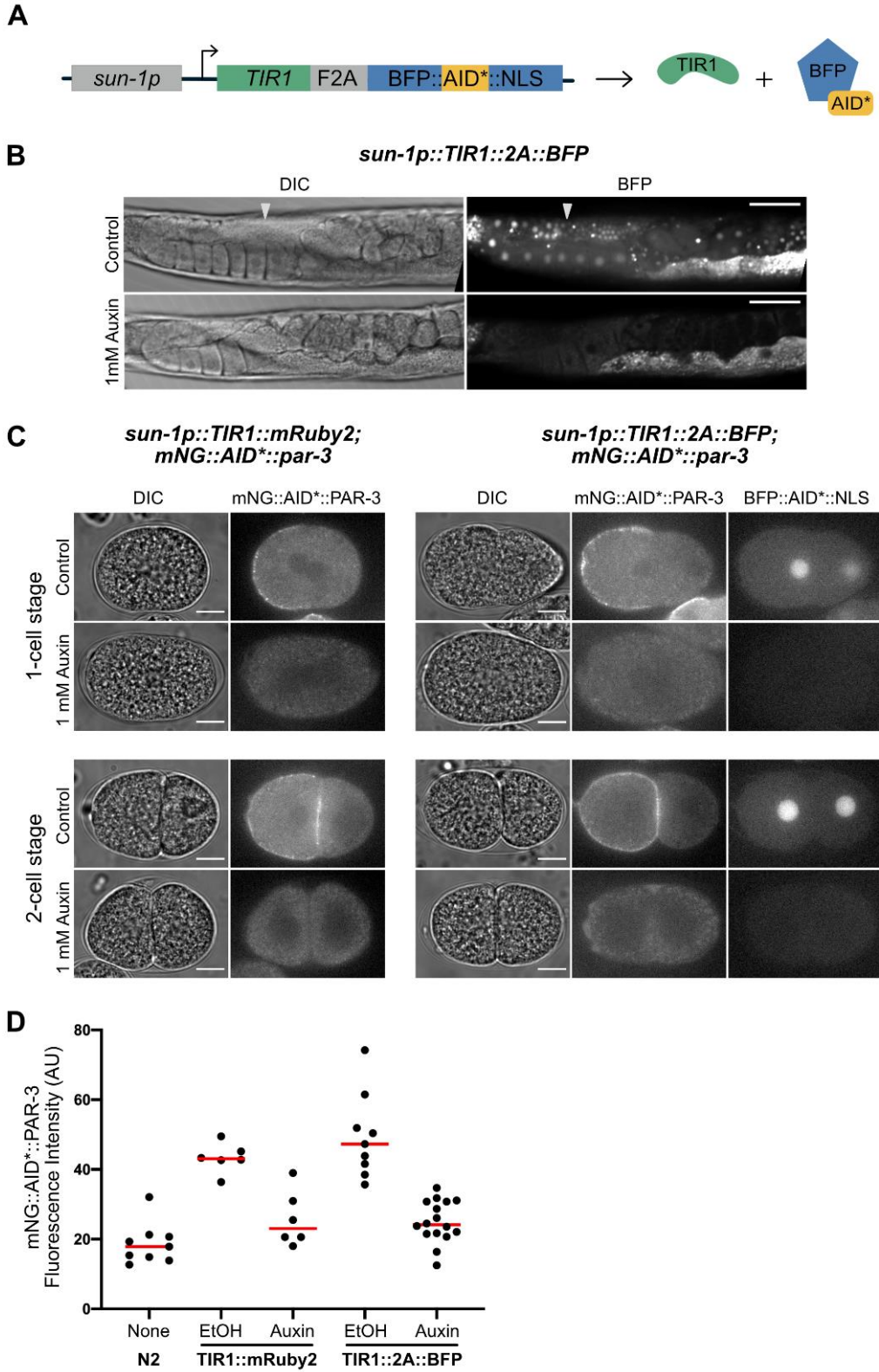


Table 1. Plasmids to support generation of new TIR1 alleles and other transgenes at standardized genetic loci through CRISPR/Cas-based genome editing.

Plasmid name	Description	Purpose
pJW1838	SapTrap sgRNA (F+E) vector, <i>K09B11.2</i> U6 promoter and 3'UTR	Creating new sgRNA (F+E) plasmids
pJW1839	SapTrap sgRNA (F+E) vector, <i>R07E5.16</i> U6 promoter	Creating new sgRNA (F+E) plasmids
pJW1836	promoterless <i>SV40 NLS::mScarlet-I (dpi)::PEST::tbb-2</i> 3'UTR vector	Promoter reporter, test new tissue-specific promoters
pJW1841	promoterless <i>SV40 NLS::mScarlet-I (dpi)::tbb-2</i> 3'UTR vector	Promoter reporter, test new tissue-specific promoters
pJW1849	ttTi4348 site targeting sgRNA (F+E) with <i>K09B11.2</i> U6 promoter and 3'UTR	CRISPR/Cas9 editing of ttTi4348 insertion site
pJW1850	ttTi5605 site targeting sgRNA (F+E) with <i>K09B11.2</i> U6 promoter and 3'UTR	CRISPR/Cas9 editing of ttTi5605 insertion site
pJW1851	cxTi10882 site targeting sgRNA (F+E) with <i>K09B11.2</i> U6 promoter and 3'UTR	CRISPR/Cas9 editing of cxTi10882 insertion site
pJW1882	ttTi4348 site targeting sgRNA (F+E) with <i>R07E5.16</i> U6 promoter and 3'UTR	CRISPR/Cas9 editing of ttTi4348 insertion site
pJW1883	ttTi5605 site targeting sgRNA (F+E) with <i>R07E5.16</i> U6 promoter and 3'UTR	CRISPR/Cas9 editing of ttTi5605 insertion site
pJW1884	cxTi10882 site targeting sgRNA (F+E) with <i>R07E5.16</i> U6 promoter and 3'UTR	CRISPR/Cas9 editing of cxTi10882 insertion site
pJW1947	<i>pes-10Δ minimal promoter::SV40 NLS::mScarlet-I (dpi)::tbb-2</i> 3'UTR vector	Promoter reporter, test new tissue-specific promoters
pJW1948	<i>pes-10Δ minimal promoter::SV40 NLS::mScarlet-I (dpi)::PEST::tbb-2</i> 3'UTR vector	Promoter reporter, test new tissue-specific promoters
pTD77	<i>eft-3p::Cas9, R07E5.16 U6::sgRNA</i> targeting LGI site where ttTi4348 Mos is inserted	CRISPR/Cas9 editing of ttTi4348 insertion site
pTD78	<i>eft-3p::Cas9, R07E5.16 U6::sgRNA</i> targeting LGII site where ttTi5605 Mos is inserted	CRISPR/Cas9 editing of ttTi5605 insertion site

The F2A ribosome skip sequence functions efficiently in an *eft-*

***3p::TIR1::F2A::BFP::AID*::NLS* transgene**

We tested the efficiency of the F2A peptide in our new TIR1 transgenes, as inefficient processing could create a TIR1::F2A::BFP::AID*::NLS fusion protein that could be nuclear localized and degraded, impairing performance of the system. The expression of BFP in our *sun-1p* strain was quite dim and we were unable to detect it via western blot. We therefore generated a new *TIR1::F2A::BFP::AID*::NLS* construct driven by a strong ubiquitous promoter (*eft-3p*) and inserted this transgene in the same site. We observed somatic BFP which was lost upon auxin exposure, indicating that our TIR1 transgene was functional (Figure 3A). We performed anti-BFP western blots on this strain (Figure 3B). We observed a doublet in the *eft-3p::TIR1::F2A::BFP::AID*::NLS* strain which was not present in N2 control animals. The upper band was consistent with the predicted size of the BFP reporter (34.5 kDa). The lower band is most likely a degradation product, as tRFP-derived proteins such as BFP are known to fragment in western blots (Kovacs *et al.* 2012; Breunig *et al.* 2015; Katoch *et al.* 2016). A similar doublet was also reported in the product literature for the antibody we used. We never observed a 101.5 kDa band, which is the predicted size for a TIR1::F2A::BFP::AID*::NLS fusion protein. Together, these data suggest that the F2A peptide is being effectively processed to produce a BFP::AID*::NLS reporter which marks TIR1 expression.

Ashley *et al.* (2020) Figure 3

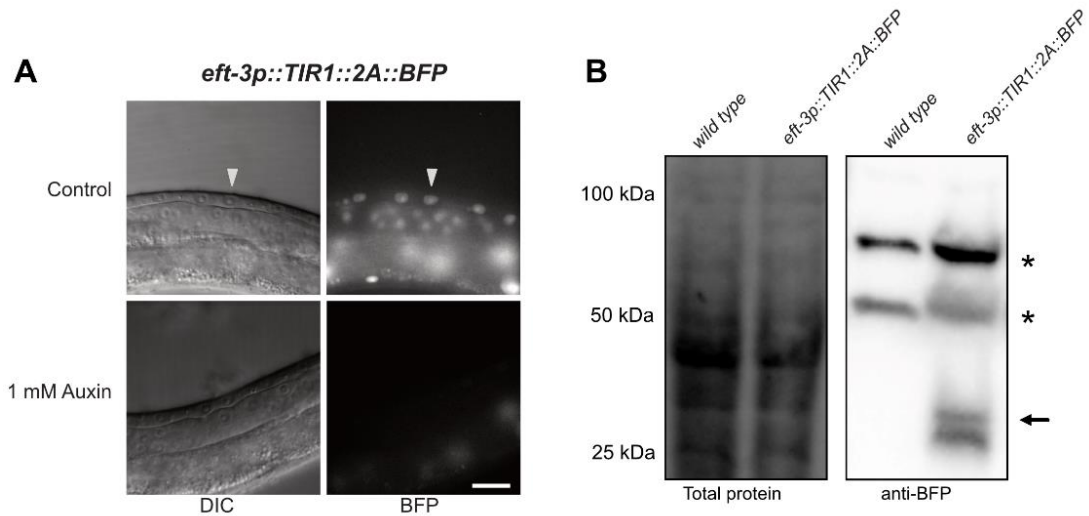


Figure 3. The F2A ribosome skip sequence functions efficiently in an *eft-3p::TIR1::F2A::BFP::AID*::NLS* transgene. A) L3 larvae expressing *eft-3p::TIR1::F2A::BFP::AID*::NLS*. A control animal expresses AID*-tagged BFP in the nuclei of vulval precursor cells (VPCs; white arrows). BFP expression is undetectable in animals grown on 1 mM K-NAA—a water-soluble, synthetic auxin—for 1 hour before imaging. Scale bars represent 15 μm (*eft-3p*). B) Western blot detecting *BFP::AID*::NLS*. Stain-free (Bio-Rad) analysis of total protein on the blot is provided as a loading control (left). Marker size (in kilodaltons) is provided. Anti-BFP blot showing background bands (marked with *) and a doublet consistent with the predicted size of *BFP::AID*::NLS* (black arrow) at approximately 34.5 kDa, and a smaller band below, likely a BFP degradation product.

***eft-3p::TIR1::F2A::BFP::AID*::NLS* is functionally equivalent to *eft-3p::TIR1::mRuby2*, but exhibits slower kinetics for degradation of substrates**

To test the efficiency of our new *eft-3p::TIR1::F2A::BFP::AID*::NLS* transgene, we crossed it to an *eft-3p::AID*::GFP* reporter and compared *AID*::GFP* depletion level and rate between our new TIR1 strain and the original *eft-3p::TIR1::mRuby2* strain (Zhang *et al.* 2015). TIR1::mRuby2 strongly depleted the *AID*::GFP* reporter within 30 minutes of exposure to the natural auxin indole-3-acetic acid (IAA) used by Zhang *et al.* (2015). In contrast, TIR1::F2A::BFP::AID*::NLS took 120 minutes to completely deplete the *AID*::GFP* reporter after exposure to IAA. (Figure 4A). Single-cell imaging of the *AID*::GFP* reporter in vulval precursor cells (VPCs)(Figure 4B, Figure S2) supported the western blot data (Figure 4A). We also compared the performance of IAA to K-NAA, a water-soluble synthetic auxin recently described for use in *C. elegans* (Martinez *et al.* 2020). The reporter was strongly depleted 30 minutes after exposure to both IAA and K-NAA in the TIR1::mRuby2 strain, but took 90 minutes for equivalent depletion in the TIR1::F2A::BFP::AID*::NLS strain (Figure 4C, Figure S2). We also compared the ratio of nuclear to cytoplasmic *AID*::GFP* to test whether there were differences in sub-cellular depletion rates. We did not observe differences in the nuclear/cytoplasmic ratio, suggesting that both TIR1::mRuby2 and TIR1::F2A::BFP::AID*::NLS are equally effective at depleting nuclear and cytoplasmic *AID*::GFP* (Figure S3). IAA and K-NAA performed identically in these experiments (Figure S3).

Ashley et al. (2020) Figure 4

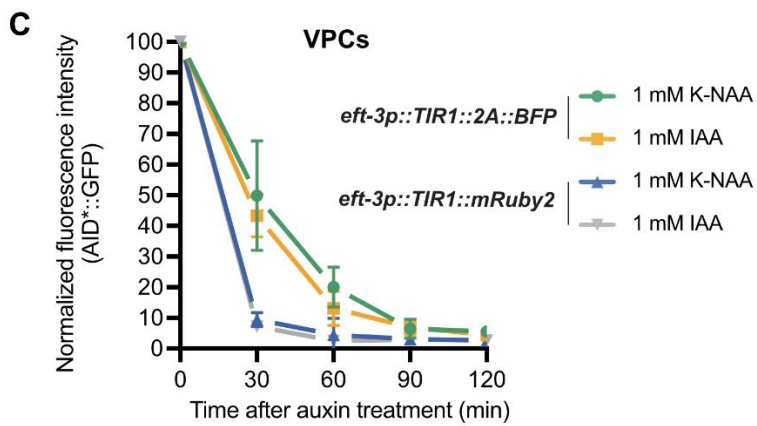
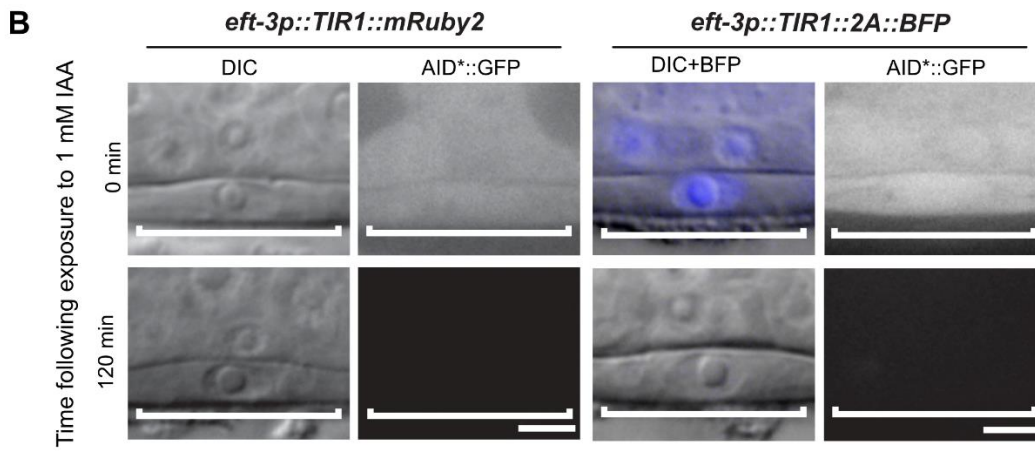
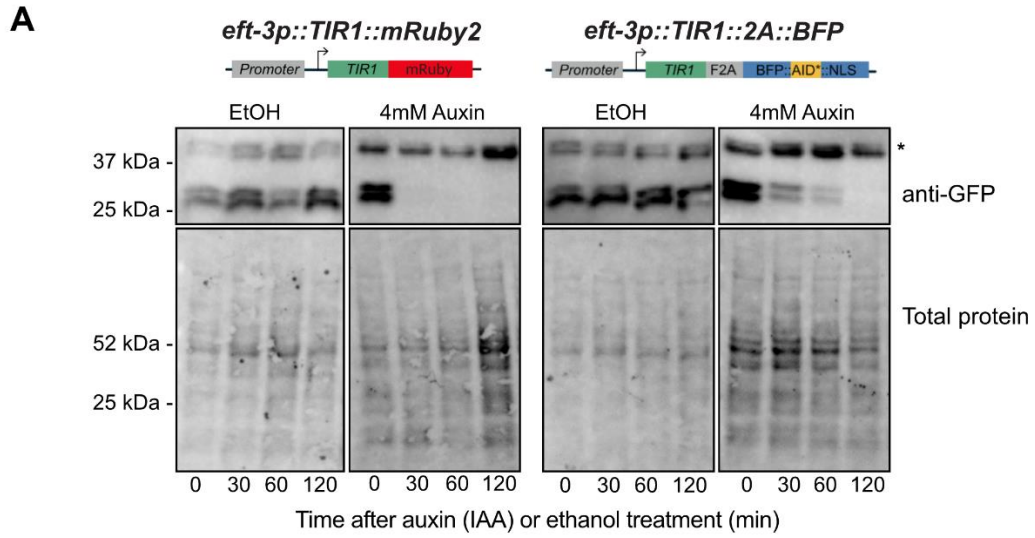


Figure 4. *eft-3p::TIR1::F2A::BFP::AID*::NLS* depletes *AID*::GFP* to the same extent as *eft-3p::TIR1::mRuby2* but exhibits a slower rate of degradation. A) Western blots detecting *AID*::GFP* after exposure to IAA or EtOH (control). An *AID*::GFP* reporter strain was crossed to either *eft-3p::TIR1::mRuby2* (left) or *eft-3p::TIR1::F2A::BFP::AID*::NLS* (right) and then exposed to 4 mM IAA or EtOH for 0 min, 30 min, 60 min, or 120 min. Anti-GFP blots (top) showing background band (marked with *) and a doublet at approximately 27 kDa, consistent with the predicted size of GFP. B) Representative images of *AID*::GFP* depletion in animals carrying either *eft-3p::TIR1::mRuby2* or *eft-3p::TIR1::F2A::BFP::AID*::NLS*. For animals expressing *eft-3p::TIR1::F2A::BFP::AID*::NLS*, an overlay of DIC and BFP images is provided. DIC and corresponding GFP images of VPCs (brackets) from L3 larvae at the P6.p 1-cell stage. Animals were treated with 1 mM IAA for the specified time and then imaged to visualize loss of *AID*::GFP*. Representative images from additional timepoints can be found in Figure S2. Scale bars represent 5 μ m. C) *AID*::GFP* degradation kinetics. Rates of degradation were determined by quantifying *AID*::GFP* levels in VPCs of animals as described above. Animals were exposed to 1 mM K-NAA or IAA from 0 to 120 minutes at intervals of 30 min. The graph depicts the mean normalized fluorescent intensity from 10 or more animals from a single experimental replicate. Error bars indicate standard deviation.

To further test the performance of *TIR1::F2A::BFP::AID*::NLS* for depleting an endogenous *AID*-tagged protein, we compared depletion in the *eft-3p::TIR1::F2A::BFP::AID*::NLS; nhr-25::GFP::AID*::3xFLAG* strain to depletion in the previously described *eft-3p::TIR1::mRuby2; nhr-25::GFP::AID*::3xFLAG* strain (Martinez *et al.* 2020). Similar to the *AID*::GFP* experiments, we performed single cell quantitative imaging experiments (Figure 5). With the *eft-3p::TIR1::mRuby2* transgene we observed undetectable *NHR-25::GFP::AID*::3XFLAG* in both seam cells and VPCs within 30 minutes of exposure to IAA or K-NAA (Figure 5, Figure S2). In contrast, we observed differences in IAA and K-NAA treatment using our *eft-3p::TIR1::F2A::BFP::AID*::NLS; nhr-25::GFP::AID*::3xFLAG* strain (Figure 5, Figure S2). K-NAA resulted in more rapid *NHR-25::GFP::AID*::3xFLAG* depletion by *TIR1::F2A::BFP::AID*::NLS* compared to IAA (Figure 5, Figure S2). In VPCs, *NHR-25::GFP::AID** was robustly depleted after 60 minutes of exposure to K-NAA and undetectable after 90 minutes (Figure 5B, Figure

S2). There appeared to be tissue-specific differences in depletion rates as NHR-25::GFP::AID*::3xFLAG was undetectable in seam cells 60 minutes after exposure to K-NAA (Figure 5C, Figure S2). Depletion rates were slower with IAA, taking an additional 30 minutes for TIR1::F2A::BFP::AID*::NLS to deplete NHR-25::GFP::AID*::3xFLAG to undetectable levels (Figure 5, Figure S2). These results suggest that: i) some element of our TIR1::F2A::BFP::AID*::NLS transgene is limiting depletion rate; ii) we reach the same depletion endpoint using our TIR1::F2A::BFP::AID*::NLS transgene; iii) there can be tissue-specific differences in depletion rates; and iv) K-NAA performed equal to or better than IAA in these depletion experiments. These results suggest that one should test IAA and K-NAA for depletion efficiency independently for each TIR1 expression system and AID*-tagged protein.

Ashley *et al.* (2020) Figure 5

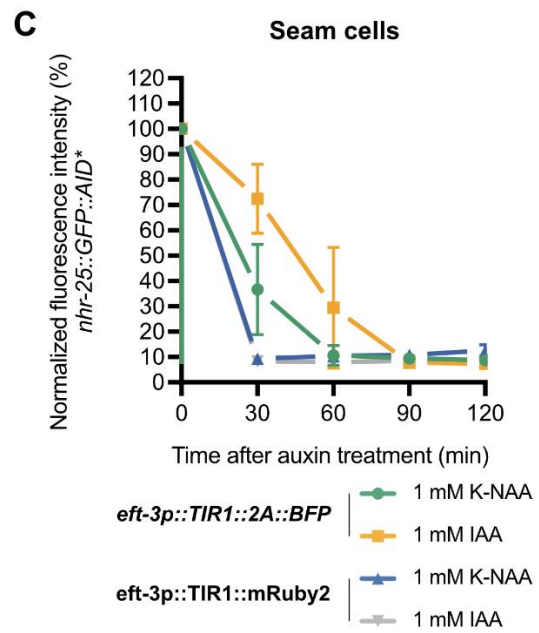
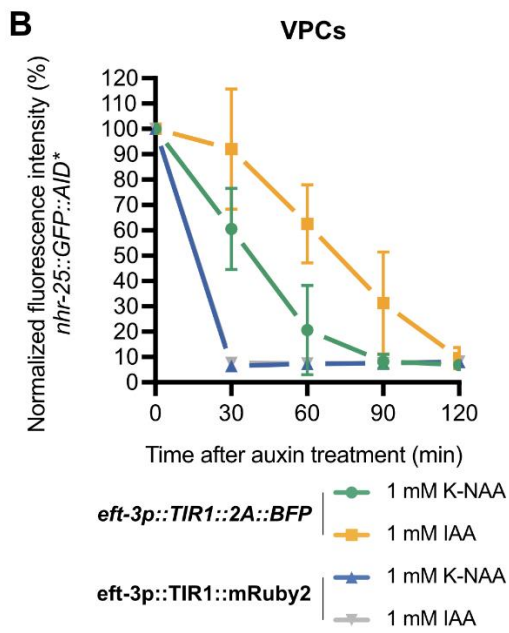
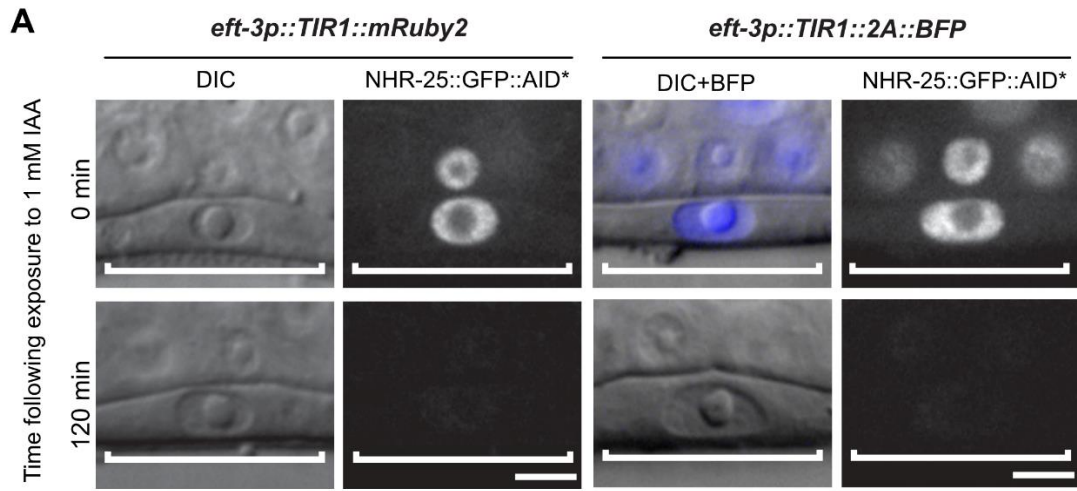


Figure 5. *eft-3p::TIR1::F2A::BFP::AID*::NLS* depletes *NHR-25::GFP::AID to the same extent as *eft-3p::TIR1::mRuby2* but also exhibits a slower degradation rate.** A) Representative images of *NHR-25::GFP::AID** depletion in VPCs of animals expressing either *eft-3p::TIR1::mRuby2* or *eft-3p::TIR1::F2A::BFP::AID*::NLS*. For animals expressing *eft-3p::TIR1::F2A::BFP::AID*::NLS*, an overlay of DIC and BFP images were used to demonstrate BFP internal control expression in VPCs. DIC and corresponding GFP images of VPCs (brackets) from L3 larvae at the P6.p 1-cell stage. Animals were treated with 1 mM IAA for the specified time and then imaged to visualize loss of *NHR-25::GFP::AID**. Additional timepoints can be found in figure S2. Scale bars represent 5 μ m. *NHR-25::GFP::AID** degradation kinetics in B) VPCs and C) seam cells. Kinetics were determined by measuring *NHR-25::GFP::AID** levels in L3s (as described above) exposed to 1 mM K-NAA or IAA. The graph depicts the mean normalized fluorescent intensity from 10 or more animals from a single experimental replicate. Error bars indicate standard deviation.

***eft-3p::TIR1::F2A::BFP::AID*::NLS* produces comparable depletion phenotypes as *eft-3p::TIR1::mRuby2* for depleting both nuclear and cytoplasmic proteins**

Given the slower depletion kinetics we observed in our *eft-3p::TIR1::F2A::BFP::AID*::NLS* strain for an *AID*::GFP* reporter and *NHR:25::GFP::AID*::3xFLAG*, we wanted to test the impact of this slowed depletion rate at the phenotypic level. We first tested the two *TIR1* alleles on our *nhr-25::GFP::AID*::3xFLAG* strain (Table 2 and Table S5). With the *TIR1::mRuby2* transgene and IAA, we observed that 61% of *nhr-25::GFP::AID*::3xFLAG* larvae arrested, and the remaining 39% of animals that made it to adulthood had gonadal abnormalities (Table 2 and Table S5). With our *TIR1::F2A::BFP::AID*::NLS* transgene, we observed that 85% of larvae arrested, while 93% of animals that reached adulthood had gonadal abnormalities (Table 2 and Table S5). Surprisingly, with growth on K-NAA we did not observe any larval arrests for either strain, but all adult animals had gonadal defects (Table 2 and Table S5). We next tested the two different *TIR1* strains on an *nhr-23::AID*::3xFLAG*

allele (Zhang *et al.* 2015). Similar to previous reports (Zhang *et al.* 2015), we observed a completely penetrant larval arrest with both the *nhr-23::AID*::3xFLAG; eft-3p::TIR1::mRuby2* and *nhr-23::AID*::3xFLAG, eft-3p::TIR1::F2A::BFP::AID*::NLS* strains grown on either IAA or K-NAA. Interestingly, some of the arrested larvae produced by growth on K-NAA died (Table S5), which we did not see on IAA and is consistent with a stronger phenotype. None of the strains tested presented any defects on MYOB or ethanol control plates (Table 2 and Table S5). Finally, we wished to test an additional cytoplasmic AID*-tagged protein for depletion phenotypes. We chose DAF-15/Raptor, a lysosome-localized factor which causes larval arrest when depleted (Duong *et al.* 2020). Both *eft-3p::TIR1::mRuby2* and *eft-3p::TIR1::F2A::BFP::AID*::NLS* caused a completely penetrant larval arrest in animals carrying the *daf-15::mNeonGreen::AID** (Table 3 and Table S6). Strains grown on IAA arrested at L2, while strains grown on K-NAA arrested at L3 (Table 3 and Table S6). Based on previous work (Duong *et al.* 2020), these results suggests that K-NAA is producing slower or less complete DAF-15::mNG::AID* depletion than IAA. For DAF-15::mNG::AID*, IAA appeared to perform better. For all strains tested, we observed wild-type growth on control media (Table 2, Table 3, Table S5, and Table S6). Together, these results indicated that our *eft-3p::TIR1::F2A::BFP::AID*::NLS* transgene performs comparably to the original *eft-3p::TIR1::mRuby2* with respect to phenocopying mutant phenotypes of NHR-23, NHR-25, and DAF-15.

Table 2. *eft-3p::TIR1::F2A::BFP::AID*::NLS* produces comparable depletion phenotypes to *eft-3p::TIR1::mRuby2* for depleting nuclear proteins.

<i>eft-3p::TIR1</i> transgene	AID-tagged allele	Treatment	% WT developmental rate	% Larval arrest	% Gonadal abnormalities among adults
<i>TIR1::mRuby2</i>	n/a	Control	100	0	0
<i>TIR1::mRuby2</i>	n/a	IAA	100	0	0
<i>TIR1::mRuby2</i>	n/a	K-NAA	100	0	0
<i>TIR1::2A::BFP</i>	n/a	Control	100	0	0
<i>TIR1::2A::BFP</i>	n/a	IAA	100	0	0
<i>TIR1::2A::BFP</i>	n/a	K-NAA	100	0	0
<i>TIR1::mRuby2</i>	<i>nhr-23(kry61[nhr-23::AID*::TEV-3xFLAG])</i>	Control	100	0	0
<i>TIR1::mRuby2</i>	<i>nhr-23(kry61[nhr-23::AID*::TEV-3xFLAG])</i>	IAA	0	100	0
<i>TIR1::mRuby2</i>	<i>nhr-23(kry61[nhr-23::AID*::TEV-3xFLAG])</i>	K-NAA	0	100	0
<i>TIR1::2A::BFP</i>	<i>nhr-23(kry61[nhr-23::AID*::TEV-3xFLAG])</i>	Control	100	0	0
<i>TIR1::2A::BFP</i>	<i>nhr-23(kry61[nhr-23::AID*::TEV-3xFLAG])</i>	IAA	0	100	0
<i>TIR1::2A::BFP</i>	<i>nhr-23(kry61[nhr-23::AID*::TEV-3xFLAG])</i>	K-NAA	0	100	0
<i>TIR1::mRuby2</i>	<i>nhr-25(wrd18[nhr-25::GFP^AID*::3xFLAG])</i>	Control	100	0	0
<i>TIR1::mRuby2</i>	<i>nhr-25(wrd18[nhr-25::GFP^AID*::3xFLAG])</i>	IAA	39	61	100
<i>TIR1::mRuby2</i>	<i>nhr-25(wrd18[nhr-25::GFP^AID*::3xFLAG])</i>	K-NAA	100	0	100
<i>TIR1::2A::BFP</i>	<i>nhr-25(wrd52[nhr-25::GFP^AID*::3xFLAG])</i>	Control	100	0	0
<i>TIR1::2A::BFP</i>	<i>nhr-25(wrd52[nhr-25::GFP^AID*::3xFLAG])</i>	IAA	15	85	93
<i>TIR1::2A::BFP</i>	<i>nhr-25(wrd52[nhr-25::GFP^AID*::3xFLAG])</i>	K-NAA	100	0	100

Table 3. *eft-3p::TIR1::F2A::BFP::AID*::NLS* produces comparable depletion phenotypes to *eft-3p::TIR1::mRuby2* for depleting cytoplasmic proteins.

<i>eft-3p::TIR1</i> transgene	AID-tagged allele	Treatment	% WT developmental rate	% L2 arrest	% L3 arrest
<i>TIR1::mRuby2</i>	<i>daf-15(re257[daf-15::mNG::AID*])</i>	Control	100	0	0
<i>TIR1::mRuby2</i>	<i>daf-15(re257[daf-15::mNG::AID*])</i>	IAA	0	100	0
<i>TIR1::mRuby2</i>	<i>daf-15(re257[daf-15::mNG::AID*])</i>	K-NAA	0	0	100
<i>TIR1::2A::BFP</i>	<i>daf-15(re257[daf-15::mNG::AID*])</i>	Control	100	0	0
<i>TIR1::2A::BFP</i>	<i>daf-15(re257[daf-15::mNG::AID*])</i>	IAA	0	100	0
<i>TIR1::2A::BFP</i>	<i>daf-15(re257[daf-15::mNG::AID*])</i>	K-NAA	0	0	100


Synchronized animals (n=120-240) of the indicated genotype were grown on the indicated plates (control, IAA, K-NAA). Animals were grown at 20°C for 4 days and scored for larval arrest. Wild-type (WT) developmental rate was determined by scoring animals that reached adulthood after 3 days at 20°C. L2 and L3 arrest were determined by animal size and gonadal development.

A new suite of TIR1 driver strains compatible with red/green FP imaging

Having confirmed our *TIR1::F2A::BFP::AID*::NLS* transgene functioned effectively in both embryos and somatic cells, we wished to create a suite of strains for tissue-specific TIR1 expression (Figure 6A). We created chromosome I and II knock-ins expressing TIR1 in the germline (*mex-5p* and *sun-1p*), hypodermis (*dpy-7p* and *col-10p*), muscle (*unc-54p*), and intestine (*ges-1p*) (Figure 6, Figure S4). We also created chromosome I knock-ins expressing TIR1 in neurons (*rgef-1p*), pharynx (*myo-2p*), body wall muscle (*myo-3p*), the anchor cell (*cdh-3*), as well as the excretory cell, hypodermis, and gut (*vha-8p*) (Figure 6, Figure S4). The *vha-8* promoter also drove expression in unidentified cells in the head. Additionally, we generated a strain expressing TIR1 in the hypodermal seam cells using a minimal SCMP enhancer (gift from Prof. Allison Woollard) with the *pes-10* minimal promoter (Figure 6A). While we observed robust seam cell expression in this strain, we also detected hypodermal expression (unpublished data). We are making this strain available to the community but encourage careful evaluation before interpretation.

Ashley et al. (2020) Figure 6

A TIR1 driver strains



Strain	Promoter	Tissue	Genotype	Insertion site
LP869	<i>vha-8p</i>	Excretory cells, Hypodermis, Gut, unidentified head cells	<i>cpSi171[vha-8p::TIR1::F2A::BFP::AID*::NLS::tbb-2 3'UTR]</i>	I:-5.32
JDW225	<i>eft-3p</i>	Soma	<i>wrdsi23[eft-3p::TIR1::F2A::BFP::AID*::NLS::tbb-2 3'UTR]</i>	I:-5.32
DV3799	<i>col-10p</i>	Hypodermis	<i>reSi1[col-10p::TIR1::F2A::BFP::AID*::NLS::tbb-2 3'UTR]</i>	I:-5.32
DV3800	<i>col-10p</i>		<i>reSi2[col-10p::TIR1::F2A::BFP::AID*::NLS::tbb-2 3'UTR]</i>	II:-0.77
JDW227	<i>dpy-7p</i>		<i>wrdsi45[dpy-7p::TIR1::F2A::BFP::AID*::NLS::tbb-2 3'UTR]</i>	II:-0.77
JDW229	<i>dpy-7p</i>		<i>wrdsi47[dpy-7p::TIR1::F2A::BFP::AID*::NLS::tbb-2 3'UTR]</i>	I:-5.32
JDW231	<i>SCMp</i> [‡]	Seam cells and	<i>wrdsi44[SCMp*::TIR1::F2A::BFP::AID*::NLS::tbb-2 3'UTR]</i>	II:-0.77
JDW233	<i>SCMp</i> [‡]	Hypodermis	<i>wrdsi46[SCMp*::TIR1::F2A::BFP::AID*::NLS::tbb-2 3'UTR]</i>	I:-5.32
JDW221	<i>mex-5p</i>	Germline	<i>wrdsi18[mex-5p::TIR1::F2A::BFP::AID*::NLS::tbb-2 3'UTR]</i>	I:-5.32
JDW223	<i>mex-5p</i>		<i>wrdsi35[mex-5p::TIR1::F2A::BFP::AID*::NLS::tbb-2 3'UTR]</i>	II:-0.77
JDW10	<i>sun-1p</i>		<i>wrdsi3[sun-1p::TIR1::F2A::BFP::AID*::NLS::tbb-2 3'UTR]</i>	II:-0.77
DV3801	<i>unc-54p</i>	Muscle	<i>reSi3[unc-54p::TIR1::F2A::BFP::AID*::NLS::tbb-2 3'UTR]</i>	I:-5.32
DV3825	<i>unc-54p</i>		<i>reSi11[unc-54p::TIR1::F2A::BFP::AID*::NLS::tbb-2 3'UTR]</i>	II:-0.77
LP871	<i>myo-3p</i>		<i>cpSi174[myo-3p::TIR1::F2A::BFP::AID*::NLS::tbb-2 3'UTR]</i>	I:-5.32
DV3803	<i>ges-1p</i>	Intestine	<i>reSi5[ges-1p::TIR1::F2A::BFP::AID*::NLS::tbb-2 3'UTR]</i>	I:-5.32
DV3826	<i>ges-1p</i>		<i>reSi12[ges-1p::TIR1::F2A::BFP::AID*::NLS::tbb-2 3'UTR]</i>	II:-0.77
DV3805	<i>rgef-1p</i>	Neuron	<i>reSi7[rgef-1p::TIR1::F2A::BFP::AID*::NLS::tbb-2 3'UTR]</i>	I:-5.32
DQM526	<i>cdh-3p</i>	Anchor cells, Seam cells, L4 Vulval precursor cells	<i>bmd176[cdh-3p::TIR1::F2A::BFP::AID*::NLS::tbb-2 3'UTR]</i>	II:-0.77
LP870	<i>myo-2p</i>	Pharynx	<i>cpSi172[myo-2p::TIR1::F2A::BFP::AID*::NLS::tbb-2 3'UTR]</i>	I:-5.32

[‡] SCM promoter is a 573bp enhancer from *arf-3* intronic sequence + *pes-10A*

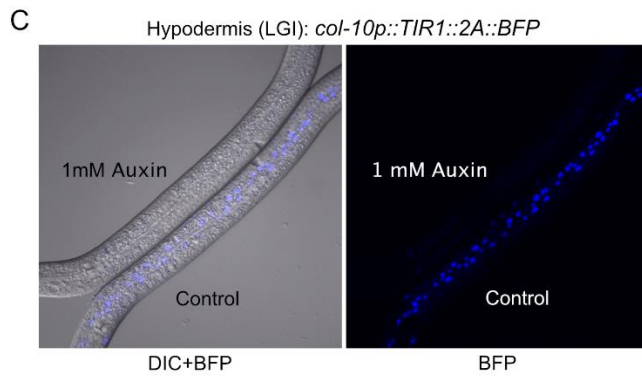
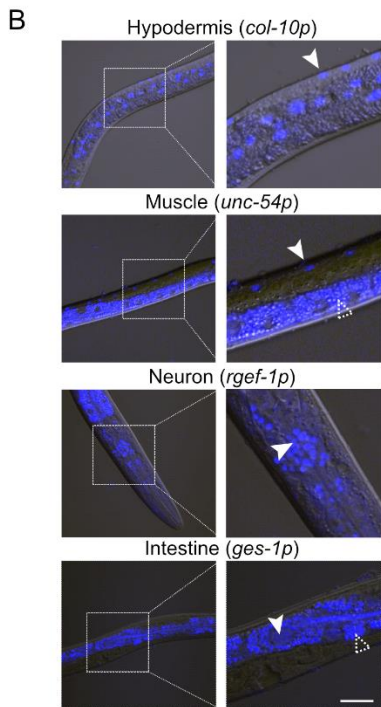


Figure 6. A new suite of TIR1 expression strains for tissue-specific depletion of AID-tagged proteins in *C. elegans*. A) Table describing new suite of TIR1::F2A::BFP::AID*::NLS strains. Strain names, promoter driving TIR1, tissue of expression, genotype, and insertion site are provided for each strain. The insertion sites are the genomic loci where the Mos1 transposon landed in the ttTi4348 and ttTi5605 insertion alleles. We note that our knock-ins were generated using CRISPR/Cas9-mediated genome editing in wild-type animals or in strains stably expressing Cas9 in the germline; there is no Mos1 transposon in these loci in these genetic backgrounds. B) BFP is detected in the expected nuclei of strains expressing TIR1 cassettes driven by *col-10p* (hypodermis), *unc-54p* (muscle), *ges-1p* (intestine), and *rgef-1p* (neurons). Representative BFP-expressing nuclei are indicated by solid arrows. Scale bars represent 20 μ m. Note that the fluorescence signal at the bottom of the muscle image and surrounding the nuclei in the intestinal image is intestinal autofluorescence, indicated by an unfilled arrow with a dashed outline. C) Functional test of TIR1 activity in a *col-10p::TIR1::F2A::BFP::AID*::NLS* strain (DV3799). Hypodermal BFP expression is lost when animals are exposed to 1 mM auxin for three hours, but not when similarly grown on control plates.

All of the TIR1-expressing strains that we have deposited in the *Caenorhabditis* Genetics Center have detectable BFP expression that is lost when animals are shifted onto auxin plates, confirming TIR1 is active (Figures 2B, 6C, S2, and S4). However, an unanswered question is the importance of TIR1 expression levels for effective depletion of AID*-tagged proteins. Motivated by an interest in NHR-25 in gene regulation (Ward *et al.* 2013, 2014) and anchor cell (AC) invasion (Matus *et al.* 2015; Medwig and Matus 2017; Medwig-Kinney *et al.* 2020), we generated a strain to study early events in AC differentiation (DQM623; Figure 7). The *cdh-3* promoter drives transgene expression in the AC but not vulval precursor cells (VPCs) during early AC differentiation (Matus *et al.* 2015). The promoter becomes active in L4 VPCs and also drives expression in seam cells and neurons (Matus *et al.* 2015). We generated a *cdh-3p::TIR1::F2A::BFP::AID*::NLS* strain, but were not able to detect any BFP expression. To perform a functional test, we crossed the *nhr-25::GFP::AID*::3xFLAG*

allele into the strain harboring *cdh-3p::TIR1::F2A::BFP::AID*::NLS*. We had previously demonstrated significant depletion of NHR-25 in ACs and VPCs using a strongly expressed *eft-3p::TIR1::mRuby2* transgene (Martinez *et al.* 2020). Strikingly, we observed auxin-dependent depletion of NHR-25::GFP::AID*::3xFLAG in the AC but no depletion in the adjacent VPCs (Figure 7). Thus, even if the presence of TIR1 is undetectable through BFP reporter expression, there may still be a sufficient amount of TIR1 to deplete proteins of interest.

Ashley *et al.* (2020) Figure 7

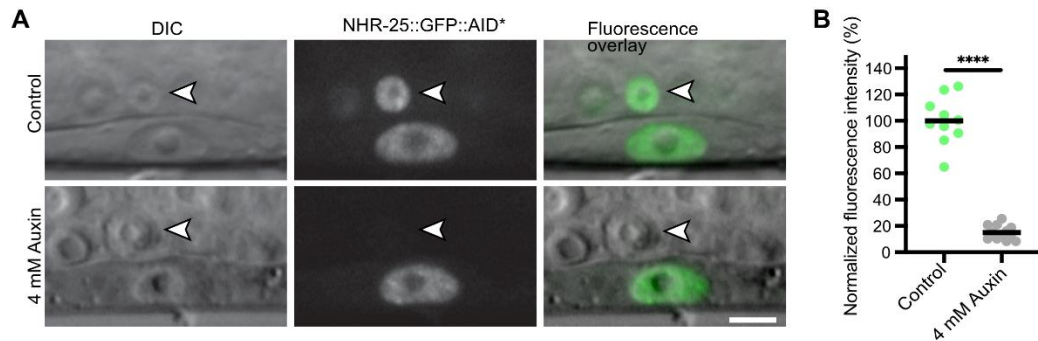


Figure 7. NHR-25::GFP::AID*::3xFLAG can be depleted in a cell-specific manner in a strain with undetectable TIR1 expression via a BFP reporter. A) An anchor cell (AC)-specific TIR1 transgene (*cdh-3p::TIR1::F2A::BFP::AID*::NLS*) did not produce observable BFP in the AC. Crossing this strain to an *nhr-25::GFP::AID*::3xFLAG* allele resulted in depletion of NHR-25 in the AC when exposed to 4 mM auxin for 1 hr (indicated by white arrow with black outline). As expected, depletion of NHR-25 was not observed in the neighboring uterine cells or the underlying vulval precursor cells (VPCs). Scale bar represents 5 μ m. B) Quantification of NHR-25::GFP::AID*::3xFLAG in ACs following auxin (K-NAA) treatment. Individual data points from a single replicate with more than 10 animals per condition are presented. The horizontal black bar depicts the mean for each condition; **** indicates $P < 0.0001$ by a two-tailed unpaired Student's t-test. $P < 0.05$ was considered statistically significant. Scale bars represent 5 μ m

Vectors to generate FP::AID* knock-ins

There are two commonly used CRISPR/Cas9 editing strategies currently used in *C. elegans* (Dickinson and Goldstein 2016; Nance and Frøkjær-Jensen 2019). One uses injection of Cas9 ribonucleoprotein complexes and typically provides linear DNA repair templates (Paix *et al.* 2015; Dokshin *et al.* 2018; Ghanta and Mello 2020). The other approach uses injection of plasmids expressing Cas9 and sgRNA, and typically provides repair templates as plasmids with selectable markers (Dickinson *et al.* 2013, 2015; Norris *et al.* 2015; Schwartz and

Jorgensen 2016). We created plasmids to facilitate assembly of repair templates for both of these genome editing strategies.

First, we generated a set of vectors to create SEC-selectable plasmid repair templates. We took a set of vectors which use Gibson assembly to generate the final repair template (Dickinson *et al.* 2015) and introduced AID* sequences upstream of the 3xFLAG epitope. This set of vectors allows for tagging genes with mNeonGreen, GFP, YPET, mKate2, and TagRFP-T along with AID*::3xFLAG epitopes (Figure 8, Table S2). Methods in *C. elegans* using biotin ligases and biotin acceptor peptides have recently been described for protein affinity purification (Waaijers *et al.* 2016), proximity labeling (Branon *et al.* 2018), native chromatin purification (Ooi *et al.* 2010), and cell-type specific nuclei purification (Steiner *et al.* 2012). To support these approaches, we have made a set of FP^SEC^BioTag::AID*::3xFLAG vectors with GFP, TagRFP-T, and mKate2 (Figure 8, Table S2).

Another approach to generate plasmid repair templates with detectable markers is a Golden Gate assembly approach known as SapTrap (Engler *et al.* 2009; Schwartz and Jorgensen 2016). A library of SapTrap donor plasmids contain protein tags, selectable markers, and fluorescent proteins; these tags can be assembled in a desired order in a one-tube isothermal reaction to allow the creation of new repair templates (Schwartz and Jorgensen 2016; Dickinson *et al.* 2018) (Figure 8D). When trying to create SapTrap assemblies containing nine fragments, we encountered very poor cloning efficiencies. We therefore created a series of pre-assembled “multi-cassettes,” where we combined fragments that we

frequently use (Figure 8E, Table S2). These constructs contain inserts for SapTrap N-terminal and C-terminal connector modules, as described by Schwartz et al. (2016) and include various combinations of AID* cassettes, and epitopes for protein purification or detection (3xMyc, 3xFLAG, BioTag). This approach restored high cloning efficiency. For our most commonly used vectors, we have generated constructs containing full assemblies of the knock-in epitope, lacking only the homology arms. PCR amplifying homology arms with SapI sites and appropriate connectors allows high-efficiency generation of repair templates.

Ashley et al. (2020) Figure 8

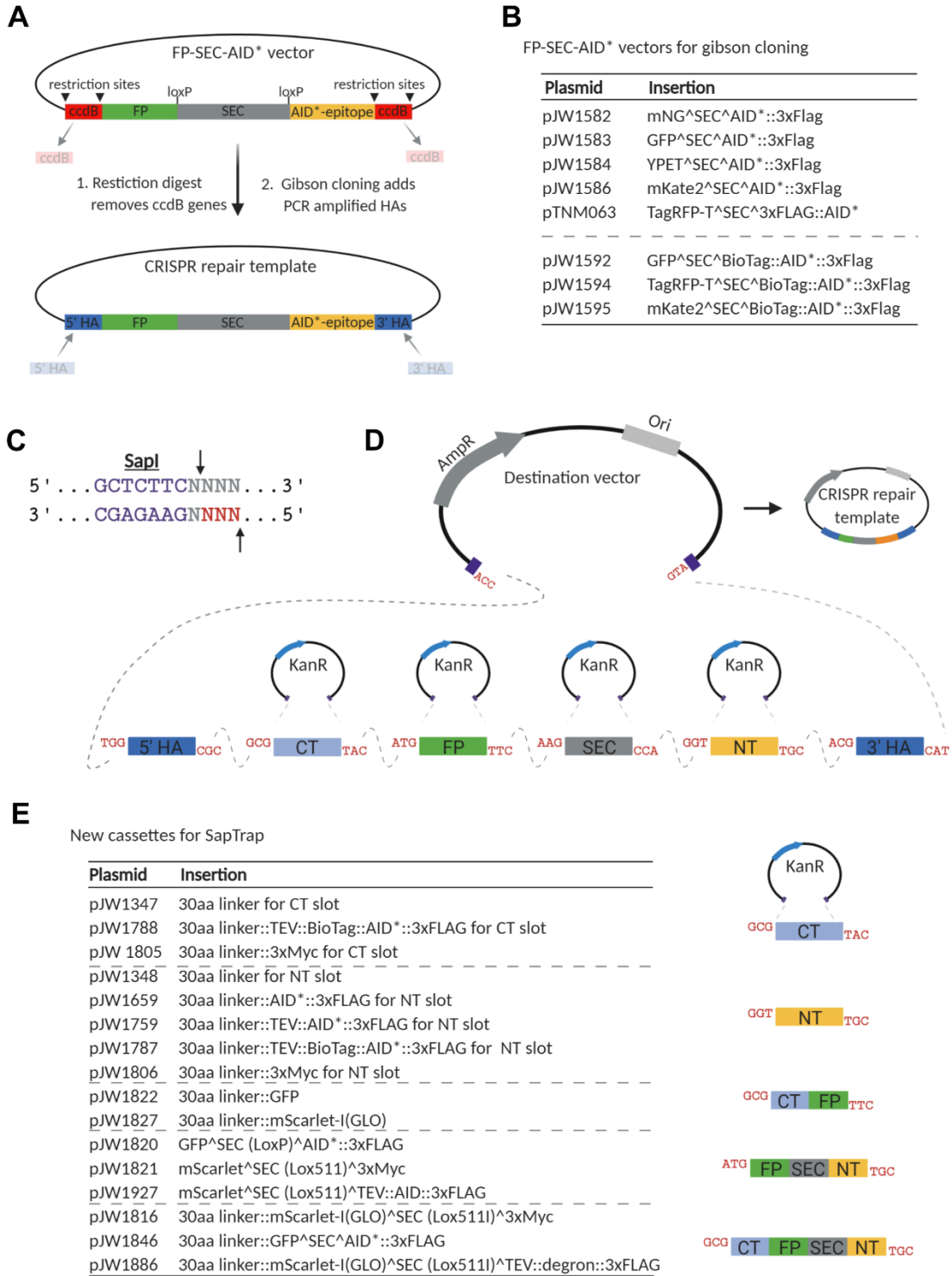


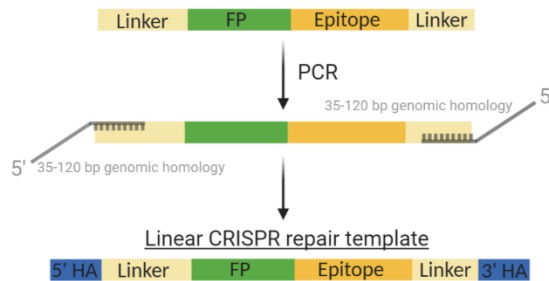
Figure 8. A collection of vectors to generate FP::AID* knock-ins through Gibson cloning and a suite of new vectors for the SapTrap cloning system. A) Schematic of the AID*-containing vectors produced by modifying the set of vectors originally described by Dickinson *et al.* (2015). An AID* epitope was inserted downstream of the loxP-flanked SEC. New repair templates for CRISPR/Cas9-mediated genome editing can be produced by restriction digestion of the vector and Gibson cloning of PCR-derived 5' and 3' homology arms (5'HA and 3'HA), as described (Dickinson *et al.*, 2015). Counter-selection against the parent vector is provided by *ccdB* cassettes. B) A suite of new FP::AID* SEC plasmids. The vectors described in Dickinson *et al.* (2015) have been modified to insert an AID* or 23 amino acid biotin acceptor peptide (BioTag)::AID* cassette between the SEC and 3xFLAG cassette. C) *SapI* is a type II restriction enzyme that cuts one base pair and four base pairs outside of its binding site, allowing for the generation of programmable 3 bp sticky ends. D) SapTrap cloning facilitates single-reaction cloning of multiple fragments, in the correct order, into a single repair template plasmid. Specific sticky ends are used for specific cassettes as described by Schwartz *et al.* (2016). E) Table of new vectors generated for the SapTrap CT and NT slots. Our initial assembly efficiencies were sub-optimal, and we found that reducing the number of fragments assembled improved our efficiencies. We have generated a set of multi-cassettes where partial assemblies (CT-FP, FP-SEC-NT, and CT-FP-SEC-NT) have been cloned, simplifying the SapTrap reactions and reducing the number of fragments required. 5'HA, 5' homology arm; 3'HA, 3' homology arm; FP, fluorescent protein; SEC, self-excising cassette; CT, C-terminal connector; NT, N-terminal connector.

Using Cas9 ribonucleoprotein complexes with linear repair templates is a common cloning-free approach in *C. elegans* (Paix *et al.* 2014; 2015), and recent refinements have further boosted editing efficiency (Dokshin *et al.* 2018; Ghanta and Mello 2020). We have generated repair templates to tag proteins with GFP, germline optimized mNeonGreen, and germline optimized mScarlet-I (Fielmich *et al.* 2018; Zhang *et al.* 2018) (Figure 9B, Table S2). All plasmids include a Myc or FLAG epitope for antibody-based detection, and we have versions with or without an AID* cassette. These vectors are suitable templates for PCR amplification to generate linear repair templates with short homology arms. FPs can be easily exchanged to generate new constructs by PCR linearization and Gibson cloning.

Linkers flanking the FP allow flexibility in targeting genes of interest and reduce functional interference, permitting N-terminal, C-terminal, or internal tagging.

Ashley *et al.* (2020) Figure 9

A



B

Lnk-FP-Epi-Lnk vectors for Cas-9 RNP-based editing

Plasmid	Insertion
pJW2072	linker::mScarlet-1 (GLO)::3xMyc::linker
pJW2086	linker::GFP::AID*::3xFLAG::linker
pJW2088	linker::GFP::3xFLAG::linker
pJW2098	linker::mScarlet(dpi)::AID*::3xFLAG::linker
pJW2171	linker::mNG(dpi)::AID*::3xFLAG::linker
pJW2172	linker::mNG(dpi)::3xMyc::linker

Figure 9. A collection of vectors to generate FP::AID* knock-ins using linear repair templates. A) Schematic primer design to generate linear repair templates by PCR. Primers with homology to the cassette and 5' homology to the desired integration site are used to amplify a dsDNA repair template. 35-120 bp homology arms (HA in figure) are recommended, as previously described (Paix *et al.* 2014; 2015; Dokshin *et al.* 2018). B) A set of vectors to generate repair templates for Cas9 ribonucleoprotein complex (RNP)-based genome editing. FP (fluorescent protein) and FP::AID* cassettes are flanked by flexible linker sequences. A 30 amino acid sequence is at the 5' end of the cassette, and a 10 amino acid sequence is at the 3' end of the cassette. This design provides flexibility for designing repair templates for N-terminal, C-terminal, or internal tagging. GLO=Germline optimized using algorithm (Fielmich *et al.*, 2018); dpi=silent mutations to remove piRNA binding sites (dpi) to promote germline expression (Zhang *et al.* 2018).

Discussion:

The original *C. elegans* AID system employed a *TIR1::mRuby2* transgene, which was useful for visualizing TIR1 expression and cellular localization (Zhang *et al.* 2015). However, for applications where red fluorescent protein imaging is desired, the *mRuby2* expression could increase background and hamper imaging analysis. We therefore developed a complementary construct containing a *TIR1::F2A::BFP::AID*::NLS* transgene (Figure 2A). TIR1 is unlabeled, and nuclear-localized BFP provides a readout for TIR1 expression (Figure 2, 3, 6, and S2). AID*-tagged BFP is degraded in the presence of auxin, confirming TIR1 activity via degradation of an internal control (Figure 2, 3 and S2). Recent work from our lab demonstrates that our new TIR1 strains are effective for experiments where red FP imaging is desired (Ragle *et al.* 2020).

Our *eft-3p::TIR1::F2A::BFP::AID*::NLS* transgenes produced the same degree of depletion of AID-tagged substrates compared to an *eft-3p::TIR1::mRuby2* transgene (Zhang *et al.* 2015), but the depletion kinetics were slower (Figure 4, Figure 5). Initially concerned about the impact of this slower degradation rate, we tested whether it impacted the phenotypes observed following depletion of two AID*-tagged nuclear proteins (NHR-23 and NHR-25) and an AID*-tagged cytoplasmic protein (DAF-15). In all cases we observed comparable penetrance of expected phenotypes (Table 2, Table 3). Additionally, our *sun-1p::TIR1::F2A::BFP::AID*::NLS* transgene produced equivalent *mNG::AID*::PAR-3* depletion and resultant synchronous cell division as compared to a *sun-1p::TIR1::mRuby2* transgene (Figure 2C and D). Similarly, using a *mex-5p::TIR1::F2A::BFP::AID*::NLS* transgene we

observed complete sterility following NHR-23 or SPE-44 depletion, identical to that observed using *pie-1p* or *sun-1p::TIR1::mRuby2* transgenes (Kasimatis *et al.* 2018; Ragle *et al.* 2020). However, there may be cases where depletion rates affect phenotypic preference, so this point should be taken into consideration when choosing which TIR1 transgene to use.

One open question is why did our BFP reporter slow the depletion of other AID*-tagged substrates? Inefficient F2A processing could lead to a TIR1::2A::BFP fusion protein that could be degraded. However, we were unable to detect such a fusion protein by western blotting, arguing against this possibility (Figure 3B). Another explanation is that some component of the system is limiting under these conditions. Possible candidates for the limiting factor include TIR1 itself, the SCF ligase with which TIR1 interacts (Martinez *et al.* 2020), or proteasomal activity. Pan-neuronal TIR1 expressed from an extrachromosomal array produced much stronger depletion of an AID*-tagged substrate compared to the equivalent TIR1 construct in single-copy (O. Hobert, personal communication). While this observation needs to be explored further, it supports the idea that TIR1 is limiting in some cases. Strong expression of both AID*::GFP and BFP::AID*::NLS could sequester the SCF ligase or proteasome if they were limiting. This sequestration might be expected to produce documented reduction-of-function phenotypes such as defects in cell fate and differentiation, meiotic defects, or embryonic lethality (Kipreos *et al.* 1996; Nayak *et al.* 2002; Kamath *et al.* 2003). As we did not observe any such defects, we favor a model where TIR1 is limiting in our system. Going forward, it will be important to test this model by boosting TIR1 expression using tools such as site-specific integration of arrays or recently

described bipartite gene expression systems (Yoshina *et al.* 2016; Nonet 2020). Another approach may be to fuse the Skp1 subunit of the SCF ubiquitin ligase to TIR1, which has resulted in enhanced degradation efficiency of AID-tagged proteins (Kanke *et al.* 2011). Determining which components of the system are limiting and boosting TIR1 activity has the potential to address the reported issue of incomplete degradation of some AID-tagged proteins and a failure to obtain null phenotypes (Patel and Hobert 2017; Serrano-Saiz *et al.* 2018; Duong *et al.* 2020)

We have compared the performance of natural auxin (IAA) with a synthetic, water-soluble analog (K-NAA) using quantitative imaging and phenotypic assays. In many cases, they produced identical results. For NHR-25::GFP::AID*::3xFLAG depletion, we observed more rapid depletion with K-NAA in two cell types using our *eft-3p::TIR1::F2A::BFP::AID*::NLS* (Figure 5). However, interestingly K-NAA did not produce the larval arrest phenotype in these animals, whereas IAA did (Table 2). It is unclear what is behind the discrepancy between these results; we will need to determine in which cells NHR-25 is acting to promote larval development and how IAA and K-NAA affect its depletion in this cell type.

Additionally, *daf-15::mNG::AID** animals grown on IAA arrested at an earlier larval stage than animals treated with K-NAA (Table 3) consistent with faster and/or more robust depletion (Duong *et al.* 2020). Our results do not indicate that one form of auxin is consistently superior, but rather that one needs to empirically test each auxin, depending on the AID-tagged gene, the TIR1 transgene, and the tissue in which depletion is occurring. As the community tests IAA and K-NAA on more AID*-tagged factors, it will be important to

look for patterns that might emerge in order to better predict which auxin will perform better in specific assays.

For many applications, the AID system offers a powerful method to conditionally degrade proteins in specific tissues and at specific points in development. However, as the system has gained popularity, particular challenges have emerged. While they do not dampen our enthusiasm for the AID system, it is important to be aware of them. The first is the previously discussed issue of incomplete degradation. The second issue is that auxin-independent, TIR1-dependent degradation of certain AID-tagged proteins has been documented in both human cells and in *C. elegans* (Zasadzińska *et al.* 2018; Sathyan *et al.* 2019; Martinez *et al.* 2020; Schiksnis *et al.* 2020). While there are recent solutions to this issue, such as alternate AID systems (Li *et al.* 2019) or additional regulatory components that block auxin-independent degradation of AID-tagged proteins (Sathyan *et al.* 2019), these methods are not compatible with existing *C. elegans* strains using minimal AID tags. Engineering an improved TIR1 that does not promote auxin-independent degradation of minimal AID-tagged proteins would be the preferable solution. A strong candidate are recently described TIR1 mutations that produce 670-1000x stronger binding to a modified auxin, reducing the amount of auxin required for target knockdown (Nishimura *et al.* 2020; Yesbolatova *et al.* 2020). This reagent would be compatible with and improve the performance of the collection of minimal AID-tagged strains, which the *C. elegans* community has already generated. Finally, AID-tagging in rare cases can disrupt protein function. For example, an mNeonGreen::AID* tag caused a mild hypomorph of *unc-3* in the

absence of TIR1 and auxin, suggesting that the presence of the AID* tag was interfering with protein levels (Patel and Hobert 2017). More examples are required to determine rules for optimal AID tag placement in both structured and unstructured domains of proteins. As a precaution, we tend to use long 10-30 amino acid flexible linker sequences to space the AID* tag away from the protein of interest.

The ability to rapidly deplete proteins with temporal and cellular resolution allows precise dissection of the roles of gene products in developmental processes of interest. With the ever-increasing efficiency of genome editing and continued refinement of the AID system, one can envision creating libraries of FP::AID*-tagged genes covering the genome and a bank of TIR1 strains to allow depletion in virtually all cell types. Together, this collection of strains and vectors should facilitate efficient generation and depletion of new FP::AID*-tagged proteins.

Methods

Molecular Biology

In the below constructs, flexible linker sequences ranging from 5-9 glycine/serine residues are used to separate cassettes within constructs (i.e., AID*, 3xFLAG, 3xMyc, TEV protease recognition sites, etc.). Unless otherwise specified, pJW plasmids (Ward lab) were generated by Gibson cloning using an in-house made master mix, as described (Gibson *et al.* 2009). For two-fragment Gibson cloning, 0.63 μ l of each DNA fragment was mixed with 3.75 μ l of the

Gibson master mix and incubated for 1-4 hours at 50°C. Longer reaction times were used for inefficient assemblies. Reactions were then transformed as described in the supplemental methods or stored at -20°C. Detailed methods describing construct generation are provided in supplemental methods (Supplementary File S2). Oligos used to construct plasmids are listed in Table S1. All plasmids used are listed in Table S2. Primer design information for designing homology arms for Gibson and SapTrap cloning is provided in Supplementary File S3. Supplementary File S4 contains sequence files for all plasmids generated for this study.

C. elegans

C. elegans strains were cultured as originally described (Brenner 1974). All strains used in this study are listed in Table S3. The majority of genome editing was performed in N2 (wild type), EG9615 *oxSi1091[mex-5p::Cas9(smu-2 introns) unc-119+] II; unc-119(ed3) III*, or EG9882 *F53A2.9(oxTi1127[mex-5p::Cas9::tbb-2 3'UTR, Phsp-16.41::Cre::tbb-2 3'UTR, Pmyo-2::nls-CyOFP::let-858 3'UTR + lox2272]) III* animals (Table S3). EG9615 and EG9882 (unpublished) stably express Cas9 in the germline and are gifts from Dr. Matthew Schwartz and Dr. Erik Jorgensen. TIR1 was isolated by outcrossing and loss of the *Cas9* allele was confirmed by PCR or loss of *myo-2::NLS::OFP* expression. The *mex-5p*, *myo-2p* and *cdh-3p* strains were generated in specialized genetic backgrounds and then the TIR1 transgene was isolated by outcrossing. The loss of other alleles in the background was confirmed by PCR genotyping. Details are provided in Supplemental File 2 and Table S4. Specific details for the TIR1 strains (injection strain, Cas9 and sgRNA source, number of times outcrossed to an N2 background) are provided in Table S4. We note that we are reporting the final, SEC-excised

strains in this table. We have made the precursor strains containing the SEC available to the CGC for our *mex-5p* and *eft-3p* strains: JDW220 *wrdSi10[mex-5p::TIR1::F2A::BFP::tbb-2 3'UTR+SEC]* I:-5.32, JDW222 *wrdSi8[mex-5p::TIR1::F2A::BFP::tbb-2 3'UTR + SEC]* II:-0.77, and JDW224 *wrdSi22[eft-3p::TIR1::F2A::BFP::tbb-2 3'UTR+SEC]* I:-5.32. Following SEC-excision, chromosome I knock-ins can be PCR genotyped using oligos 2835+2836+3415 (Table S1). A wild-type locus produces a 623 bp band and the TIR1 knock-in produces an 881 bp band. Chromosome II knock-ins can be similarly genotyped post-SEC excision by PCR with oligos 273+274+3415 (Table S1). A wild-type locus produces a 684 bp band and a TIR1 knock-in produces an 881 bp band.

CRISPR/Cas9-based genome editing

All TIR1 strains were generated through SEC selection-based genome editing as previously described (Dickinson *et al.* 2015). Single-copy transgenes were inserted into the chromosome I and II loci where the ttTi4348 and ttTi5605 transposons are inserted for MosSCI (Frøkjær-Jensen *et al.* 2008; Frøkjær-Jensen *et al.* 2012), respectively. The genetic map positions for these insertions are provided in the genotype information. In Table S5, we detail the genetic background in which injections were performed, which Cas9 and sgRNA plasmids were used, and how many times the strains were outcrossed against an N2 background. Repair templates were used at 10 ng/μl and Cas9+sgRNA or sgRNA plasmids were used at 50 ng/μl.

Auxin treatment

The Dickinson and Reiner labs routinely use 1 mM IAA, while the Matus and Goldstein lab routinely use 1 mM K-NAA for experiments. The Ward lab routinely uses 4 mM IAA as a stronger NHR-25 depletion phenotype (embryonic lethality) is observed at 4 mM IAA, but not at 1 mM IAA (Zhang *et al.* 2015). In addition, a sterility phenotype produced by depleting NHR-23 in the germline is more penetrant and reproducible on 4 mM IAA compared to 1 mM IAA (unpublished data). Therefore, the western blots (Figure 3B, Figure 4A) and phenotypic assays (Tables 2, 3, S5, S6) were performed using 4 mM IAA or K-NAA to provide the strongest possible depletion. For DQM623 imaging (Figure 7), we also used a higher concentration of auxin (4 mM K-NAA), as we could not detect BFP reporter expression from the *bmd176[cdh-3pTIR1::F2A::mTagBFP2::AID::NLS]* transgene and wanted to design the experiment to achieve the strongest possible depletion of NHR-25. Controls for experiments using IAA are NGM plates with an equivalent concentration of ethanol vehicle. Controls for experiments using K-NAA are NGM plates.

BFP::AID*::NLS reporter depletion experiments

For Figure 2B, LP630 *cpls103[sun-1p::TIR1-C1::F2A::mTagBFP2-C1::AID*::NLS + SEC II:-0.77]*

// L4 larvae were placed on standard NGM plates containing 1 mM Auxin or 4% ethanol (control) and kept at 22°C overnight. Young adults were then mounted on 3% agar pads containing 10 mM sodium azide as a paralytic. Images were acquired on a Nikon TiE microscope equipped with a 405 nm diode laser for fluorescence excitation; a 20x air objective and 1.2x tube lens (total magnification of 24x); a CSU-X1 spinning disk head; and a

Hamamatsu ImageEM EM-CCD camera. Acquisition was controlled by MetaMorph software, and images were prepared for display by cropping, rotating and adjusting brightness and contrast using ImageJ. No other image manipulations were performed.

For DV3799 *reSi1[col-10p::TIR1::F2A::mTagBFP2::AID*::NLS::tbb-2 3'UTR I:-5.32]*, DV3801 *reSi3[unc-54P::TIR1::F2A::mTagBFP2::AID*::NLS::tbb-2 3'UTR I:-5.32]*, DV3803 *reSi5[ges-1p::TIR1::F2A::mTagBFP2::AID*::NLS::tbb-2 3'UTR I:-5.32]*, and DV3805 *reSi7[rgef-1p::TIR1::F2A::mTagBFP2::AID*::NLS::tbb-2 3'UTR I:-5.32]* (Figure 6), we made an auxin (IAA) (Alpha Aesar, #A10556) stock solution (400 mM in ethanol) that was stored at 4°C for up to one month. A 16 mM auxin working solution was then prepared freshly by diluting 1:25 in filtered water with 4% ethanol final concentration. 500 µL of 16 mM auxin was added to 60 mm NGM plates for a final concentration of 1 mM, with 4% ethanol as vehicle control (plates contain approximately 8 ml of agar). Plates were then seeded with OP50. Larvae were grown on NGM plates to the desired stage, then shifted onto auxin or vehicle plates for 3 hours before imaging. Animals were anesthetized with 5 mM tetramisole and images were acquired on a Nikon A1si Confocal Laser Microscope using a Plan-Apochromat 40x/1.4 DIC objective and DS-Fi2 camera. Images were analyzed using NIS Elements Advanced Research, Version 4.40 software (Nikon).

For JDW221 *wrdsi18[mex-5p::TIR1::F2A::mTagBFP2::AID*::NLS::tbb-2 3'UTR I:-5.32]*, JDW225 *wrdsi23[eft-3p::TIR1::F2A::mTagBFP2::AID*::NLS::tbb-2 3'UTR I:-5.32]*, JDW229 *wrdsi47[dpy-7p::TIR1::F2A::mTagBFP2::AID*::NLS::tbb-2 3'UTR I:-5.32]* (Figure S4), 1-hour

auxin treatments were performed. Animals were synchronized at the L1 larval stage by sodium hypochlorite treatment and moved to nematode growth media (NGM) plates seeded with *E. coli* OP50. At the young adult stage, JDW221 worms were either kept on OP50-seeded NGM plates (control) or moved to plates treated with 1 mM K-NAA (Phyto-Technology Laboratories, N610) (Martinez and Matus 2020). At the mid-L3 larval stage, JDW225 and JDW229 worms were either kept on OP50-seeded NGM plates or moved to plates treated with 1 mM K-NAA. OP50-seeded NGM plates containing K-NAA were prepared as described (Martinez and Matus 2020). Images were acquired on a custom-built upright spinning-disk confocal microscope consisting of a Zeiss Axio Imager.A2 modified with a Borealis-modified Yokogawa CSU-10 confocal scanner unit with 405 nm lasers and 488 nm lasers and equipped with a Hamamatsu Orca EM-CCD camera. Images shown for JDW221 (pachytene region) were acquired using a Plan-Apochromat 40x/1.4 DIC objective. Images shown for JDW225 (uterine and vulval tissues) and JDW229 (hypodermal cells) were acquired using a Plan-Apochromat 100x/1.4 DIC objective. MetaMorph software (version: 7.8.12.0) was used to automate image acquisition. Worms were anesthetized on 5% agarose pads containing 7 mM NaN₃ and secured with a coverslip. Acquired images were processed through Fiji software (version: 2.0.0-rc-69/1.52p).

For LP869 *cpSi171[vha-8p::TIR1::F2A::mTagBFP2::AID*::NLS::tbb-2 3'UTR I:-5.32]*, LP870 *cpSi172[myo-2p::TIR1::F2A::mTagBFP2::AID*::NLS::tbb-2 3'UTR I:-5.32]*, and LP871 *cpSi174[myo-3p::TIR1::F2A::mTagBFP2::AID*::NLS::tbb-2 3'UTR I:-5.32]* Figure S4), mixed stage animals were transferred to 1 mM K-NAA NGM plates for 24 hours. Images were then

taken using the 60x objective on a Nikon TiE stand with CSU-X1 spinning disk head (Yokogawa), 447 nm, 514 nm, and 561 nm solid state lasers, ImagEM EMCCD camera (Hamamatsu). Worms were anesthetized and images were processed as described above.

AID*-tagged substrate depletion experiments

To examine depletion of mNG::AID*::PAR-3 in embryos (Figure 2), young adult worms were treated with either 1 mM IAA or 0.25% EtOH in standard liquid culture conditions (Stiernagle 2006) for 1 hour. Then, embryos were dissected on poly-lysine-coated coverslips and mounted in egg buffer with 22.8 μ m beads as spacers. Confocal images were captured on a Nikon Ti2 microscope equipped with 405 nm and 488 nm illumination lasers; a 60x, 1.4 NA oil immersion objective; a Visitech VT-iSIM scan head; and a Photometrics PrimeBSI camera controlled by μ Manager software. The total amount of mNG::AID*::PAR-3 present in each embryo was measured in FIJI by drawing a box around each embryo, measuring integrated pixel intensity, and then converting to a fluorescence intensity by subtracting off-embryo background. Results were plotted using GraphPad Prism software.

To monitor depletion of GFP::AID in the vulval precursor cells (Figure 4B,C) CA1202 *ieSi57 [eft-3p::TIR1::mRuby::unc-54 3'UTR + Cbr-unc-119(+)] II*; *ieSi58 [eft-3p::degron::GFP::unc-54 3'UTR + Cbr-unc-119(+)] IV* and JDW185 *wrdSi54[eft-3p:TIR1:F2A:mTagBFP2:tbb-2 3'UTR, l:-5.32]; unc-119(ed3) III*; *ieSi58 [eft-3p::AID*::GFP::unc-54 3'UTR + Cbr-unc-119(+)] IV* animals were grown on NGM plates until early L3. A subset of animals were imaged at timepoint “0

min”, and the remainder were shifted onto 1 mM K-NAA and imaged at the indicated timepoints. Images were acquired using a Plan-Apochromat 100x/1.4 DIC objective on a custom-built upright spinning-disk confocal microscope. This microscope consisted of a Zeiss Axio Imager.A2 modified with a Borealis-modified Yokogawa CSU-10 confocal scanner unit with 405 nm lasers and 488 nm lasers and equipped with a Hamamatsu Orca EM-CCD camera. MetaMorph software (version: 7.8.12.0) was used to automate image acquisition. Worms were anesthetized on 5% agarose pads containing 7 mM NaN₃ and secured with a coverslip. Acquired images were processed through Fiji software (version: 2.0.0-rc-69/1.52p). GFP was quantified as described in Martinez et al. (2020). Measurements of total fluorescence intensity in the nucleus was measured, and fluorescence intensity immediately outside the circumference of the nucleus was also measured to obtain the cytoplasmic value. The ratio of these intensities is plotted in Figure S3. For Figure 4C, only the nuclear intensity was plotted.

To monitor depletion of nuclear NHR-25::GFP::AID* in the vulval precursor cells and seam cells using *eft-3p::TIR1* transgenes (Figure 5), JDW71 *ieSi57 [eft-3p::TIR1::mRuby2::unc-54 3'UTR, cb-unc-119(+)] II; unc-119(ed3) III; nhr-25(wrd18[nhr-25::GFP::AID*:3xFLAG]) X* and JDW187 *wrdSi23[eft-3p::TIR1:F2A:mTagBFP2::AID*::NLS:tbb-2 3'UTR, l:-5.32]; wrd52[nhr-25::GFP::AID*:3xFLAG] X* animals were grown to L3 on NGM plates. Animals were auxin treated, and they were imaged and analyzed as described above for AID*::GFP depletion experiments. Experiments measuring NHR-25::GFP::AID* depletion using DQM623 *bmd176[cdh-3pTIR1::F2A::mTagBFP2::AID*::NLS] II; nhr-25(wrd10[nhr-*

25::GFP^{AID}:3xFLAG]) X were similarly performed (Figure 7), except animals were imaged one hour after exposure to control or 4 mM K-NAA plates.

Western Blot Analysis

For all western blots, animals were synchronized by sodium hypochlorite treatment, moved to nematode growth media (NGM) plates seeded with *E. coli* OP50, and grown at 20°C for ~40 hours. L4 animals were collected untreated or exposed to 4 mM auxin (IAA) or ethanol for the amount of time specified prior to collection in M9 buffer. Animals were washed several times, pelleted, and freeze cracked in liquid nitrogen 2X. To each worm sample was added house-made 4x Laemmli Sample Buffer, followed by 10 minutes boiling at 95°C and centrifugation. The resulting supernatants were used for western blot analysis. The total proteins were denatured for 10 min at 95°C. Equal amounts of protein samples were loaded and separated by precast 4-20% Mini-Protean TGX Stain Free Gels (Bio-Rad) then transferred to polyvinylidene difluoride membranes. The primary antibodies used were rabbit anti-GFP antibody (Abcam, #ab290) (Figure 4 and Figure S1), and rabbit anti-tRFP (Evrogen, #AB233) (Figure 3) both diluted at 1:1000. The secondary antibody used was goat anti-Rabbit-HRP (Kindle Biosciences LLC, #R1006) diluted at 1:1000 in all cases. Images were captured with a Bio-Rad ChemiDoc imaging system.

Phenotypic analysis

For all strains containing *nhr-23::GFP::AID** and *nhr-25::GFP::AID** (Table 2, Table S5), experiments were performed as previously described (Zhang *et al.* 2015). Briefly, adult hermaphrodites were picked onto MYOB plates seeded with OP50 and containing 4 mM IAA, 4 mM K-NAA, or EtOH (control). Adults were permitted to lay eggs for 4 hours at 25°C prior to being removed and the resulting progeny were kept at 25°C and scored daily for larval arrest and gonadal abnormalities for four days. For strains containing *daf-15::mNG::AID** (Table 3, Table S6), animals were synchronized at L1 by sodium hypochlorite treatment and released onto MYOB plates seeded with OP50 and containing either 4 mM auxin (IAA or K-NAA), or EtOH (control). Animals were grown at 20°C for 4 days and scored for larval arrest. Larval arrest stage (L2 vs L3) was determined by animal size and confirmed by imaging a subset of animals by DIC microscopy and evaluating gonadal development.

Statistical analysis

Statistical significance was determined using a two-tailed unpaired Student's t-test. $P < 0.05$ was considered statistically significant. **** indicates $P < 0.0001$

Data availability

Strains in Figure 6A and Table S4 are available through the *Caenorhabditis* Genetics Center with the exception of DQM526 which can be obtained upon request from Prof. David Matus. Other strains and plasmids can be requested directly from the authors. The data that

support the findings of this study are available upon reasonable request. The indicated plasmids in Table S2 will be made available through Addgene. Supplemental files will be available on figshare at <https://figshare.com/s/2e570e4c83c897462926>.

Acknowledgments:

Many thanks to Matthew Schwartz for providing reagents and suggestions to get the SapTrap system established in our lab. We thank Oliver Hobert, Troy McDiarmid, and Francis McNally for helpful discussions about the AID system. We thank Alison Woollard for sharing unpublished information about a minimal SCM enhancer. G.A., M.T.L., L.C.J., H.N.S., and J.D.W. are supported by the NIH/NIGMS [R00 GM107345 and R01 GM138701]. J.M.R and J.D.W are supported by National Science Foundation (NSF) Division of Molecular and Cellular Biosciences (CAREER award 1942922). J.D.H. is supported by F32 GM131577, J.D.H. and B.G. are supported by R35 GM134838, D.J.D. is supported by R00-GM115964, and T.D. and D.J.R are supported by R01 GM121625. D.Q.M. is supported by the NIH NIGMS [R01 GM121597]. D.Q.M. is also a Damon Runyon-Rachleff Innovator supported (in part) by the Damon Runyon Cancer Research Foundation [DRR-47-17]. M.A.Q.M. is supported by the NIGMS [R01 GM121597-02S2]. N.J.P. is supported by the American Cancer Society [132969-PF-18-226-01-CSM]. T.N.M.-K. is supported by the NICHD [F31 HD100091]. D.J.D. is also a CPRIT Scholar supported by Cancer Prevention and Research Institute of Texas Grant RR170054. Some strains were provided by the Caenorhabditis Genetics Center, which is funded by the NIH Office of Research Infrastructure Programs [P40 OD010440].

AUTHOR CONTRIBUTIONS

D.J.D. designed the built-in F2A::BFP::AID*::NLS reporter strategy for TIR1 expression and activity. G.A, T.D., M.L., M.A.Q.M., L.C.J., J.D.H, N.J.P., D.Q.M., D.J.D., D.J.R., and J.D.W. conceived and designed the experiments. G.A. T.D., R.D., J.D.H., W.Z., T.N.M.-K., S.S.S., D.Q.M., D.J.D., D.J.R., and J.D.W. designed the constructs. T.D., J.D.H., R.D., N.J.P., J.M.R, and D.J.D. performed the microinjections. G.A., T.D., M.L., M.A.Q.M., J.D.H., N.J.P., and D.J.D. performed the crosses and characterized strains. G.A., T.D., M.L., R.D., M.A.Q.M., L.C.J., J.D.H., H.N.S., N.J.P., R.M., B.D., J.M.R., and D.J.D. performed the experiments. G.A., T.D., M.A.Q.M., J.D.H., N.J.P., D.Q.M., D.J.D., D.J.R., and J.D.W. analyzed and quantified the data. G.A. and J.D.W. wrote the manuscript with contributions from the other authors. The authors declare no competing interests.

Supplemental Figures:

Ashley *et al.* (2020) Figure S1

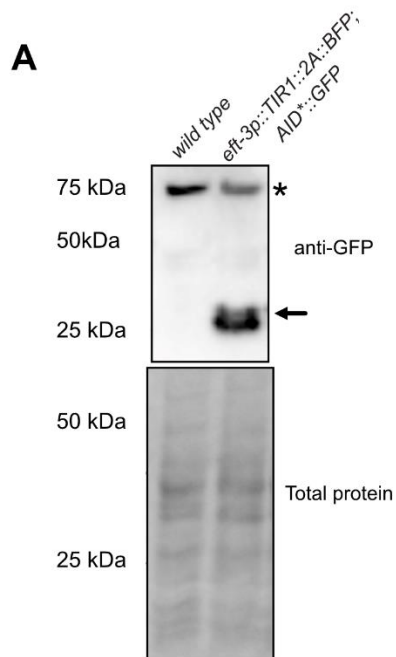


Figure S1. Anti-GFP western blot with wild type (N2) control. A) Anti-GFP western blot performed in wild type (left) and in an AID*::GFP reporter strain containing the *eft-3::TIR1::F2A::BFP::AID*::NLS* insertion. Anti-GFP blot (top) showing background band (marked with *; see Figure S1) and a doublet at approximately 27 kDa, (arrow) consistent with the predicted size of GFP. Stain-free (Bio-Rad) analysis of total protein on the blot is provided as a loading control. Marker size (in kilodaltons) is provided

Ashley et al. (2020) Figure S2

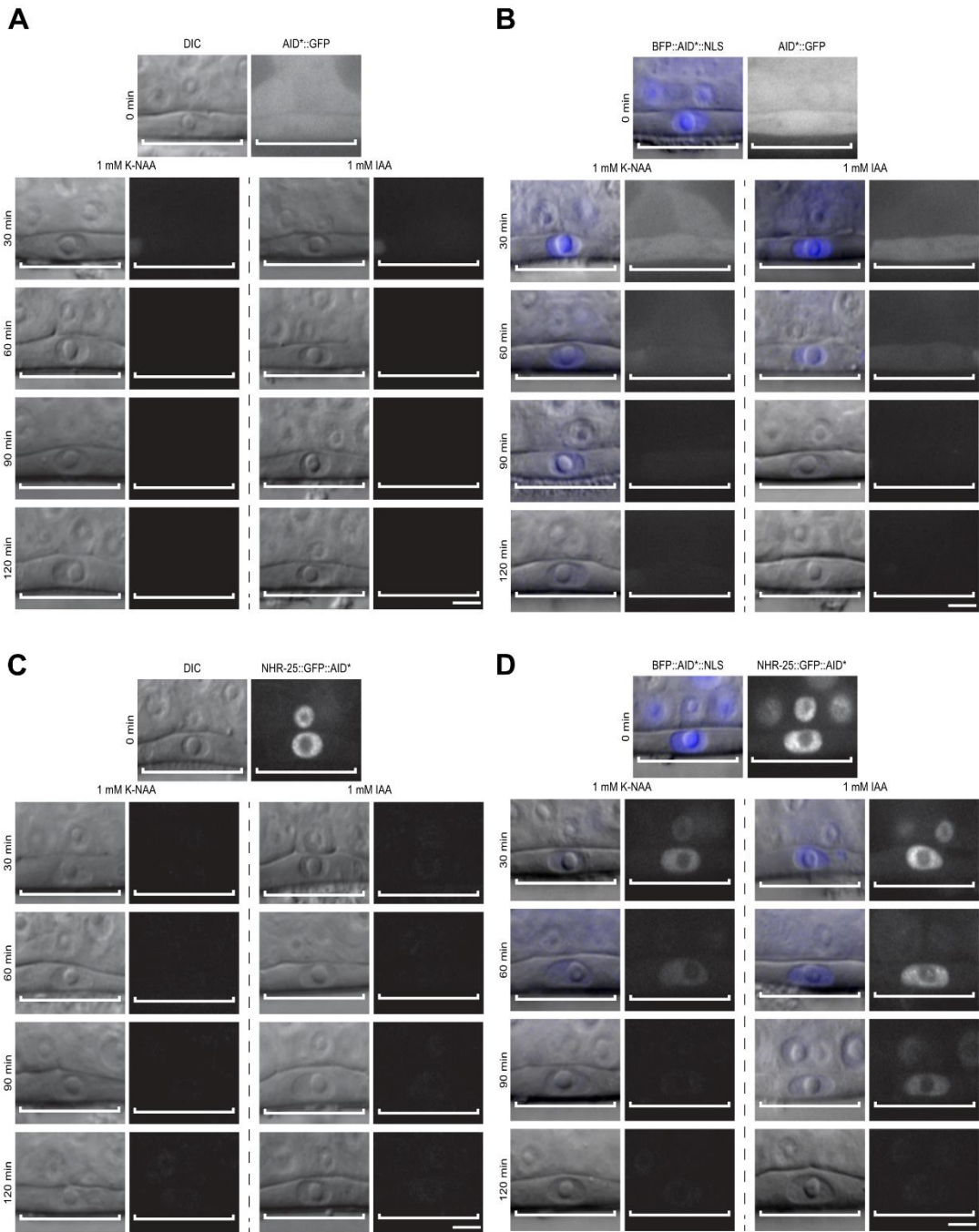


Figure S2. Representative images of AID*::GFP and NHR-25::GFP::AID* depletion in animals expressing either *eft-3p::TIR1::mRuby2* or *eft-3p::TIR1::F2A::BFP::AID*::NLS*. A-D) DIC and corresponding GFP images of VPCs (brackets) from L3 larvae at the P6.p 1-cell stage. For animals expressing *eft-3p::TIR1::F2A::BFP::AID*::NLS*, an overlay of DIC and BFP images were used to demonstrate BFP internal control expression in VPCs. Animals expressing *eft-3p::TIR1::mRuby2* (A,C) and *eft-3p::TIR1::F2A::BFP::AID*::NLS* (B,D) were treated with 1 mM K-NAA or IAA to visualize loss of AID*::GFP (A,B) and NHR-25::GFP::AID* (C,D) over time.

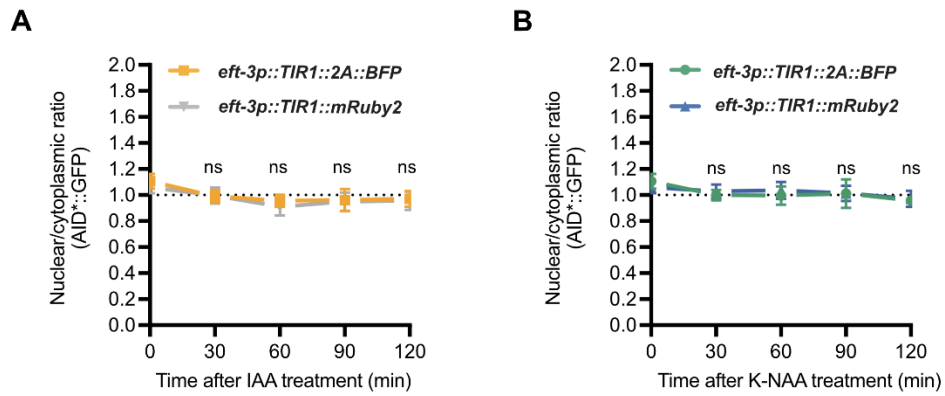


Figure S3. Nuclear/cytoplasmic ratios of AID*::GFP in VPCs with activated TIR1. These ratios were calculated by dividing AID*::GFP levels in the nucleus by AID*::GFP levels in the cytoplasm. L3s expressing *eft-3p::TIR1::F2A::BFP::AID*::NLS* and *eft-3p::TIR1::mRuby2* animals exposed to 1 mM IAA (A) or K-NAA (B) were analyzed. In both instances, the mean ratio of normalized fluorescent intensity from the nucleus and cytoplasm is shown from a single replicate of 10 or more animals. Error bars represent standard deviation

Ashley et al. (2020) Figure S4

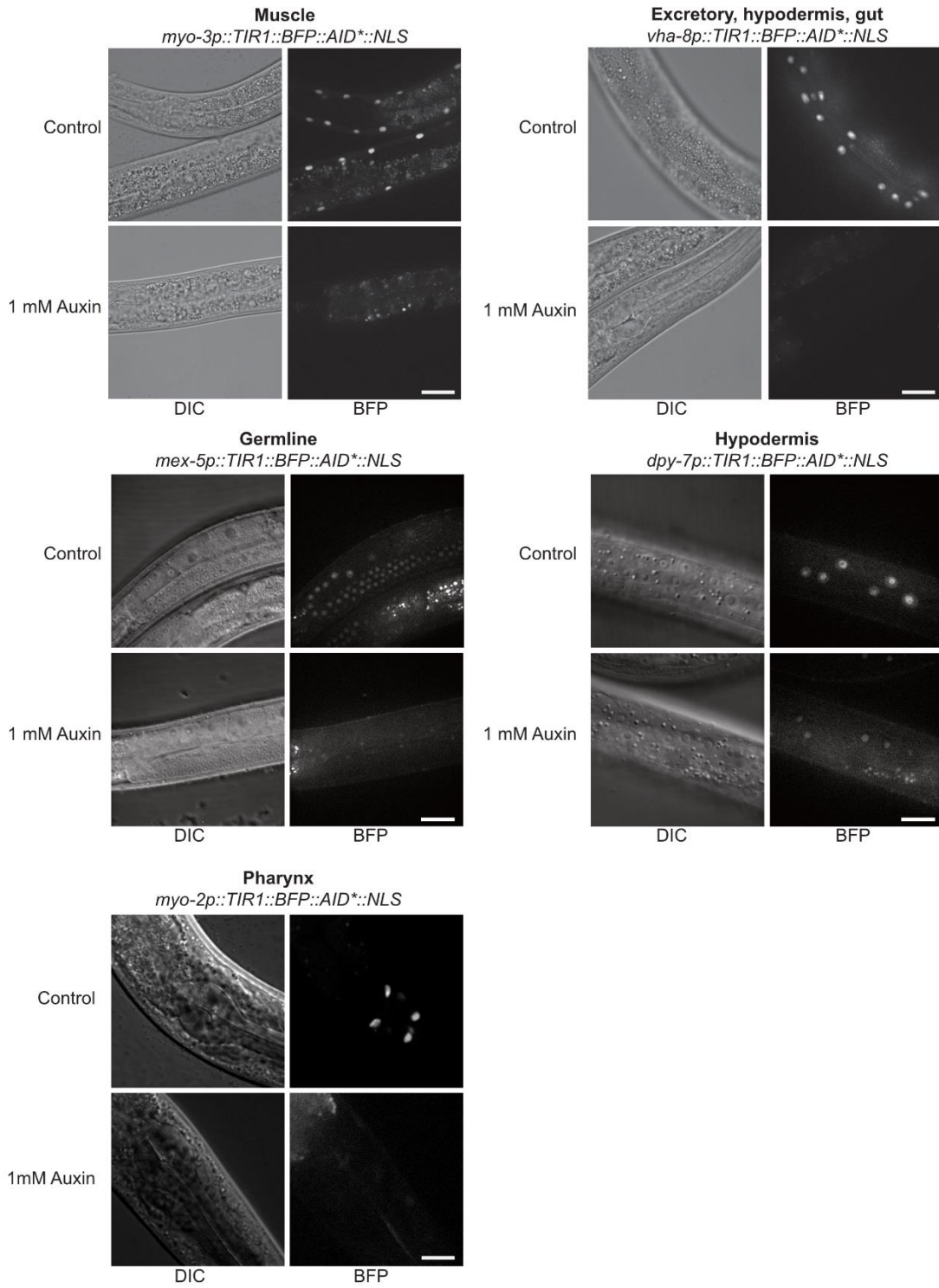


Figure S4. Functional test of new TIR1-expressing strains. Strains of the indicated genotypes were grown on 1 mM water-soluble, synthetic auxin (K-NAA) for ~24 hours (*myo-2*, *myo-3p* and *vha-8p*) or for 1 hour (*mex-5p* and *dpy-7p*) before imaging. Animals were similarly grown on control seeded NGM plates lacking K-NAA. For all strains, the expected BFP expression pattern was observed in control animals, and BFP expression was reduced or lost in auxin treated animals. Scale bars represent 20 μm (*myo-2*, *myo-3p*, *vha-8p*), 15 μm (*dpy-7p*), and 40 μm (*mex-5p*).

Bibliography

- Breunig J. J., R. Levy, C. D. Antonuk, J. Molina, M. Dutra-Clarke, et al., 2015 Ets Factors Regulate Neural Stem Cell Depletion and Gliogenesis in Ras Pathway Glioma. *Cell Rep.* 12: 258–271. <https://doi.org/10.1016/j.celrep.2015.06.012>
- Brown K. M., S. Long, and L. D. Sibley, 2017 Plasma Membrane Association by N-Acylation Governs PKG Function in *Toxoplasma gondii*. *mBio* 8: e00375-17. <https://doi.org/10.1128/mBio.00375-17>
- Camlin N. J., and J. P. Evans, 2019 Auxin-inducible protein degradation as a novel approach for protein depletion and reverse genetic discoveries in mammalian oocytes. *Biol. Reprod.* 101: 704–718. <https://doi.org/10.1093/biolre/iox113>
- Chen B., L. A. Gilbert, B. A. Cimini, J. Schnitzbauer, W. Zhang, et al., 2013 Dynamic Imaging of Genomic Loci in Living Human Cells by an Optimized CRISPR/Cas System. *Cell* 155: 1479–1491. <https://doi.org/10.1016/j.cell.2013.12.001>
- Chen W., M. Werdann, and Y. Zhang, 2018 The auxin-inducible degradation system enables conditional PERIOD protein depletion in the nervous system of *Drosophila melanogaster*. *FEBS J.* 285: 4378–4393. <https://doi.org/10.1111/febs.14677>
- Daniel K., J. Icha, C. Horenburg, D. Müller, C. Norden, et al., 2018 Conditional control of fluorescent protein degradation by an auxin-dependent nanobody. *Nat. Commun.* 9: 3297–13. <https://doi.org/10.1038/s41467-018-05855-5>
- Dickinson D. J., J. D. Ward, D. J. Reiner, and B. Goldstein, 2013 Engineering the *Caenorhabditis elegans* genome using Cas9-triggered homologous recombination. *Nat. Methods* 10: 1028–1034. <https://doi.org/10.1038/nmeth.2641>
- Dickinson D. J., A. M. Pani, J. K. Heppert, C. D. Higgins, and B. Goldstein, 2015 Streamlined Genome Engineering with a Self-Excising Drug Selection Cassette. *Genetics* 200: 1035–1049. <https://doi.org/10.1534/genetics.115.178335>

Dickinson D. J., and B. Goldstein, 2016 CRISPR-Based Methods for *Caenorhabditis elegans* Genome Engineering. *Genetics* 202: 885–901. <https://doi.org/10.1534/genetics.115.182162>

Dickinson D. J., M. M. Slabodnick, A. H. Chen, and B. Goldstein, 2018 SapTrap assembly of repair templates for Cas9-triggered homologous recombination with a self-excising cassette. *MicroPublication Biol.* <https://doi.org/10.17912/W2KTON>

Dokshin G. A., K. S. Ghanta, K. M. Piscopo, and C. C. Mello, 2018 Robust Genome Editing with Short Single-Stranded and Long, Partially Single-Stranded DNA Donors in *Caenorhabditis elegans*. *Genetics* 210: 781–787. <https://doi.org/10.1534/genetics.118.301532>

Duong T., N. R. Rasmussen, E. Ballato, F. S. Mote, and D. J. Reiner, 2020 The Rheb-TORC1 signaling axis functions as a developmental checkpoint. *Development* 147: dev181727. <https://doi.org/10.1242/dev.181727>

Engler C., R. Gruetzner, R. Kandzia, and S. Marillonnet, 2009 Golden Gate Shuffling: A One-Pot DNA Shuffling Method Based on Type II Restriction Enzymes. *PLoS ONE* 4: e5553. <https://doi.org/10.1371/journal.pone.0005553>

Fielmich L.-E., R. Schmidt, D. J. Dickinson, B. Goldstein, A. Akhmanova, et al., 2018 Optogenetic dissection of mitotic spindle positioning in vivo. *eLife* 7: 219. <https://doi.org/10.7554/eLife.38198>

Ghanta K. S., and C. C. Mello, 2020 Melting dsDNA Donor Molecules Greatly Improves Precision Genome Editing in *Caenorhabditis elegans*. *Genetics* 216: 643–650. <https://doi.org/10.1534/genetics.120.303564>

Holland A. J., D. Fachinetti, J. S. Han, and D. W. Cleveland, 2012 Inducible, reversible system for the rapid and complete degradation of proteins in mammalian cells. *Proc. Natl. Acad. Sci.* 109: E3350-7. <https://doi.org/10.1073/pnas.1216880109>

Kamath R. S., A. G. Fraser, Y. Dong, G. Poulin, R. Durbin, et al., 2003 Systematic functional analysis of the *Caenorhabditis elegans* genome using RNAi. *Nature* 421: 231–237. <https://doi.org/10.1038/nature01278>

Kasimatis K. R., M. J. Moerdyk-Schauwecker, and P. C. Phillips, 2018 Auxin-Mediated Sterility Induction System for Longevity and Mating Studies in *Caenorhabditis elegans*. *G3* 8: 2655–2662. <https://doi.org/10.1534/g3.118.200278>

Katoh Y., M. Terada, Y. Nishijima, R. Takei, S. Nozaki, et al., 2016 Overall Architecture of the Intraflagellar Transport (IFT)-B Complex Containing Cluap1/IFT38 as an Essential Component of the IFT-B Peripheral Subcomplex. *J. Biol. Chem.* 291: 10962–10975. <https://doi.org/10.1074/jbc.M116.713883>

- Kipreos E. T., L. E. Lander, J. P. Wing, W. W. He, and E. M. Hedgecock, 1996 *cul-1* Is Required for Cell Cycle Exit in *C. elegans* and Identifies a Novel Gene Family. *Cell* 85: 829–839. [https://doi.org/10.1016/S0092-8674\(00\)81267-2](https://doi.org/10.1016/S0092-8674(00)81267-2)
- Kovacs G., N. Montalbetti, A. Simonin, T. Danko, B. Balazs, et al., 2012 Inhibition of the human epithelial calcium channel TRPV6 by 2-aminoethoxydiphenyl borate (2-APB). *Cell Calcium* 52: 468–480. <https://doi.org/10.1016/j.ceca.2012.08.005>
- Li S., X. Prasanna, V. T. Salo, I. Vattulainen, and E. Ikonen, 2019 An efficient auxin-inducible degron system with low basal degradation in human cells. *Nat. Methods* 16: 866–869. <https://doi.org/10.1038/s41592-019-0512-x>
- Martinez M. A. Q., B. A. Kinney, T. N. Medwig-Kinney, G. Ashley, J. M. Ragle, et al., 2020 Rapid Degradation of *Caenorhabditis elegans* Proteins at Single-Cell Resolution with a Synthetic Auxin. *G3* 10: 267–280. <https://doi.org/10.1534/g3.119.400781>
- Matus D. Q., L. L. Lohmer, L. C. Kelley, A. J. Schindler, A. Q. Kohrman, et al., 2015 Invasive Cell Fate Requires G1 Cell-Cycle Arrest and Histone Deacetylase-Mediated Changes in Gene Expression. *Dev. Cell* 35: 162–174. <https://doi.org/10.1016/j.devcel.2015.10.002>
- Nance J., and C. Frøkjær-Jensen, 2019 The *Caenorhabditis elegans* Transgenic Toolbox. *Genetics* 212: 959–990. <https://doi.org/10.1534/genetics.119.301506>
- Natsume T., T. Kiyomitsu, Y. Saga, and M. T. Kanemaki, 2016 Rapid Protein Depletion in Human Cells by Auxin-Inducible Degron Tagging with Short Homology Donors. *Cell Rep.* 15: 210–218. <https://doi.org/10.1016/j.celrep.2016.03.001>
- Nayak S., F. E. Santiago, H. Jin, D. Lin, T. Schedl, et al., 2002 The *Caenorhabditis elegans* Skp1-Related Gene Family: Diverse Functions in Cell Proliferation, Morphogenesis, and Meiosis. *Curr. Biol.* 12: 277–287. [https://doi.org/10.1016/S0960-9822\(02\)00682-6](https://doi.org/10.1016/S0960-9822(02)00682-6)
- Nishimura K., T. Fukagawa, H. Takisawa, T. Kakimoto, and M. Kanemaki, 2009 An auxin-based degron system for the rapid depletion of proteins in nonplant cells. *Nat. Methods* 6: 917–922. <https://doi.org/10.1038/nmeth.1401>
- Nishimura K., R. Yamada, S. Hagihara, R. Iwasaki, N. Uchida, et al., 2020 A super sensitive auxin-inducible degron system with an engineered auxin-TIR1 pair. *bioRxiv* 2020.01.20.912113. <https://doi.org/10.1101/2020.01.20.912113>
- Nonet M. L., 2020 Efficient Transgenesis in *Caenorhabditis elegans* Using Flp Recombinase-Mediated Cassette Exchange. *Genetics* 215: 903–921. <https://doi.org/10.1534/genetics.120.303388>
- Norris A. D., H.-M. Kim, M. P. Colaiácovo, and J. A. Calarco, 2015 Efficient Genome Editing in *Caenorhabditis elegans* with a Toolkit of Dual-Marker Selection Cassettes. *Genetics* 201: 449–458. <https://doi.org/10.1534/genetics.115.180679>

- Paix A., A. Folkmann, D. Rasoloson, and G. Seydoux, 2015 High Efficiency, Homology-Directed Genome Editing in *Caenorhabditis elegans* Using CRISPR-Cas9 Ribonucleoprotein Complexes. *Genetics* 201: 47–54. <https://doi.org/10.1534/genetics.115.179382>
- Patel T., and O. Hobert, 2017 Coordinated control of terminal differentiation and restriction of cellular plasticity. *eLife* 6: 249. <https://doi.org/10.7554/eLife.24100>
- Ragle J. M., A. L. Aita, K. N. Morrison, R. Martinez-Mendez, H. N. Saeger, et al., 2020 The conserved molting/circadian rhythm regulator NHR-23/NR1F1 serves as an essential co-regulator of *C. elegans* spermatogenesis. *Development* <https://doi.org/10.1242/dev.193862>
- Sathyan K. M., B. D. McKenna, W. D. Anderson, F. M. Duarte, L. Core, et al., 2019 An improved auxin-inducible degron system preserves native protein levels and enables rapid and specific protein depletion. *Genes Dev.* 33: 1441–1455. <https://doi.org/10.1101/gad.328237.119>
- Schiksnis E., A. Nicholson, M. Modena, M. Pule, J. Arribere, et al., 2020 Auxin-independent depletion of degron-tagged proteins by TIR1. *MicroPublication Biol.* 2020. <https://doi.org/10.17912/micropub.biology.000213>
- Schwartz M. L., and E. M. Jorgensen, 2016 SapTrap, a Toolkit for High-Throughput CRISPR/Cas9 Gene Modification in *Caenorhabditis elegans*. *Genetics* 202: 1277–1288. <https://doi.org/10.1534/genetics.115.184275>
- Serrano-Saiz E., E. Leyva-Díaz, E. De La Cruz, and O. Hobert, 2018 BRN3-type POU Homeobox Genes Maintain the Identity of Mature Postmitotic Neurons in Nematodes and Mice. *Curr. Biol.* 28: 2813–2823.e2. <https://doi.org/10.1016/j.cub.2018.06.045>
- Stiernagle T., 2006 Maintenance of *C. elegans*. *WormBook*. <https://doi.org/10.1895/wormbook.1.101.1>
- Trost M., A. C. Blattner, S. Leo, and C. F. Lehner, 2016 *Drosophila dany* is essential for transcriptional control and nuclear architecture in spermatocytes. *Development* 143: 2664–2676. <https://doi.org/10.1242/dev.134759>
- Ward J. D., N. Bojanala, T. Bernal, K. Ashrafi, M. Asahina, et al., 2013 Sumoylated NHR-25/NR5A Regulates Cell Fate during *C. elegans* Vulval Development. *PLoS Genet.* 9: e1003992. <https://doi.org/10.1371/journal.pgen.1003992.s010>
- Ward J. D., B. Mullaney, B. J. Schiller, L. D. He, S. E. Petnic, et al., 2014 Defects in the *C. elegans* acyl-CoA Synthase, *acs-3*, and Nuclear Hormone Receptor, *nhr-25*, Cause Sensitivity to Distinct, but Overlapping Stresses. *PLoS ONE* 9: e92552. <https://doi.org/10.1371/journal.pone.0092552.s013>
- Ward J. D., 2015 Rapid and Precise Engineering of the *Caenorhabditis elegans* Genome with Lethal Mutation Co-Conversion and Inactivation of NHEJ Repair. *Genetics* 199: 363–377. <https://doi.org/10.1534/genetics.114.172361>

- Yesbolatova A., Y. Saito, N. Kitamoto, H. Makino-Itou, R. Ajima, et al., 2020 The auxin-inducible degron 2 technology provides sharp degradation control in yeast, mammalian cells, and mice. *Nat. Commun.* 11: 5701. <https://doi.org/10.1038/s41467-020-19532-z>
- Yoshina S., Y. Suehiro, E. Kage-Nakadai, and S. Mitani, 2016 Locus-specific integration of extrachromosomal transgenes in *C. elegans* with the CRISPR/Cas9 system. *Biochem. Biophys. Rep.* 5: 70–76. <https://doi.org/10.1016/j.bbrep.2015.11.017>
- Zasadzińska E., J. Huang, A. O. Bailey, L. Y. Guo, N. S. Lee, et al., 2018 Inheritance of CENP-A Nucleosomes during DNA Replication Requires HJURP. *Dev. Cell* 47: 348-362.e7. <https://doi.org/10.1016/j.devcel.2018.09.003>
- Zhang L., J. D. Ward, Z. Cheng, and A. F. Dernburg, 2015 The auxin-inducible degradation (AID) system enables versatile conditional protein depletion in *C. elegans*. *Development* 142: 4374–4384. <https://doi.org/10.1242/dev.129635>
- Zhang D., S. Tu, M. Stubna, W.-S. Wu, W.-C. Huang, et al., 2018 The piRNA targeting rules and the resistance to piRNA silencing in endogenous genes. *Science* 359: 587–592. <https://doi.org/10.1126/science.aao2840>

